

# Impact Assessment of Sand and Dust Storms on key socio-economic sectors: Aviation

Master Thesis conducted by:

**Konstantina Chouta**

Supervised by:

**María Gonçalves Ageitos**

Universitat Politècnica de Catalunya, UPC

External Supervisors:

**Sara Basart**

Barcelona Supercomputer Center, BSC

**Isadora Christel Jiménez**

Barcelona Supercomputer Center, BSC

Master in:

Environmental Engineering

Department of Project and Construction Engineering

Barcelona, 29<sup>th</sup> of September 2020

**MASTER THESIS**

## Abstract

Desert dust is the dominating species of atmospheric aerosols over large areas of the Earth, accounting for about 35% of the total aerosol mass. It is mainly generated in arid and semi-arid regions, but it can be transported hundreds to thousands of kilometers away, resulting in a unique type of environmental hazard. Apart from its implications for the climate, mineral dust and its related phenomena, particularly the sand and dust storms impact air quality and ecosystems, human health, and various socio-economic sectors, such as solar energy production, agriculture, aviation and ground transportation.

Focusing on the aviation sector, poor visibility associated to intense sand and dust storms is one of the main weather-related factors that can lead to flight delays, cancellation, or rerouting. Additionally, in airports located in dust-prone areas, frequent visibility reduction leads to the implementation of special protocols for landing and take-off, as well as the modification of the applied flight management strategies. The availability of reliable forecasts can help predict situations of low visibility and serve as a mitigation strategy to reduce dust-induced impacts in airports.

The aim of the present Master Thesis is the development of a dust-related forecast product for the aviation sector. The proposed aviation product will predict the visibility reduction due to sand and dust storms and it will be considered for implementation under the framework of the WMO Barcelona Dust Forecast Center.

## Acknowledgements

I would like to thank my supervisors, María Gonçalves Ageitos, Isadora Christel Jiménez and especially Sara Basart for their trust and the great opportunity they gave me to develop this project in the Earth Sciences Department at the Barcelona Supercomputing Center (BSC). Their guidance and support throughout the whole duration of the project, their patience, their valuable time and the different ways in which each one of them inspired me and contributed to my learning process are gratefully acknowledged and deeply appreciated.

Thanks to all researchers from the Earth Sciences Department of BSC involved in the development and maintenance of the NMMB-MONARCH model. Special thanks to Dr Oriol Jorba for providing the simulation outputs used in the present project.

Also, I would like to thank all the staff and contributing researchers of the Regional Center for Northern Africa, Middle East and Europe of the World Meteorological Organisation (WMO) of the Barcelona Dust Forecast Center and the Sand and Dust Warning Advisory and Assessment System (SDS-WAS) and especially Ernest Werner for his valuable advice and consultations.

The long-term dust research program at the Barcelona Supercomputing Center – Centro Nacional de Supercomputación (BSC-CNS) is associated to the AXA Research Fund. The European projects inDust (COST Action CA16202 supported by COST Association) and DustClim (as a part of ERA4CS, an ERANet initiated by JPI Climate, and funded by FORMAS (SE), DLR (DE), BMFWF (AT), IFD (DK), MINECO (ES), ANR (FR) with co-funding by the European Union Grant 690462) are also gratefully acknowledged.

Last but not least, I would like to thank my mother for her unconditional support in every life goal I decide to pursue, my friends in Greece for always being present in my life besides the physical distance, my friends in Barcelona for all the great moments we shared together during the last two years, my classmates from UPC that added value and challenges to the whole learning process we have been through together, and my colleagues from the Earth System Services group in BSC for their warm welcome into the scientific world.

## List of contents

1	Project aim and objectives .....	1
1.1	Specific objectives.....	1
1.2	Work scope .....	2
1.3	Work plan.....	2
2	Scientific background.....	4
2.1	Aerosols in the Earth System.....	4
2.2	The Dust Cycle.....	6
2.3	Sand and Dust Storms .....	10
2.3.1	Defining sand and dust storms .....	10
2.3.2	Impacts related to Sand and Dust Storms .....	10
2.4	Dust short-term operational services .....	12
2.4.1	Dust forecasting .....	12
2.4.2	Dust observations.....	13
2.4.3	International initiatives on dust forecasting and monitoring.....	17
3	Methodology .....	19
3.1	NMMB-MONARCH description .....	19
3.1.1	Model simulation.....	20
3.2	Methodology scheme .....	21
4	Implementation of visibility in dust forecasts .....	23
4.1	Visibility approaches .....	23
4.2	Visibility evaluation: Methodology .....	25
4.3	Evaluation results.....	35
4.3.1	Multi-category contingency tables .....	35
4.3.2	Overall results: Skill scores .....	39
4.4	Visibility diagnostic.....	43
5	Impact assessment of SDS: Aviation sector .....	46
5.1	Methodology .....	46
5.1.1	Visibility thresholds for aviation .....	47
5.2	Impact analysis results .....	49
6	End-user product proposal .....	56
7	Conclusions .....	61
8	References .....	63
	Appendix A: List of the selected stations for the evaluation .....	71
	Appendix B: Percentage reduction of observations after the application of the RH filter.....	74
	Appendix C: Critical hours for the exceedance of the 1000m threshold.....	78



## List of figures

Figure 2.1: Global radiative forcing estimates in 2011 relative to 1750 and their uncertainties for the main drivers of climate change. The best estimates of the net radiative forcing are shown as black diamonds with the corresponding uncertainty bars; the confidence level in the net forcing is characterised as VH – very high, H – high, M – medium, L – low or VL – very low. Albedo forcing due to black carbon on snow and ice is included in the black carbon aerosol bar. Total anthropogenic radiative forcing is provided for three different years relative to 1750. Extracted from: IPCC AR5 Summary for Policymakers, 2013.....	5
Figure 2.2: Annual mean dust emission based on Moderate Resolution Imaging Spectroradiometer (MODIS) Deep Blue estimates of dust optical depth in conjunction with other data sets including land use. Extracted from Ginoux et al. (2012).....	7
Figure 2.3: The dust cycle in the Earth system and the main processes in which dust plays an important role. Extracted from: Shao et al., 2011.....	8
Figure 2.4: Pattern of global dust transportation and locations of the main deserts, including: (1) Great Basin, (2) Sonoran, (3) Chihuahua, (4) Peruvian, (5) Atacama, (6) Monte, (7) Patagonia, (8) Sahara, (9) Somali-Chabli, (10) Namib, (11) Kalahari, (12) Karroo, (13) Arabian, (14) Rub al Khali, (15) Turkestan, (16) Iranian, (17) Thar, (18) Taklimakan, (19) Gobi, (20) Great Sandy, (21) Simpson, (22) Gibson, (23) Great Victoria and (24) Sturt; Extracted from Shao et al. (2011).....	9
Figure 2.5: Map of surface stations currently included in GAW. Extracted from: Benedetti et al., 2018, courtesy of MeteoSwiss. ....	16
Figure 2.6: Dust AOD forecast offered by the Barcelona Dust Forecast Center, depicting the reference domain, bounded by the following coordinates: longitude 25°W to 60°E and latitude 0° to 65°N. Extracted from: Barcelona Dust Forecast Center official webpage ( <a href="https://dust.aemet.es/">https://dust.aemet.es/</a> ) .....	18
Figure 3.1: Description of the meteorology-chemistry atmospheric NMMB-MONARCH model.....	19
Figure 3.2: Schematic diagram of the methodology applied in the different task groups that form the project. ....	22
Figure 4.1: Example of raw ISD data from the Al Maktoum International Airport - OMDW in Dubai, UAE for the 3rd of January 2018 at 03:00. Highlighted in blue correspond: the date and time of the observations, the visibility value, the air temperature and dew point temperature, the airport ICAO code and the present weather code.....	26
Figure 4.2: Geographical distribution of the ISD stations used in the model evaluation.....	26
Figure 4.3: Predicted time series for visibility diagnostics, as described in Table 4.1, and observations for the Al Ain International Airport in Abu Dhabi, UAE (N24°15.70', E55°36.55) for 2018 and 2019 respectively. ....	30
Figure 4.4: Predicted time series for visibility diagnostics, as described in Table 4.1, and observations for the Thomas Sankara International Airport Ouagadougou (N12°21.22', W1°30.72') in Burkina Faso for 2018 and 2019 respectively.....	31

Figure 4.5: Predicted time series for visibility diagnostics, as described in Table 4.1, and observations for the Boudghene Ben Ali Lotfi Airport (N31°39.16', W2°15.40') in Algeria for 2018 and 2019 respectively.....	32
Figure 4.6: Multi-category contingency tables depicting the frequency of predictions and observations in each category in the studied area for 2018: a) DA, b) Dayan , c) IZO, d) Koschmieder, e) Biral. ....	37
Figure 4.7: Multi-category contingency tables depicting the frequency of predictions and observations in each category in the studied area for 2019: a) DA, b) Dayan , c) IZO, d) Koschmieder, e) Biral. ....	38
Figure 4.8: Contingency tables depicting the performance of the tested calibrations for the Koschmieder equation versus the performance of the IZO diagnostic. a) Calibration with 1.5 factor- 2018, b) Calibration with 2 factor- 2018, c) Calibration with 2.5 factor-2018, d)IZO diagnostic- 2018, e) Calibration with 1.5 factor- 2019, f) Calibration with 2 factor- 2019, g) Calibration with 2.5 factor-2019, h)IZO diagnostic- 2019.....	45
Figure 5.1: A classification of airports according to ILS capacity. Green indicates commercial airport with ILS capacity; yellow: non-commercial ILS; magenta: commercial no ILS; red: non-commercial no ILS. Extracted from: (Votsis et al., DustClim Technical Report 2020)..	46
Figure 5.2: Number of days in 2018 and 2019 with exceedance of aviation-related thresholds, indicating possible changes in the applied flight rules and the flow of operations. a) 5000m VFR threshold in 2018, b) 800m IRF threshold in 2018, c) 1000m threshold in 2018, d) 550m VFR threshold in 2018, e) 5000m VFR threshold in 2019, f) 800m IRF threshold in 2018, g) 1000m threshold in 2019, h) 550m VFR threshold in 2019.....	50
Figure 5.3: Frequency of exceedance of the 5000m VFR category per 3-hourly timesteps and grid cell during 2018. a) Valid for 00h, b) Valid for 03h, c) Valid for 06h, d) Valid for 09h, e) Valid for 12h, f) Valid for 15h, g) Valid for 18h, h) Valid for 21h.....	54
Figure 5.4: Frequency of exceedance of the 5000m VFR category per 3-hourly timesteps and grid cell during 2019. a) Valid for 00h, b) Valid for 03h, c) Valid for 06h, d) Valid for 09h, e) Valid for 12h, f) Valid for 15h, g) Valid for 18h, h) Valid for 21h.....	55
Figure 6.1: Visibility forecast for 12-13 February 2018 . a) Valid for 12h of 12 Feb 2018, b)Valid for 15h of 12 Feb 2018, c) Valid for 18h of 12 Feb 2018, d) Valid for 21h of 12 Feb 2018, e) Valid for 00h of 13 Feb 2018, f) Valid for 03 of 13 Feb 2018, g) Valid for 06h of 13 Feb 2018, h) Valid for 12h of 13 Feb 2018.....	58

## List of tables

Table 1.1: Gantt Chart of 31 weeks, including the main task groups identified from the specific objectives of the project, consultation meetings and the preparation of the final presentation.....	3
Table 4.1: Tested physically based and empirical equations to estimate visibility. PM <sub>10</sub> stands for particulate matter with diameter less than 10µm, V for horizontal visibility and ec for the extinction coefficient in the visible range (at 550nm). ....	24
Table 4.2: Definition of visibility categories for categorical forecast evaluation with visibility observations in NAME.....	29

Table 4.3: Example of multi-category contingency table.....	33
Table 4.4: Statistics used for the evaluation of categorical forecasts.....	34
Table 4.5: Overall skill scores for evaluation for the five tested visibility diagnostics (described in Table 4.1) for 2018 and 2019. ....	39
Table 4.6: Overall skill scores by categories for the five tested visibility diagnostics (described in Table 4.1) for 2018 and 2019. ....	41
Table 4.7: Accuracy of visibility diagnostics for four selected countries: Burkina Faso (Sahel), UAE (Middle East), and Algeria (Northern Africa), for 2018 and 2019. ....	42
Table 5.1: Runway Visual Range (RVR) and visibility limits for ILS approach categories for precision approach and landing. Source: ICAO, Manual of all-weather operations .....	48
Table 5.2: Visibility thresholds used for the impact analysis of low visibility conditions on air operations.....	49

## List of Acronyms

<b>AE</b>	Ångström Exponent
<b>AEMET</b>	Spanish State Meteorological Center
<b>AERONET</b>	Aerosol Robotic Network
<b>AOD</b>	Aerosol optical depth
<b>BDFC</b>	Barcelona Dust Forecast Center
<b>BSC</b>	Barcelona Supercomputing Center
<b>CAMS</b>	Copernicus Atmosphere Monitoring Service
<b>CNN</b>	Cloud condensation nuclei
<b>CSP</b>	Concentrating solar-thermal power
<b>DA</b>	Data assimilation
<b>DH</b>	Decision height
<b>EEA</b>	European Environment Agency
<b>ICAO</b>	International Civil Aviation Organization
<b>ICAP</b>	International Cooperative for Aerosol Prediction
<b>IFN</b>	Ice formation nuclei
<b>IFR</b>	Instrument Flight Rules
<b>ILS</b>	Instrument Landing System
<b>IPCC</b>	Intergovernmental Panel on Climate Change
<b>ISD</b>	Integrated Surface Database
<b>LVP</b>	Low Visibility Protocol
<b>METAR</b>	Meteorological Terminal Air Report
<b>MONARCH</b>	Multiscale Online Nonhydrostatic AtmospheRe CHemistry
<b>NAAP</b>	Numerical atmospheric aerosol prediction

<b>NAME</b>	North Africa- Middle East
<b>NAMEE</b>	North Africa - Middle East - Europe
<b>NCDC</b>	National Climatic Data Center
<b>NMMB</b>	Nonhydrostatic Multiscale Model on the B-grid
<b>NRT</b>	Near-real-time
<b>NWP</b>	Numerical weather prediction
<b>PM</b>	Particulate matter
<b>PM10</b>	Particulate matter with diameter less than 10nm
<b>PM2.5</b>	Particulate matter with diameter less than 2.5nm
<b>PV</b>	Photovoltaic
<b>RF</b>	Radiative forcing
<b>RH</b>	Relative Humidity
<b>RSMC-ASDF</b>	Regional Specialized Meteorological Center- Atmospheric Sand and Dust Forecast
<b>RVR</b>	Runway visual range
<b>SDG</b>	Sustainable Development Goals
<b>SDS</b>	Sand and Dust Storms
<b>SDS-WAS</b>	Sand and Dust Storms- Warning Advisory System
<b>SYNOP</b>	Surface Synoptic Observations
<b>UN</b>	United Nations
<b>VFR</b>	Visual Flight Rules
<b>WHO</b>	World Health Organization
<b>WMO</b>	World Meteorological Organization

## 1 Project aim and objectives

The aim of the present Master Thesis is the **development of a dust-related forecast product for the aviation sector**. The proposed aviation product will predict the visibility reduction due to sand and dust storms (SDS).

The present work is developed in the framework of the activities of the World Meteorological Organisation (WMO) Regional Specialised Meteorological Center with activity specialisation on Atmospheric Sand and Dust Forecast (RSMC-ASDF), the **Barcelona Dust Forecast Center**. The mission of this operational center is to generate and distribute operational dust predictions for Northern Africa, the Middle East and Europe (NAMEE). The daily dust forecast products offered by the center are based on the NMMB-MONARCH model and serve the need of various sectors to access reliable desert dust predictions.

For the aviation sector, the availability of visibility predictions is crucial. In dust-prone areas, visibility reduction due to SDS potentially leads to flight delays, cancellations, or rerouting (Lekas *et al.*, 2014). Additionally, it entails the implementation of special protocols for landing, take-off, and flight management, with the aim to reduce the environmental risks related to airport operations. Therefore, the aim of the present work, to design a visibility-dust forecast as a tool to predict and assess the impacts of SDS in air operations in the NAMEE domain, is considered extremely relevant for the sector of aviation.

The evaluation of the NMMB-MONARCH atmospheric model, which is the reference prediction model of the Barcelona Dust Forecast Center, as well as the proposal of a methodology to diagnose visibility from the model's output are essential stages of the design process of the final product.

### 1.1 Specific objectives

The specific objectives that are established to achieve the project aim are the following:

- Implementation of a visibility diagnostic from the atmospheric composition NMMB-MONARCH model output, after testing different parametrisations.
- Development of a methodology for the evaluation of the NMMB-MONARCH model on surface level using visibility observations.
- Assessment of the impact of desert dust events on the aviation sector in dust-prone areas based on visibility reduction estimations.

## 1.2 Work scope

The present work focuses on the selection of an appropriate method to diagnose visibility from the variables provided by the NMMB-MONARCH model, after testing five different theoretical and empirical parametrisations obtained from literature. The performance and suitability of the parametrisations is assessed through comparison against visibility observations for a period of 2 years. The impacts of low visibility conditions caused by the presence of desert dust are assessed for airports located in North Africa and the Middle East (NAME). Only impacts related to airport operations and flight disruptions are considered. The visibility-dust forecast product, proposed under the framework of the Barcelona Dust Forecast Center, is based on the selected methodology and is considered suitable to predict the impacts of SDS on air operations in the NAME region.

It is out of the scope of the present work: to evaluate other prediction models; to run the research experiment of NMMB-MONARCH in order to obtain the output; to evaluate the model output with observations different than visibility; to perform any kind of analysis in domains located out of the NAME region; to provide an overview of the evolution of the model performance over the years; to perform impact assessments for other sectors; to consider risks related with mechanical damages and maintenance operations in aviation; to assess economic impacts.

## 1.3 Work plan

The main tasks that are required to meet the specific objectives could be summarised in five task groups:

- **literature review** that includes bibliographical research related to the scientific background, model verification, visibility implementation and impact assessment studies;
- **academic writing** that consists in writing the present document;
- **visibility diagnostic implementation** that includes the comparison of different methods to derive dust-visibility from the model outputs, furtherly described in section 4.1;
- **model evaluation** that includes the quality control and dust-filtering of the observations, the calculation of categorical statistics for the comparison of the model output against observations and the presentation of the evaluation results for the proposed dust-visibility diagnostics in an appropriate and concise manner, furtherly presented in sections 4.2 and 4.3. This ultimately results in the selection of the most suitable visibility parametrisation to be considered for operational purposes, presented in section 4.4.

- **impact assessment for aviation**, that consists in the estimation of the number of low dust-visibility cases that could potentially affect airport operations, presented in section 5.2;
- **user product proposal**, that focuses on the description of the proposed dust-visibility forecast, presented in section 6.

To carry out the tasks mentioned before, a provisional work plan of 31 weeks is created, with duration from the 20<sup>th</sup> of January 2020 to the 25<sup>th</sup> of September 2020. This work plan corresponds to a total of 930 hours of dedication, achieved with 30h weekly dedication. The distribution of each task group and the two set milestones corresponding to the digital deposit of the project document and the final presentation/defense is presented in Table 1.1.

Table 1.1: Gantt Chart of 31 weeks, including the main task groups identified from the specific objectives of the project, consultation meetings and the preparation of the final presentation.

TASK GROUP	JAN		FEB				MAR				APR					MAY					JUN				JUL		SEP				OCT		
	W1	W2	W3	W4	W5	W6	W7	W8	W9	W10	W11	W12	W13	W14	W15	W16	W17	W18	W19	W20	W21	W22	W23	W24	W25	W26	W27	W28	W29	W30	W31		
Consultation meetings	●		●		●		●	●	●	●	●	●	●	●	●	●	●	●	●	●	●	●	●			●	●	●	●		●		
Literature review																																	
Academic writing																																	
Visibility diagnostic																																	
Model evaluation																																	
Impact Assessment for aviation																																	
User product proposal																																	
Project presentation																																	



## 2 Scientific background

This chapter presents the scientific basis and the role that aerosols play in the Earth system, with an emphasis on desert dust aerosols. In addition, it summarises the impacts that SDS provoke in different socio-economic sectors. Furthermore, it provides an overview of the different methodologies and tools utilised in desert dust research, as well as for monitoring and operational purposes, and comments the international initiatives that serve the demand for quality desert dust products.

### 2.1 Aerosols in the Earth System

Atmospheric aerosols also referred to as particulate matter, are liquid or solid particles suspended in the atmosphere with diameters ranging from 1nm to 100  $\mu\text{m}$ . Aerosols provoke a radiative effect either directly, due to the scattering and absorption of solar and thermal radiation or indirectly, with the modification of the microphysical and radiative properties and amount of clouds (Tegen, 2003; Balkanski *et al.*, 2007; Andreae and Rosenfeld, 2008; Heinold *et al.*, 2008).

Although most aerosols are found in the lower troposphere, the radiative effect they may produce is sensitive to the vertical distribution of the particles. Furthermore, it depends on their spatial distribution, chemical composition, size, and shape. Therefore, the accurate estimation of this effect can result challenging, from both the observational and theoretical point of view and it is accompanied by high uncertainty.

The Intergovernmental Panel on Climate Change (IPCC) has conducted estimations of the aerosol radiative forcing (RF) as part of the study of the influence of external factors on climate. These estimations have been presented in different Assessment Reports (*SAR*, *TAR*, *AR4*, *AR5*) and were conducted taking into account three aerosol effects: i) the direct effect related to aerosol-radiation interaction, ii) the indirect effect related to aerosol-cloud interaction and iii) the aerosol impact on the cryosphere, related to the decrease of the snow and ice surface albedo. The RF of aerosols is estimated based on in-situ and remote observations and calculations from numerical models that represent the observed processes. The RF of the total aerosol effect in the atmosphere relative to 1750 was estimated at the Fifth Assessment Report of the IPCC to be  $-0.9$  [  $-1.9$  to  $0.1$  ]  $\text{W} \cdot \text{m}^{-2}$ . This estimation results from the negative forcing from most aerosol species and the positive contribution of black carbon and it includes cloud adjustments due to aerosols, as it can be observed in Figure 2.1. It is also highlighted that the aerosols RF calculation contributes the largest uncertainty to the total RF estimations, compared to other atmospheric drivers of climate change.



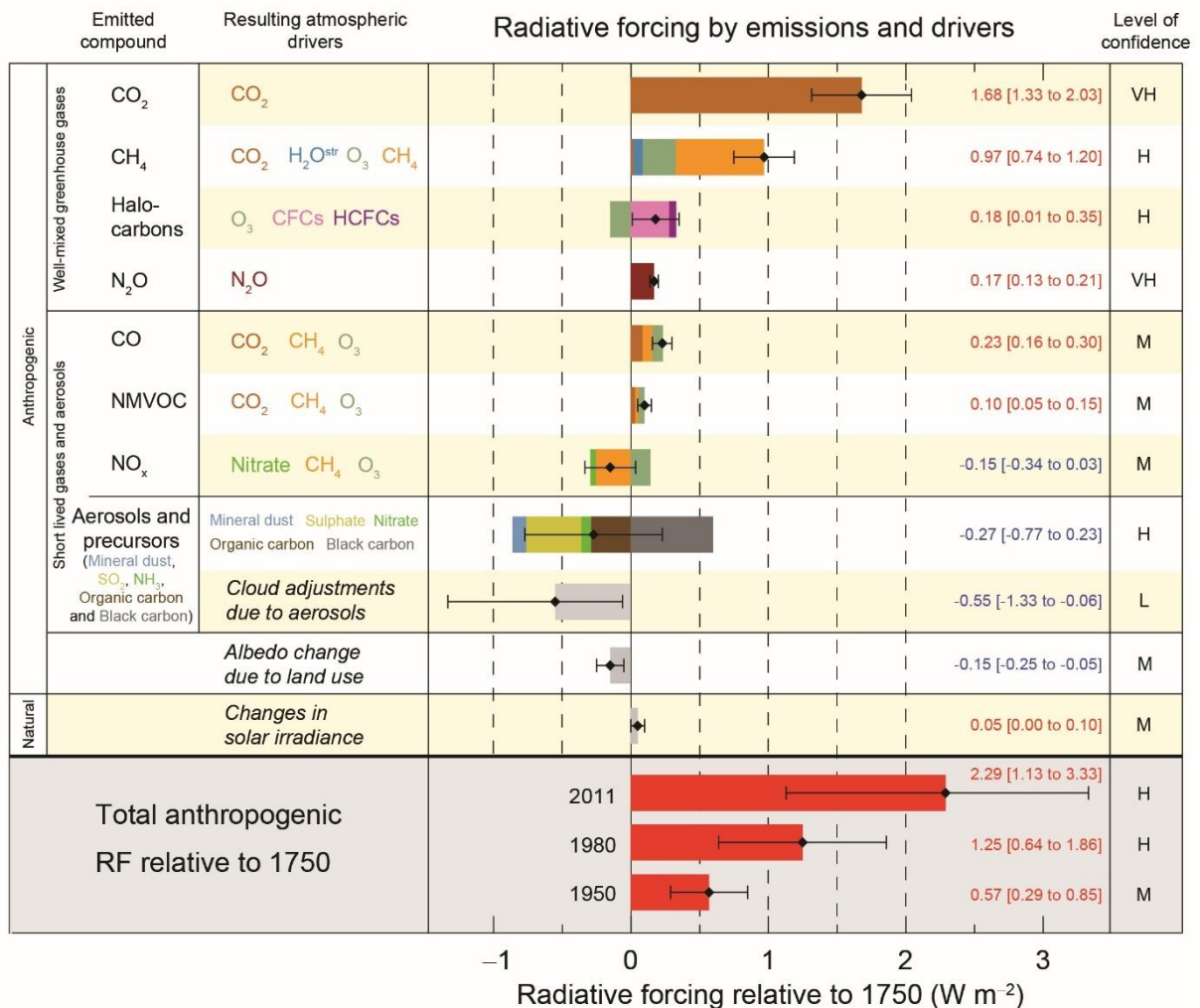


Figure 2.1: Global radiative forcing estimates in 2011 relative to 1750 and their uncertainties for the main drivers of climate change. The best estimates of the net radiative forcing are shown as black diamonds with the corresponding uncertainty bars; the confidence level in the net forcing is characterised as VH – very high, H – high, M – medium, L – low or VL – very low. Albedo forcing due to black carbon on snow and ice is included in the black carbon aerosol bar. Total anthropogenic radiative forcing is provided for three different years relative to 1750. Extracted from: IPCC AR5 Summary for Policymakers, 2013

Atmospheric particles undergo physical and chemical changes during their residence time in the atmosphere and are largely removed by precipitation. The residence time of atmospheric aerosols varies for the different species and ranges from 1 day to 1 week, according to estimations from the AeroCom models (Textor *et al.*, 2006; Huneus *et al.*, 2011), while their concentration is maxima near the emission sources.

Aerosols can be classified, according to their origin, into natural and anthropogenic. The aerosols of natural origin are classified according to their chemical composition into mineral dust, sea-salt, biological particles, volcanic aerosols, sulfate or nitrate aerosols and biomass burning aerosols, among others and are of great importance for the Earth system. As it is mentioned in the IPCC Fifth Assessment Report, mineral dust and sea-salt are globally the most

abundant in mass aerosol species. Furthermore, at the same report, it is stated that mineral dust is found to be the dominating species of atmospheric aerosols over large areas of the Earth, accounting for about 35% of the total aerosol mass with a diameter smaller than 10  $\mu\text{m}$ .

Aerosols can act as cloud condensation nuclei (CCN) and as ice formation nuclei (IN), depending on their size, shape, and chemical composition. They also affect the amount and location of precipitation by influencing the growth of ice crystals and cloud droplets in the atmosphere (Yin *et al.*, 2002; Andreae and Rosenfeld, 2008). Additionally, the modification of the microphysical composition of the clouds due to aerosols, changes their ability to absorb solar radiation, thus affects indirectly the energy reaching the Earth's surface (Boucher *et al.*, 2013). Moreover, since they can absorb and scatter short-wave solar radiation and absorb long-wave thermal radiation, they also interfere directly with the Earth's energy balance. Also, atmospheric aerosol deposition can affect the Earth's albedo by reducing the reflection ability of mainly snow and ice surfaces and can act as an important source of nutrients to many continental and marine ecosystems, having both positive and adverse impacts on biogeochemical cycles (Mahowald *et al.*, 2017).

## 2.2 The Dust Cycle

According to Kohfeld and Tegen (2007), “dust particles are a combination of irregular-shaped mineral grains such as quartz, feldspars and calcite, clay minerals rich in elements such as aluminium, and oxides and hydroxides rich in elements such as iron”, they are formed in arid and semi-arid soils and are emitted into the atmosphere through wind erosion. The chemical composition of dust particles strongly depends on the source region and their chemical and physical properties are bound to change during atmospheric transport. Airborne dust can be transported hundreds to thousands of kilometres away, depending on the size of the particles and becomes visible in the atmosphere as haze. African dust has been observed over both North and South America (Prospero, Glaccum and Nees, 1981; Perry *et al.*, 1997; Prospero, 1999), and over the Indian Ocean (Meywerk and Ramanathan, 1999). Likewise, several case studies have detected soil-derived particles from Asian deserts in the Pacific islands (Duce *et al.*, 1980; Parrington, Zoller and Aras, 1983), in North America and Greenland (Biscaye *et al.*, 1997; Reader, Fung and McFarlane, 1999; Bory *et al.*, 2002, 2003), and even in Northern Europe (Ansmann *et al.*, 2003).

Our understanding of the present-day dust sources is largely based on the information derived from satellite and ground-based remote sensing observations, dust monitoring networks and numerical models. During the past decades, there

has been a continuing effort to estimate the global dust emission and the intensities of the different dust sources. According to Shao *et al.* (2011) recent estimates range from  $1000 \text{ Tg yr}^{-1}$  to  $5000 \text{ Tg yr}^{-1}$ , converging to a value between 1000 and  $2000 \text{ Tg yr}^{-1}$  (Shao *et al.*, 2011), while Ginoux *et al.* (2012) estimated the global annual emissions to be  $1536 \text{ Tg yr}^{-1}$ .

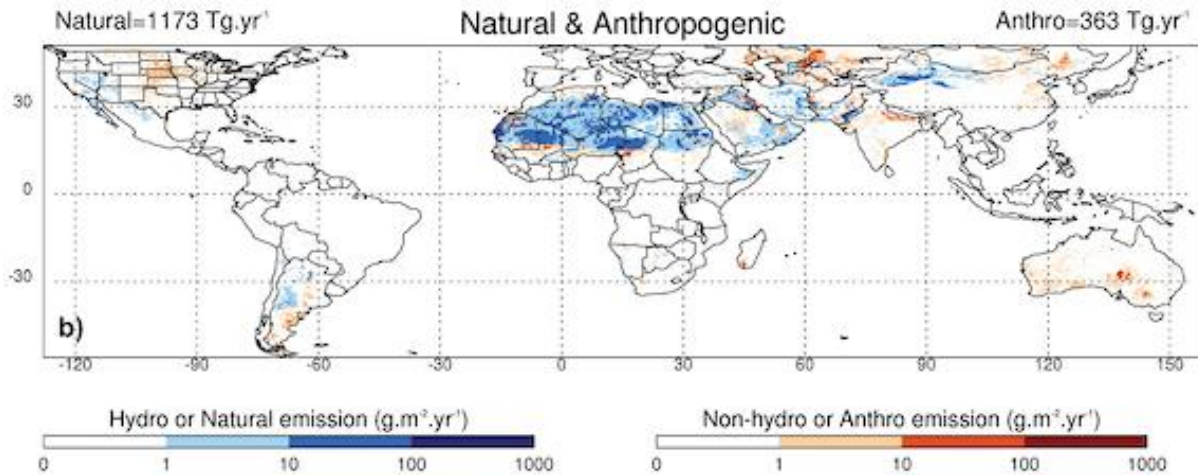


Figure 2.2: Annual mean dust emission based on Moderate Resolution Imaging Spectroradiometer (MODIS) Deep Blue estimates of dust optical depth in conjunction with other data sets including land use. Extracted from Ginoux *et al.* (2012)

As it can be observed in Figure 2.2, the major large-scale sources of desert dust are located in the desert areas of the Northern Hemisphere, in the dust belt that extends from the Eastern Subtropical Atlantic eastwards through the Sahara Desert to Arabia and Southwest Asia (Middleton and Goudie, 2001; Prospero *et al.*, 2002; Luo, 2004; Badarinath *et al.*, 2010; Ginoux *et al.*, 2012). Other significant sources can be found in the Australian, North and South American and South African deserts (Formenti *et al.*, 2001; Washington *et al.*, 2003), but the largest contributions of dust are emitted from North Africa (55%) mostly from the Sahel (Ginoux *et al.*, 2012). According to the model intercomparison of 15 global aerosol models within the AeroCom project, the range of possible emissions from North Africa is suggested to be from  $400$  to  $2200 \text{ Tg yr}^{-1}$ , while in the Middle East is estimated to be between  $26$  and  $526 \text{ Tg yr}^{-1}$  (Huneeus *et al.*, 2011).

While deserts constitute the main natural sources of dust, human activity can also induce dust emissions. Mahowald *et al.* (2010) have shown that dust load may have doubled in the 20th century due to anthropogenic activities. Poor land management and agricultural methods, in combination with desertification factors induced by climate change, can lead to the creation of anthropogenic sources, summing to the emission of desert dust on global scale. Anthropogenic dust emissions remain ill quantified although some satellite observations suggest the fraction of desert dust due to land changes could be 20% to 25% of the total

(Ginoux *et al.*, 2012). Anthropogenic activities may also affect dust emission indirectly, particularly through their effects on climate. Climate change is an important potential driver of future wind erosion and dust storm occurrence, especially via more extreme wind events, greater frequency of droughts and greater aridity in some areas (IPCC, 2012; Dai, 2011).

The desert dust cycle involves dust emission, transport, transformation and deposition (Shao *et al.*, 2011). Desert dust particles are entrained into the atmosphere by wind shear, they are transported by synoptic and global circulation over a variety of distances, they react and mix with anthropogenic air pollutants and other components of the atmosphere, such as clouds, they scatter and absorb radiation and they finally return to the surface, land or ocean, due to wet or dry deposition (Figure 2.3).

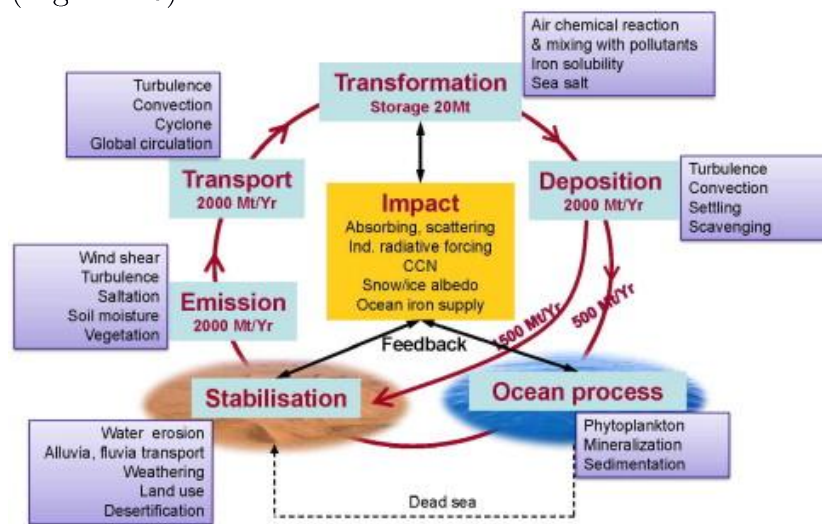


Figure 2.3: The dust cycle in the Earth system and the main processes in which dust plays an important role. Extracted from: Shao *et al.*, 2011

Desert dust emission is an overly complex process that responds to a variety of environmental factors in a non-linear way. Therefore, the emission of desert dust particles is highly variable on spatial and temporal scales. The main requirements for the emission of dust particles are the following: i) the soil surface must be dry and sparsely vegetated, ii) the presence of substantial concentrations of relatively large particles on the surface that the wind can drag and carry away (entrainment) is essential, iii) the presence of strong winds is necessary. A correct estimation of dust fluxes requires precise knowledge of the surface properties of the soil, which for many of the main source areas is unavailable or poorly detailed.

There are several meteorological mechanisms, each with its own diurnal and seasonal features, occurring at a wide range of spatiotemporal scales (i.e. synoptic, mesoscale and microscale) that potentially control strong winds and cause SDS (Knippertz and Stuut, 2014). Some of the meteorological phenomena that influence the apparition of SDS are the following: i) Large-scale monsoon-type flows, such as the Harmattan in Sahel in winter; ii) mobile synoptic-scale systems



such as anticyclones, cyclones and cold fronts; iii) gust fronts generated by convective storms, also known as haboobs; iv) intense dry convection that leads to the generation of dust devils and dusty plumes.

The main routes of global desert dust transport are presented in Figure 2.4, together with the locations of the major deserts of the Earth. Additionally, the magnitudes of desert dust emission from different regions are indicated using bars and the deposition to the oceans using thick arrows. In the case of Saharan dust, there are four main trajectories (D’Almeida, 1986; Engelstaedter, Tegen and Washington, 2006; Klose *et al.*, 2010): i) southward transport over the Sahel and the Gulf of Guinea (60% of the emissions); ii) western transport to the Atlantic ocean (25%); iii) northward transport to Europe (10%); iv) eastward transport to the Middle East (5%).

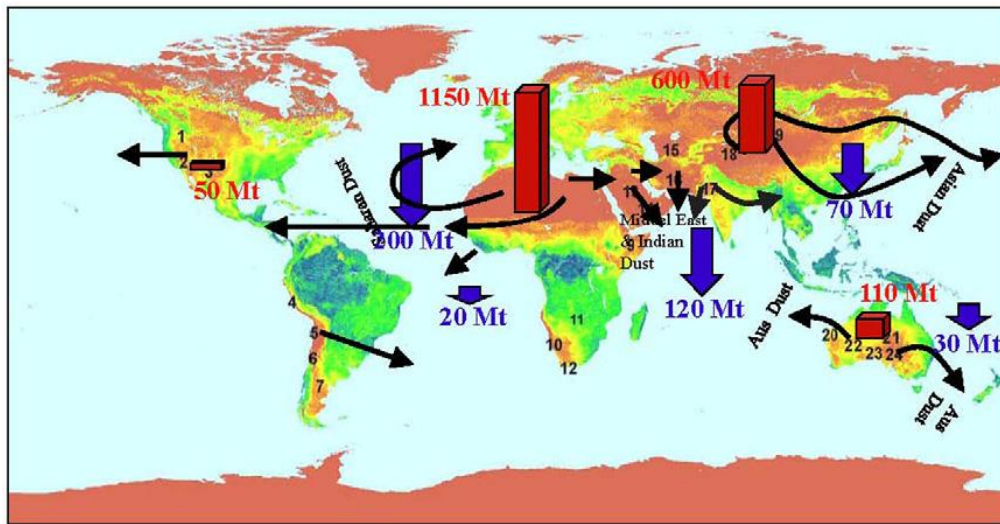


Figure 2.4: Pattern of global dust transportation and locations of the main deserts, including: (1) Great Basin, (2) Sonoran, (3) Chihuahuahua, (4) Peruvian, (5) Atacama, (6) Monte, (7) Patagonia, (8) Sahara, (9) Somali-Chabli, (10) Namib, (11) Kalahari, (12) Karroo, (13) Arabian, (14) Rub al Khali, (15) Turkestan, (16) Iranian, (17) Thar, (18) Taklimakan, (19) Gobi, (20) Great Sandy, (21) Simpson, (22) Gibson, (23) Great Victoria and (24) Sturt; Extracted from Shao *et al.* (2011)

Early measurements of desert dust deposition over land have shown deposition rates from  $3.5 \text{ g m}^{-2} \text{ yr}^{-1}$  in Japan to  $200 \text{ g m}^{-2} \text{ yr}^{-1}$  in the Niger (Goudie, Livingstone and Stokes, 1999). Dust deposition is generally lower over the oceans, while there are two areas of maximum deposition: one in the North Atlantic due to Saharan dust and one in the North Pacific due to Asian dust. Dust deposited over the oceans have been shown to boost primary production in marine ecosystems due to the release of iron and other nutrients (Duce and Tindale, 1991; Mahowald *et al.*, 2005). Additionally, African and Asian dust may have harmful effects on coral reefs in global scale (Garrison *et al.*, 2003). Dust deposited over land provides nutrients to terrestrial ecosystems: Saharan dust fertilises the Amazon rainforest (Yu *et al.*, 2015), while desert dust from central Asia contributes nutrients to the Hawaiian rainforest (Chadwick *et al.*, 1999).

## 2.3 Sand and Dust Storms

### 2.3.1 Defining sand and dust storms

SDS are formally defined by the WMO as “an ensemble of particles of dust or sand energetically lifted to great heights by a strong and turbulent wind”. It is the meteorological phenomenon that occurs when strong winds lift large amounts of sand and dust from dry, sparsely vegetated soils into the atmosphere. It results in visibility reduction at eye level (1.8 meters from the ground) to less than 1km (McTainsh and Pitblado, 1987). While, traditionally, the severity of dust events is defined using visibility limits, no strict and unanimous definition exists in global scale. Hence, SDS definitions deriving from visibility reduction limits vary among different countries and authorities. An alternative way to define the severity of the dust events is the dust storm index that apart from visibility reduction, includes factors such as the frequency and duration of dust events, as well as the wind speed (O’Loingsigh *et al.*, 2014).

Other dust events, less severe than SDS have been defined considering the WMO synoptic codes for present weather and the associated visibility ranges. To mention a few: i) dust haze, ii) drifting sand or dust, iii) blowing sand or dust and iv) dust whirls, also referred to as dust devils. Dust haze refers to the suspension of dust and sand particles in the air, that have been raised by an SDS occurring either at or near the observation site. Drifting dust or sand refers to dust or sand raised by the wind to small heights above the ground without causing visibility reduction at eye level. The motion of the particles occurs in horizontal level, more or less parallel to the ground. Blowing sand or dust refers to dust or sand particles raised to moderate heights above the ground and it is accompanied by a slight reduction of visibility at eye level to 1-10 km. Dust whirl refers to an ensemble of dust or sand particles raised vertically in a whirling column of a small diameter and a varying height (typically around 30m and up to 1km) and they occur when the near-ground air is unstable.

### 2.3.2 Impacts related to Sand and Dust Storms

Atmospheric desert dust plays a significant role in weather, climate, and atmospheric chemistry, as it is described in section 2.2. Therefore, desert dust events and particularly SDS impact air quality, human health, and various socio-economic sectors in numerous ways, such as energy and transportation.

Although airborne desert dust comes from arid and semi-arid regions, where SDS are generated, it can be transported hundreds to thousands of kilometers away, provoking impacts in wide spatial and temporal scales. Hence, dust-related impacts can occur both in-site (source regions) and off-site (impact regions). The fact that the source and impact regions can be separated by long distances makes

SDS a unique type of natural hazard and adds complexity to relevant impact assessment studies.

Such impact assessment studies aim to evaluate the diverse impacts of airborne desert dust, considering all inter-related environmental and socio-economic impacts, both beneficial and adverse. A hazard is any agent that can cause harm or adverse effects to humans, infrastructure, livestock, or the environment. One key concept in identifying environmental hazards is the definition of appropriate thresholds, above which the related impact represents a hazard for living organisms or the environment. The likelihood of an adverse effect, taking place as a result of the hazard, provides the definition of risk.

Various researchers have studied the implications that airborne desert dust presents for human health due to its biological, chemical, and physical properties (Zhang *et al.*, 2016). Exposure to dust can cause eye or skin irritation, conjunctivitis, coughing and sneezing, while inhalation of dust particles has been associated with both respiratory and cardiovascular diseases. Additionally, epidemiological studies show that dust exposure is potentially associated with increase in mortality (Giannadaki, Pozzer and Lelieveld, 2014) and hospital admissions. Desert dust can contain a wide variety of microorganisms, bacteria and fungi, thus acts as a transmission agent for diseases like meningococcal meningitis in sub-Saharan Africa (García-Pando *et al.*, 2014; Jusot *et al.*, 2017) valley fever in North and South America (Sprigg *et al.*, 2014; Tong *et al.*, 2017) and the Kawasaki disease in Asia (Rodó *et al.*, 2014).

Regions located in the pathway of desert dust transportation report increased ambient PM concentrations, which lead to the deterioration of the local air quality, with negative implications for human health. Hence, monitoring is important to ensure compliance with air quality standards and protection of vulnerable population. Various health authorities have established thresholds for acceptable atmospheric concentration of the coarse and fine fractions of PM at chronic (annual mean) and acute (daily mean) level. However, these air quality limits refer to PM in general and desert dust particles are by no means the only source of PM in the atmosphere.

Concerning the solar energy production sector, the deposition of desert dust affects the two main technologies that are used, photovoltaic (PV) and concentrating solar-thermal power (CSP) systems (Sarver, Al-Qaraghuli and Kazmerski, 2013), directly as it reduces the solar radiation that reaches the panels, and indirectly, since desert dust particles interfere with cloud formation. Energy losses can reach up to 80% for CSP and up to 50% for PV installations (Kosmopoulos *et al.*, 2017). Another implication of dust deposition over solar

panels is associated with their clean-up and the scarcity of water resources in desert areas, leading to the demand of adopting effective water management strategies.

Major cities also tend to host transport infrastructures, as airports with significantly high aircraft activity and major road transport systems. SDS can increase accidents in the air and on the ground, due to poor visibility or mechanical damages. The term visibility indicates the distance to which human visual perception is limited by atmospheric conditions and describes the transparency of the air in the horizontal direction, which can be affected by the presence of hydrometeors, such as rain, snow, fog or mist and lithometeors, such as desert dust.

Regarding ground transportation, circulation can be affected by road closures due to either poor visibility or dust deposition on the road surface and various studies have shown a clear correlation between SDS and traffic accidents (Al-Hemoud *et al.*, 2017). Regarding aviation, airports located in areas commonly affected by SDS are obliged to close during intense SDS, causing flight delays or cancellations, while they need to apply special take-off and landing protocols and re-assess their flight management strategies. Additionally, aircrafts flying over dusty areas require more frequent maintenance, which results in additional costs for the airline companies. Since the present work focuses on the aviation sector, a more detailed description of the impacts is given in chapter 5.

## 2.4 Dust short-term operational services

During the past 40 years, the importance of the desert dust cycle and its role in the Earth system has been widely recognised within the scientific community and has sparked the interest of researchers from diverse disciplines to study the far-reaching implications of dust to the environment. Desert dust research has stimulated the integration of disciplines, including geomorphology, soil physics, meteorology, fluid dynamics, air chemistry and ocean biology (Shao *et al.*, 2011). It has also involved the combination of different methodologies and tools, ranging from satellite and ground-based observations, numerical modelling, data assimilation, Geographical Information Systems (GIS) analyses, field campaigns and laboratory experiments.

### 2.4.1 Dust forecasting

A variety of regional and global models of the desert dust cycle have been developed since the early 1990s (Tegen and Fung, 1994; Marticorena and Bergametti, 1995; Ničković *et al.*, 1996). Dust models predict desert dust emission, transport, and deposition. The base is always an atmospheric host model that includes the relevant physical processes, such as advection, convection, turbulent



diffusion, radiation, and interaction with clouds, as well as some parameterisations for land, ocean and ice surfaces. Upon this base, the desert dust module is developed to simulate desert dust emission, transport, deposition, and chemistry. The dust module solves the conservation equation, using surface boundary conditions.

Dust models that are coupled online or offline with short and medium-range weather forecast models aim to provide desert dust forecasts for up to 3 - 5 days. On the other hand, those coupled with climate models focus on the accurate representation of the seasonally dependent desert dust cycle, as well as on the global scale effects of the desert dust radiative forcing on climate. Several models use data assimilation techniques, combining measurements and model estimates in order to achieve more accurate predictions. It is through the model evaluation and validation that it is possible to provide a measure of confidence and accuracy of the derived forecast products, but also model evaluation is vital for the further model development.

#### 2.4.2 Dust observations

Several state-of-the-art instrumentation techniques have been developed to monitor the physicochemical and optical properties of aerosols, improving remote sensing technologies and ground-based and satellite measurements. Dust observations are mainly bulk-aerosol information from satellite measurements and ground-based stations. Alternative sources of dust information, as surface visibility synoptic observations (SYNOP) and meteorological aerodrome reports (METAR), can be used as a proxy for dust concentration at the surface.

Satellite observations play a key role in describing the horizontal distribution of desert dust particles and their transport in the atmosphere. The principal quantitative indicator of the horizontal distribution of columnar dust amount determined by most instruments is the aerosol optical depth (AOD), which is related to the amount of light, aerosols scatter or absorb in a vertical column through the atmosphere. Since AOD is related to all kinds of aerosols, additional information is needed to identify specific aerosol species, which can be obtained using the Ångström exponent (AE). AE describes the spectral dependence of AOD relative to various wavelengths of light, hence provides information on the size distribution of the aerosol particles and therefore, an estimation of the species that are present. Therefore, dust-related AODs can be derived from observations at different wavelengths, from the ultra-violet to the near infra-red, obtained from MODIS (Remer *et al.*, 2005; Sayer *et al.*, 2013), VIIRS (Jackson *et al.*, 2013), OMI (Torres *et al.*, 2007), SeaWIFS (Hsu *et al.*, 2012; Sayer *et al.*, 2012) and SEVIRI (Carrer *et al.*, 2010; Banks and Brindley, 2013) sensors. Nowadays, different algorithms exist to obtain information for different types of surfaces, such as the Dark-Target method (Levy *et al.*, 2010) for observations over non-

desert territories and the Deep Blue approach for measurements over deserts and vegetated surfaces, processing data from several sensors, such as the MODIS (Moderate-Resolution Image Spectroradiometer), the SeaWiFS (Sea-Viewing Wide Field-of-View Sensor) and the VIIRS (Visible Infrared Imaging Radiometer Suite) sensors. In addition to that, the vertical distribution of aerosols in the atmosphere can be obtained at high spatial resolution from the CALIOP (Cloud-Aerosol Lidar with Orthogonal Polarization) lidar, that has been added to CALIPSO (Cloud-Aerosol Lidar and Infrared Pathfinder Satellite Observations) satellite in 2006 (Winker, Hunt and McGill, 2007).

All mentioned satellite products are highly valuable for dust modelling and monitoring, either for evaluation (Cuevas *et al.*, 2015) or data assimilation purposes (Di Tomaso *et al.*, 2017). Amongst them, the MODIS Dark Target and Deep Blue retrievals should be highlighted, due to their high spatial coverage and high quality (Ginoux *et al.*, 2012) and the CALIOP products (Amiridis *et al.*, 2015), for the highly valued vertical profiles they provide.

Remote sensing observations derive from photometers and lidar methods. Photometers are instruments widely used in aerosol studies, that provide information on aerosol optical depth and sky radiance, thus information on the microphysical properties of the particles can be retrieved and the presence of dust particles can be identified. There are two sources that have integrated photometers and provide freely accessible centralised databases with calibrated and quality assured data: i) the Global Atmospheric Watch (GAW) programme through the Precision Filter Radiometer (PFR) and ii) the Aerosol Robotic Network (AERONET) through the Cimel photometer. AERONET is a global network of ground-based solar photometer stations, measuring AOD in multiple spectral channels. It is one of the most densely populated networks and provides information about the content and type of aerosols in the atmospheric column.

Light detection and ranging (lidar) methods provide information about the vertical structure and distribution of the atmosphere in high resolution. Concerning dust aerosols, lidars provide information on the distribution of dust particles in the atmosphere and therefore lidar measurements are ideal to monitor the long-range transport of dust, to investigate the mixing processes of dust particles with other types of aerosols and to study the aerosol/cloud interaction (Mona *et al.*, 2012). Different techniques of different complexity for the investigation of aerosol properties using lidars exist, such as the elastic backscatter lidar, also known as ceilometer, the multi-wavelength Raman lidar and the High Spectral Resolution Lidar (HSRL). Concerning important networks offering information on aerosol properties using lidar techniques, the following should be mentioned: the European Network  $\alpha$ -profile, that provides information from

ceilometers in near-real-time, and the European Aerosol Research Lidar Network (EARLINET), which is the first aerosol lidar network that operates multi-wavelength Raman lidars in Europe since 2000 with 31 active stations, offering quality assured measurements of the aerosol backscatter and extinction coefficient and therefore, AOD.

In contrast to columnar information obtained by satellite measurements or remote sensing observations, in-situ ground-based stations provide observations that are relevant for near-surface characterisation of dust, mainly measuring surface mass concentration of particulate matter (PM). Estimations of the dust concentration at ground level derive from the measurement of  $PM_{10}$  (particulate matter with diameters of  $10\mu m$  or less) and  $PM_{2.5}$  (particulate matter with diameters of  $2.5\mu m$  or less) mass concentrations provided by air quality networks. Various networks and international research programmes are established in Europe, offering such measurements, among them the European Monitoring and Evaluation Program (EMEP), the Aerosols, Clouds and Trace Gases Research Infrastructure (ACTRIS), the Global Aerosol Watch (GAW) and the European environment Information and Observation NETwork (EIONET), whereas in Northern Africa and the Middle East the only network that provides appropriate PM measurements is the Sahelian Dust Transect (SDT), a monitoring network of mineral dust in the Sahel.

While in Europe there are numerous  $PM_{10}$  and  $PM_{2.5}$  mass concentration measurements, NAME presents some particularities related to the availability of observations. More specifically, the air quality stations that can be found in the NAME area are mostly part of urban air quality monitoring networks and therefore, their observations include anthropogenic aerosols. Hence, the dust contribution to the measured quantities is difficult to be estimated and there is a necessity for using different variables as an alternative for the evaluation.

Visibility data included in meteorological observations can be used as an alternative way to monitor dust concentration due to their better spatial and temporal coverage of data sets of weather records (Terradellas et al., 2014). In this case, it is of crucial importance to complement the use of visibility data with weather information to discard the cases of reduced visibility due to the presence of hydrometeors. The scarcity of ground-based networks in NAME becomes evident in Figure 2.5. In areas with low density of air quality stations, such as the Saharan and the Arabian deserts, horizontal visibility data from meteorological reports (METAR and SYNOP) can be used, as an alternative, to obtain surface dust concentration, due to their better spatial and temporal coverage. An important source of such datasets can be found in the Integrated

Surface Database (ISD) of the National Oceanic and Atmospheric Administration (NOAA).

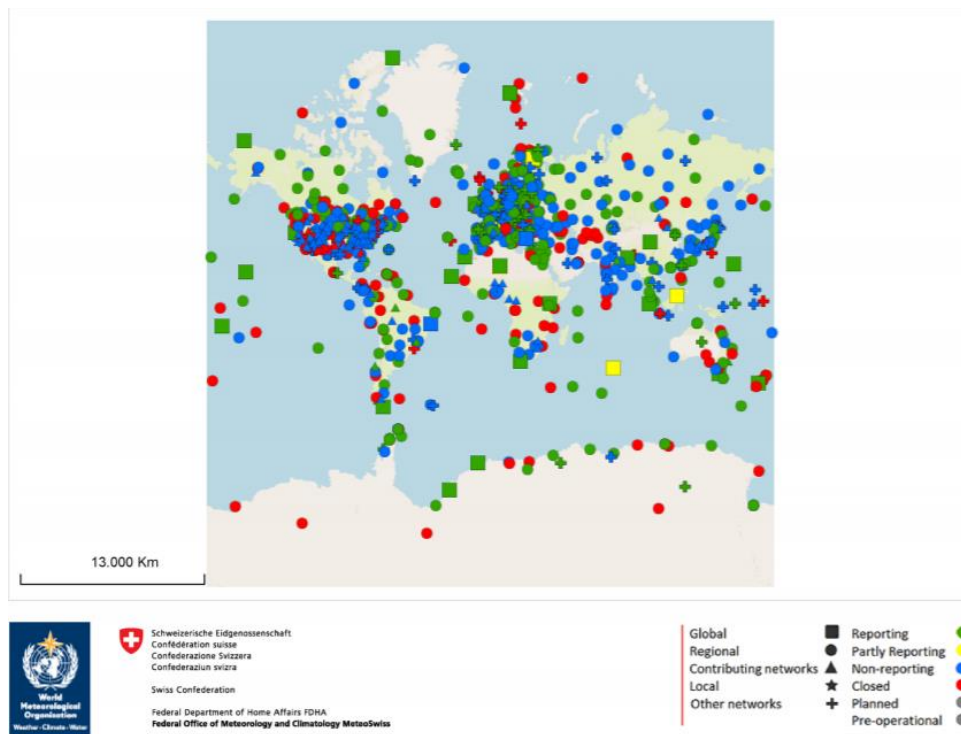


Figure 2.5: Map of surface stations currently included in GAW. Extracted from: Benedetti et al., 2018, courtesy of MeteoSwiss.

Numerous experimental campaigns have been carried out in dust-prone regions with the aim to characterise mineral dust. Field campaigns collect ground-based and airborne observations, deriving from a set of instrumentation operated in high temporal frequency for a continuous but limited amount of time. Most experimental campaigns have a duration of a few weeks and aim to document fundamental variables related to dust research, such as mass concentration, size distribution, and scattering, absorption and extinction coefficients, that can be used to build datasets useful for model evaluation on specific case studies and to support model developments.

Concerning operational requirements in data, it is highlighted that not all the above-mentioned observational datasets are suitable for operational purposes. Ease of access through centralised data repositories, low uncertainty, and timely delivery (6-24h) are essential to guarantee their use for data assimilation or routine model evaluation. When performing near-real-time (NRT) evaluation (also known as *verification*) for aerosols and particularly for dust, the most widely used network of ground observations is AERONET, as it provides highly accurate measurements of AOD, and information on the aerosol size distribution, from over 600 sites around the world. Concerning PM<sub>10</sub> and PM<sub>2.5</sub> mass concentrations, measurements provided by EEA are suggested for evaluation purposes in Europe. In source regions in North Africa and the Middle East, the lack of surface aerosol

observations justifies the use of other indirect dust observations, such as visibility measured in airports.

### 2.4.3 International initiatives on dust forecasting and monitoring

The considerable impacts that SDS provoke to a wide range of sectors trigger the demand for reliable dust-related information. The progress of the scientific community regarding dust prediction and monitoring, the increasing accuracy of the numerical prediction models and the variety and improved quality of observations, demonstrate the maturity of the available dust products and their suitability as decision-making tools for the most affected sectors.

Various international initiatives have been established to serve this demand; amongst them the Copernicus Atmosphere Monitoring Service (CAMS) of the European Union, that provides 5-day dust aerosol forecasts for global and regional domains as well as observations, the ensemble aerosol global forecast, that includes desert dust, of the International Cooperative for Aerosol Prediction (ICAP; Xian *et al.*, 2019), and the multi-model ensemble desert dust regional forecasts of the WMO Sand and Dust Storm Warning Advisory and Assessment System (SDS-WAS).

The WMO SDS-WAS was initiated in 2007 in response to the demand of 40 WMO countries for more reliable sand and dust storm forecasts and their intention to enforce their capability to predict dust events. The SDS-WAS provides access to forecasts, observations, and scientific knowledge. It aims to improve forecasting and observation technology through research and to enhance the operational forecasts with the latest technology available. Additionally, it consults the user communities to identify and further improve the products offered and it promotes the use of the SDS-WAS products among relevant countries to meet societal needs. Finally, it strives to build bridges between SDS-WAS and other scientific communities that conduct aerosol-related research.

The SDS-WAS is established as a federation of partners organised in three regional nodes: the Northern Africa- Middle East- Europe (NAMEE) node, the Asian node, and the Pan-American node. The NAMEE node was created in 2010 in Barcelona, Spain and it is jointly managed by the Spanish State Meteorological Center (AEMET) and the Barcelona Supercomputing Center (BSC). The NAMEE Regional Center provides daily dust forecasts, covering the main source areas in Northern Africa and the Middle East, as well as the main transport routes and deposition zones. Besides, the Regional Center hosts a variety of activities and capacity building events that promote knowledge transfer, networking, and collaboration among its members.



Considering the good results obtained by the SDS-WAS and to meet the demand for specialised meteorological services, the Regional Specialised Meteorological Center with activity specialisation on Atmospheric Sand and Dust Forecast (RSMC-ASDF) was created in Barcelona, Spain. The **Barcelona Dust Forecast Center**, as it is named, generates and distributes operational dust predictions for the Northern Africa, Middle East and Europe domain, bounded by the following coordinates: longitude 25°W to 60°E and latitude 0° to 65°N (Figure 2.6), since March 2014 and it is hosted by the consortium formed by AEMET and the BSC. Its objectives are aligned with the mission of the WMO SDS-WAS programme.

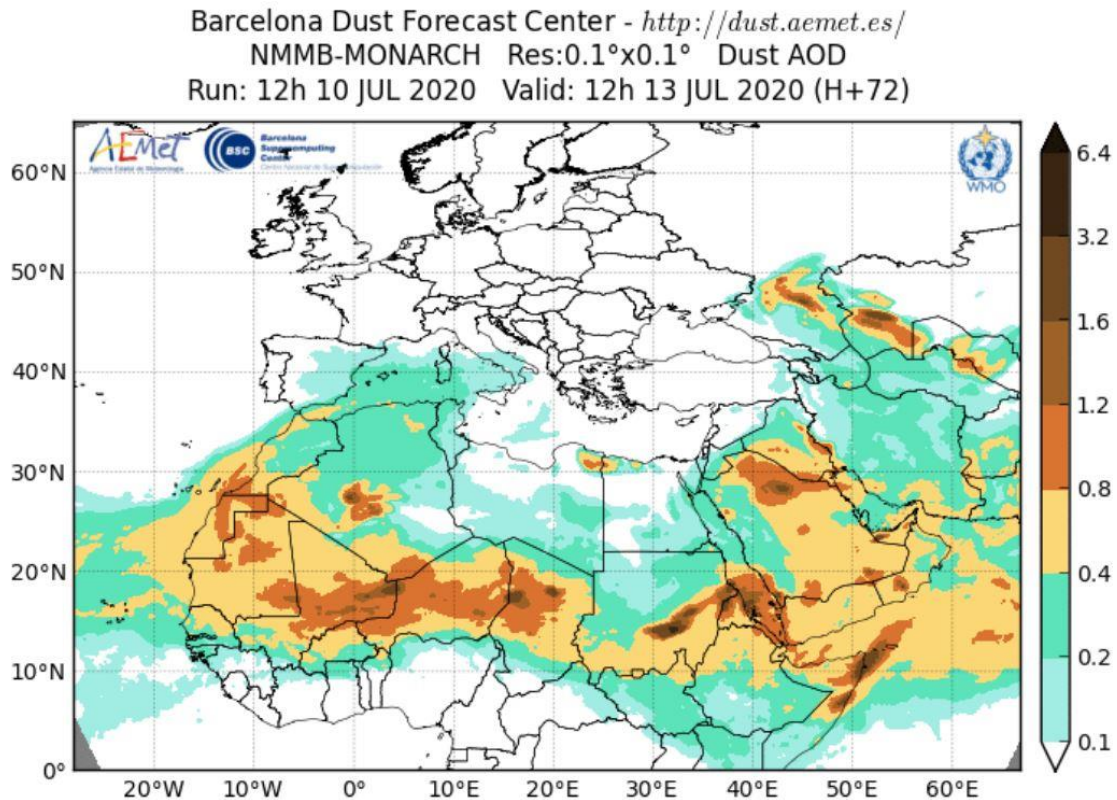


Figure 2.6: Dust AOD forecast offered by the Barcelona Dust Forecast Center, depicting the reference domain, bounded by the following coordinates: longitude 25°W to 60°E and latitude 0° to 65°N. Extracted from: Barcelona Dust Forecast Center official webpage (<https://dust.aemet.es/>)

Furthermore, SDS have received increasing attention by policymakers, that have recognised their impacts on the environment, health, agriculture and socio-economic well-being as potential challenges in achieving the Sustainable Development Goals (SDG) of the United Nations (UN) both in developed and developing countries. Hence, in 2018 the UN proceeded to the formation of the Coalition to Combat Sand and Dust Storms as an endeavor to strengthen the cooperation on desertification, dust storms, land degradation and drought and to promote disaster risk reduction. The Coalition consists of 15 nominated UN agency Focal Points, amongst them the WMO that is responsible for the Forecasting and Early Warning systems.

### 3 Methodology

This chapter presents the main tool utilised to perform the tasks included in the work plan, which is the NMMB-MONARCH model, and provides a general overview of the methodology applied for the model evaluation and the assessment of the SDS impacts on civil aviation, while a more detailed description of the specific methods employed in each task is given in Chapters 4 and 5.

#### 3.1 NMMB-MONARCH description

The Multiscale Online Nonhydrostatic Atmosphere Chemistry model (NMMB-MONARCH), developed at the Barcelona Supercomputing Center (BSC), is an online meteorology-chemistry model that provides short- and mid-term chemical weather forecasts on both regional and global scales (Pérez *et al.*, 2011; Haustein *et al.*, 2012). The NMMB-MONARCH is based on the online coupling of the meteorological Nonhydrostatic Multiscale Model on the B-grid (NMMB; Janjic and Gall, 2012) developed at the National Centers for Environmental Prediction (NCEP), with a full chemistry module, including gas phase and all aerosol species, developed at the BSC. Therefore, the model is designed to account for the feedbacks among gases, aerosol particles and meteorology. The aerosol module is enhanced with a data assimilation (DA) system to optimally combine forecast with observations and improve predictions. A schematic description of the NMMB-MONARCH modelling system is presented in Figure 3.1.

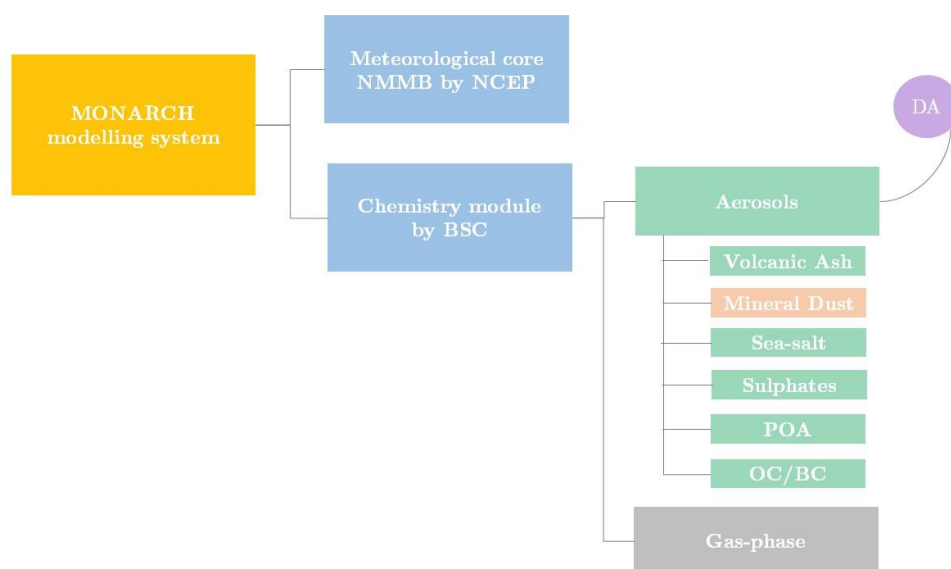


Figure 3.1: Description of the meteorology-chemistry atmospheric NMMB-MONARCH model.

The desert dust module, previously known as NMMB/BSC-Dust, that is embedded into the NMMB meteorological core, solves the mass balance equation for dust taking into account the following processes: i) dust generation and uplift

by the wind, ii) horizontal and vertical advection, iii) horizontal diffusion and vertical transport by turbulence and convection, iv) dry deposition and gravitational settling, v) wet removal, including in-cloud and below-cloud scavenging. The model includes 8 dust size bins from 1 to 10  $\mu\text{m}$  (Pérez *et al.*, 2006).

The desert dust component of the NMMB-MONARCH model has been evaluated at regional and global scales (Ansmann *et al.*, 2017; Pérez *et al.*, 2011; Haustein *et al.*, 2012; Gama *et al.*, 2015). Pérez *et al.* (2011) provides daily to annual evaluations of the model for its global and regional configurations. At global scale, the model lies within the top range of AEROCOM dust models in terms of performance statistics for surface concentration, deposition and aerosol optical depth (AOD). At regional scale, the model reproduces significantly well the daily variability and seasonal spatial distribution of the dust optical depth (DOD) over Northern Africa, the Middle East and Europe. In Haustein *et al.* (2012), the model was evaluated at the regional scale against measurements at source regions from the Saharan Mineral Dust Experiment (SAMUM-I) and the Bodélé Dust Experiment (BoDEx) campaigns. Gama *et al.*, (2015) and Ansmann *et al.*, (2017) show the availability of the model to reproduce seasonal transport over the North Atlantic.

The NMMB-MONARCH model is the reference model of the Barcelona Dust Forecast Center, while it also contributes to the ICAP global operational aerosol multi-model ensemble and the SDS-WAS regional dust multi-model ensemble.

### 3.1.1 Model simulation

For the present analysis, we are using a research configuration of the NMMB-MONARCH model that follows the settings of the operational run of the Barcelona Dust Forecast Center. The regional domain covering NAMEE is selected, with resolution set to  $0.10^\circ$  in the horizontal ( $\sim 10\text{km}$  in Equator), and to 40  $\sigma$ -layers extending up to approximately 15 km in the vertical. The simulated desert dust distributions consisted of daily runs for the years 2018-2019 on 3-hourly basis. The initial state of the dust concentration was defined by the 24-h forecast of the previous day model run. Only in the ‘cold start’ of the model, concentration is set to zero. The cold start of the model was initiated in December 2017. The Global Forecast System (GFS) which is a weather global forecast produced by the National Centers for Environmental Prediction (NCEP) (NCEP/GFS; at  $0.5^\circ \times 0.5^\circ$ ) at 12UTC is used every 24 hours as initial conditions and boundary conditions were updated every 6 hours. Simulations are carried with feedback between dust and radiation.

As a difference to the current operational NMMB-MONARCH configuration considered in the Barcelona Dust Forecast Center, the research experiment used



in the context of the present work uses a new high-resolution mapping of dust sources based on MODIS Deep Blue retrievals (Ginoux *et al.*, 2012). The identification of dust sources is a crucial aspect for the representation of dust mobilisation in models. Traditionally, models used aridity as a criterion to identify potential dust sources. These so-called ‘preferential sources’ are found within enclosed basins, where easily eroded soil particles have accumulated after fluvial erosion of the surrounding highlands.

Preferential source functions based on topography (Ginoux *et al.*, 2001) have significantly improved the skill of models by approximately locating large-scale natural sources. However, this approach is limited to representing small-scale dust sources and regions where the main sources are anthropogenic (cropland and pasture), which can make a significant contribution to the dust load. High-resolution satellite dust-derived retrievals subsequently showed that the most prolific sources occupy only a small fraction of arid regions. The new source map included in the updated model configuration used in the present work is using the dust-derived MODIS Deep Blue dataset based on Ginoux *et al.* (2012).

Both the currently operational NMMB-MONARCH version in the Barcelona Dust Forecast Center and the research experiment used in the present analysis have been compared using dust-filtered DOD AERONET observations for the years 2018 and 2019. The dust-filtering is based on the Angstrom Exponent, which is an optical parameter used for aerosols characterization. Both runs can reproduce the daily variability with annual overall correlation coefficient above 0.70 (0.71 and 0.76 for 2018 and 2019 respectively for the operational run, and 0.77 and 0.76 for 2018 and 2019 respectively for the research experiment), with higher values in long-transport regions as Southern Europe. Underestimations present in the operational run (annual MB of -0.02 for 2018 and 2019) are reduced in the upgraded version that tends to overestimate the DOD AERONET observations with annual MB of 0.06 for 2018 and 2019.

While the evaluation with AERONET AOD aimed to validate the model’s predictions in column-load, the evaluation of the model’s performance on surface over desert dust source regions in the NAME region is considered necessary to derive trust-worthy products targeted to the aviation sector.

### 3.2 Methodology scheme

The methodology applied for the model evaluation and the assessment of the SDS impacts on aviation, prior to the proposal of the final product, is presented in a schematic diagram in Figure 3.2. The inputs and outputs of every task group are marked in separate sections. A more detailed description of the specific methods employed in each task group is given in Chapters 4 and 5.

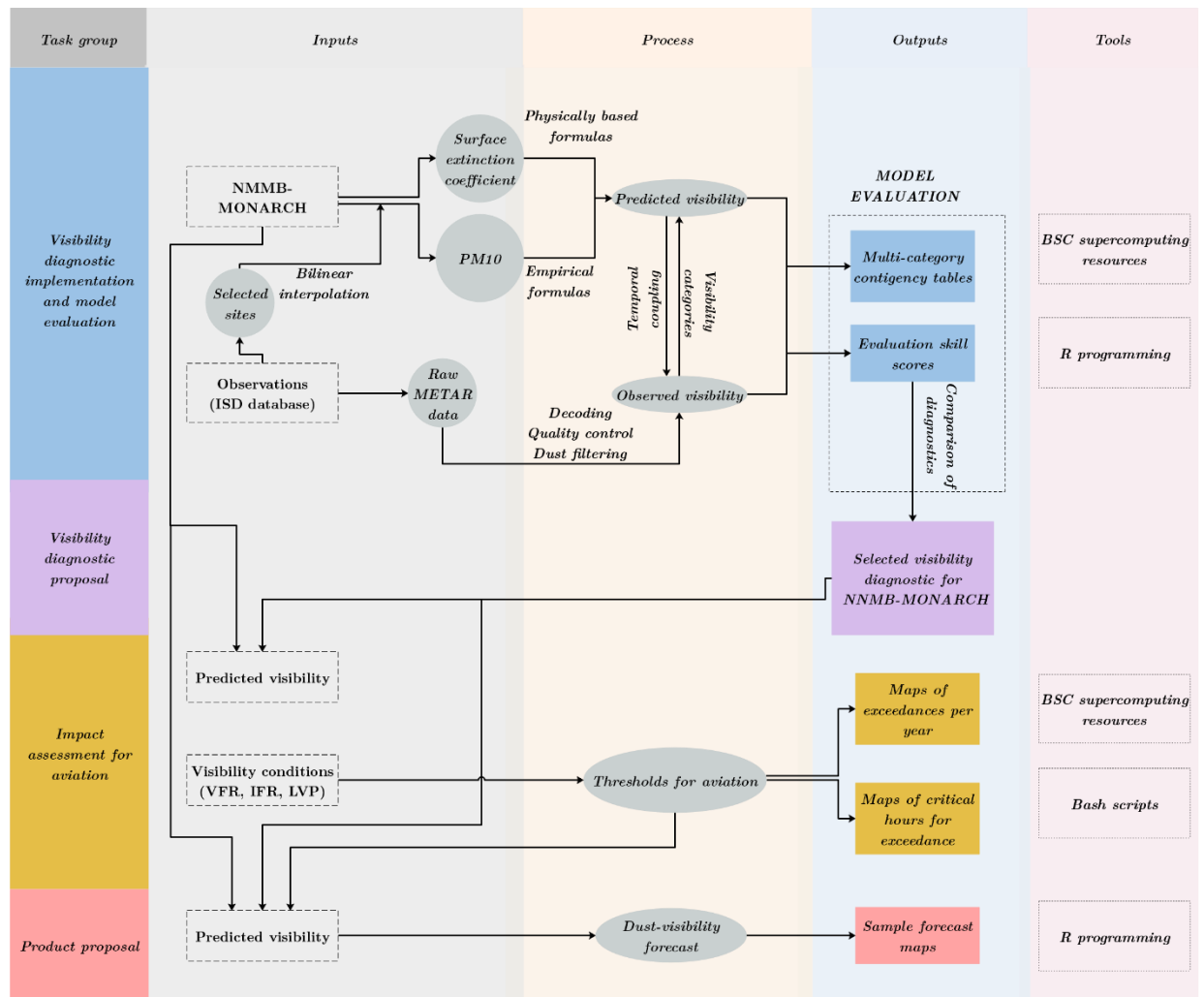


Figure 3.2: Schematic diagram of the methodology applied in the different task groups that form the project.

## 4 Implementation of visibility in dust forecasts

This chapter describes the different approaches that have been used to diagnose visibility from the NMMB-MONARCH model output and the selection of a diagnostic that can be used for operational purposes. Furthermore, it presents the visibility observations considered, the quality control and dust-filtering that has been applied prior to the evaluation, and the obtained model evaluation results.

### 4.1 Visibility approaches

Visibility is a measure of the integrated surface concentration of aerosols and other particles between the eye and distant objects, and can be converted to a surface extinction value, representing the aerosol extinction of light when a viewer is looking horizontally at the surface, through the Koschmieder's formula (Godish, 1997). In desert dust regions, the horizontal visibility is strongly influenced by the dust particle size distribution (Tegen, 2003), and has a clear dependence on the ambient humidity (Shao and Dong, 2006; Cabello *et al.*, 2012). However, many studies have shown that horizontal visibility is a good indicator of SDS (Mahowald *et al.*, 2007; Klose *et al.*, 2010). Several empirical equations relating surface dust concentration and visibility have been proposed in dust regions, such as North America (Chepil and Woodruff, 1957; Patterson and Gillette, 1977), Australia (Tews, 1996; Leys *et al.*, 2002), Asia (Shao and Wang, 2003; Wang *et al.*, 2008; Jugder *et al.*, 2014), West Asia (Dayan *et al.*, 2008) and West Africa (D'Almeida, 1986; Ben Mohamed *et al.*, 1992; Camino *et al.*, 2015).

In the present work different approaches are tested, corresponding both to physically based and empirical parametrisations. In the case of physically based formulas, the selection is limited to the traditionally used Koschmieder equation and its variations. On the other hand, since a great variety of empirical equations is available, only formulas developed and calibrated within the studied domain, i.e North Africa and the Middle East, have been considered. Hence, the five tested approaches to diagnose visibility from the available NMMB-MONARCH model outputs are presented in Table 4.1.

Table 4.1: Tested physically based and empirical equations to estimate visibility.  $PM_{10}$  stands for particulate matter with diameter less than  $10\mu\text{m}$ ,  $V$  for horizontal visibility and  $ec$  for the extinction coefficient in the visible range (at  $550\text{nm}$ ).

Equation	Name	Type	Comments	Reference
$V = \frac{3.92}{ec}$	Koschmieder	Theoretical	Proposes that visibility is inversely proportional to the extinction coefficient. Considers the contrast between a dark object set against the horizon and a constant contrast threshold identifiable by an observer equal to 0.02. It is more appropriate for estimations during daytime.	Godish (1997)
$V = \frac{3.00}{ec}$	Biral	Theoretical	Variation of Koschmieder's equation that considers a contrast threshold of 0.05, resulting in a conversion factor of 3.00 which is also used in practice for the calculation of Meteorological Optical Range (MOR).	Bennett (2012)
$PM_{10} = 1772.24 \cdot V^{-1.1}$	IZO	Empirical	Derived from observations performed during the period 2003-2010 at the Izaña Atmospheric Observatory in <b>Tenerife, Spain</b> .	Camino <i>et al.</i> (2015)
$PM_{10} = 914.0 \cdot V^{-0.73} + 19.03$	DA	Empirical	Calibrated with observations of $PM_{10}$ obtained during a field campaign in <b>Niger</b> from January 1981 to December 1982, with visibility ranges from 0.2 to 40 km.	D'Almeida, 1986
$PM_{10} = -505 \ln V + 2264$	Dayan	Empirical	$PM_{10}$ monitoring site located at Negev Desert. Visibility ranges from 1 to 5 km at Hazerim airport ( <b>Israel</b> ).	Dayan et al. (2008)

## 4.2 Visibility evaluation: Methodology

Following the parametrisations presented in Table 4.1, the surface extinction coefficient at 550nm ( $ec$ ) and dust PM10 surface concentration obtained by the model are converted to horizontal visibility ( $V$ ). The visibility diagnostics obtained are directly comparable to visibility observations from meteorological reports. The proposed evaluation method facilitates the forecast verification in areas where observations from air quality networks are scarce and therefore, suggests an alternative to the traditional forecast verification methods, that use mainly PM10 mass concentration or AOD measurements. This alternative is particularly useful for the NAME region due to the scarcity of observational networks. Since visibility observations consider all aerosols present in the atmosphere, the application of a filter to identify dust-dominant situations is essential. Additionally, the application of an extensive quality control is necessary prior to their comparison with the visibility diagnostics to obtain reliable evaluation results.

Horizontal visibility and meteorological data were obtained from the Integrated Surface Database of the National Climatic Data Center (Smith, Lott and Vose, 2011). The Integrated Surface Database (ISD) consists of global hourly and synoptic observations from over 35,000 stations worldwide, with some having data as far back as 1901, though the data show a substantial increase in volume in the 1940s and again in the early 1970s. ISD currently includes over 14,000 “active” stations worldwide and offers numerous parameters, among them, the parameters required to conduct the present evaluation such as, visibility. ISD visibility observations are obtained from meteorological aerodrome reports (METAR) and from surface synoptic observations (SYNOP), therefore are available in codified format, their temporal resolution is hourly, and their spatial distribution corresponds to that of commercial service airports. Decoding of the raw observations is necessary to obtain the information required for the evaluation.

An example of the raw format of the observations from the Al Maktoum International Airport - OMDW in Dubai, UAE for the 3<sup>rd</sup> of January 2018 at 03:00, is shown in Figure 4.1.





points that coincide with the selected stations, through bilinear interpolation. Additionally, the temporal coupling has been based on the model's time resolution and therefore, observations corresponding to the 3-hourly model timesteps have been selected.

Since the ISD dataset compiles surface data from various sources, for the cases of multiple observations corresponding to the same timestep, the selection of the value to be used in the model evaluation consisted in considering the lowest visibility value available. Although the conversion of predictions per grid cell to point values that correspond to observation points is a common technique in model evaluation, the case of evaluation with visibility observations presents some particularities that mainly arise from the nature of the visibility observation database.

Visibility is a complex physico-chemical phenomenon, governed mainly by the atmospheric extinction coefficient associated with solid and liquid particles held in suspension in the atmosphere. The extinction is caused primarily by light scattering. Its estimation is subject to variations in individual perception and interpretative ability, as well as the light source characteristics and the transmission factor. Thus, any visual estimate of visibility is subjective.

Visibility estimation by human observers depends not only on the photometric and dimensional characteristics of the object to be perceived, but also on the observer's contrast threshold. At night, the intensity of the light sources, the background illuminance and, the adaptation of the observer's eyes to darkness affect visibility measurements and therefore, the estimation of visibility at night is particularly problematic. In most of the airports in the study region, horizontal visibility is estimated by a human observer using targets located in different directions.

Apart from the spatial and temporal coupling of model and observations, it is crucial to complement the use of visibility data with weather information to discard cases of reduced visibility due to the presence of hydrometeors and other aerosols. This filtering can be done considering either the present weather codes, included in the raw data or relative humidity thresholds. It is highlighted that present weather information is a quality characterisation that depends on human observer and not on automated measurements. Therefore, it forms part of the additional section of the raw ISD data and is not available for all decoded observations. The analysis of the decoded data revealed that 32 stations do not provide information on present weather for 2018 and 25 stations for 2019 systematically, while those that provide present insufficient density of information. Hence, the present weather codes in the ISD dataset are not an appropriate filter and relative humidity (RH) has been chosen as the main filter applied to identify observations related to the presence of dust.

Considering that the analysis is limited to desert dust regions in North Africa and the Middle East, desert dust is the main contributor to the aerosol budget (Basart *et al.*, 2009). For the comparison with the model output, that only considers desert dust, visibility observations accompanied by RH values greater than 70% are discarded, since desert dust air masses are related to dry conditions. RH is calculated from the air temperature ( $T$ ) and dew point temperature ( $T_d$ ) measurements included in the raw ISD dataset, using the approximation described by the Equation 1 (Lawrence, 2005).

*Equation 1: Formula for relative humidity estimation from air temperature and dew point temperature.*

$$RH = 100 \cdot \frac{\exp\left(\frac{17.625 \cdot T_d}{243.04 + T_d}\right)}{\exp\left(\frac{17.625 \cdot T}{243.04 + T}\right)}$$

In stations located in source regions, where desert dust is the dominating aerosols species, the reduction of observations after the application of the RH filter is not significant, i.e. data provided by stations located in Algeria have experienced a reduction of less than 5%. On the contrary, a significant reduction of data (up to 70%) is observed in stations located in long-range transport and coastal regions. More specifically, in Larnaca International Airport (LCLK) in Cyprus the RH filter has removed 35.5% of the initial data for 2018 and 36.4% for 2019, while in Tenerife Norte Airport (GCXO) in Canary Islands, a tremendous reduction of 66.9% has been observed for 2018 and 58.6% for 2019, which is explained by local meteorology and more specifically by the quasi-permanent thermal inversion above the island that holds down the humid oceanic air masses, resulting in high humidity conditions. In Léopold Sédar Senghor International Airport (GOOY) in coastal Senegal, 66.9% of the observations have been removed for 2018, while in Tambacounda Airport (GOTT) in continental Senegal, the removal percentage for 2018 was 20.7%.

In all cases, it becomes evident that dust-filtering visibility observations with RH is essential to remove cases of low visibility due to other aerosols or the presence of hydrometeors and to obtain an homogeneous dataset of dust observations that is comparable to the dust predictions provided by the model and that leads to reliable model evaluation results. A complete list of the percentage of data reduction after the application of the RH filter is given in Appendix B.

While the model outputs are continuous values, visibility observations are found to be categorical, as it is shown in the time series of three airports in United Arabic Emirates (UAE, Figure 4.3), Burkina Faso (Figure 4.4) and Algeria (Figure 4.5). This is mainly due to the methods used to conduct the visibility measurements, which are performed either automatically with the use of visibility



sensors, or manually by trained staff using visual reference indicators. Strongest visibility reductions in the observations are associated to the desert dust cycle with maximum reductions in winter in Sahel (see Burkina Faso in Figure 4.4), in spring-summer in Sahara (see Algeria in Figure 4.5) and in spring in the Middle East (see UAE in Figure 4.3).

The analysis of the time series of the observations shows specific visibility categories. The most frequent categories are 20km, 15km, 10km, 8km and 6km, while for visibilities lower than 5km there are more categories that go to the resolution of meters (Figure 4.3, Figure 4.4, Figure 4.5). For evaluation purposes, visibility values higher than 8 km are considered as “clean” atmosphere. Visibility values below 1km are considered SDS (section 2.3.1), while visibility values below 5km start to present implications for the aviation sector (section 5.1.1). As a result, the thresholds that are considered appropriate for categorical model evaluation with visibility observations in the studied domain are 8km, 5km and 1km. These thresholds mark the visibility categories applied in the evaluation and are defined as it is shown in Table 4.2. It is highlighted that the necessity for categorical evaluation derives from the nature of the visibility observations, which also leads to the necessity for classifying the model outputs in accordance with the defined visibility categories.

*Table 4.2: Definition of visibility categories for categorical forecast evaluation with visibility observations in NAME.*

Visibility category	Range (km)
0	$V \geq 8$
1	$5 \leq V < 8$
2	$1 \leq V < 5$
3	$V < 1$

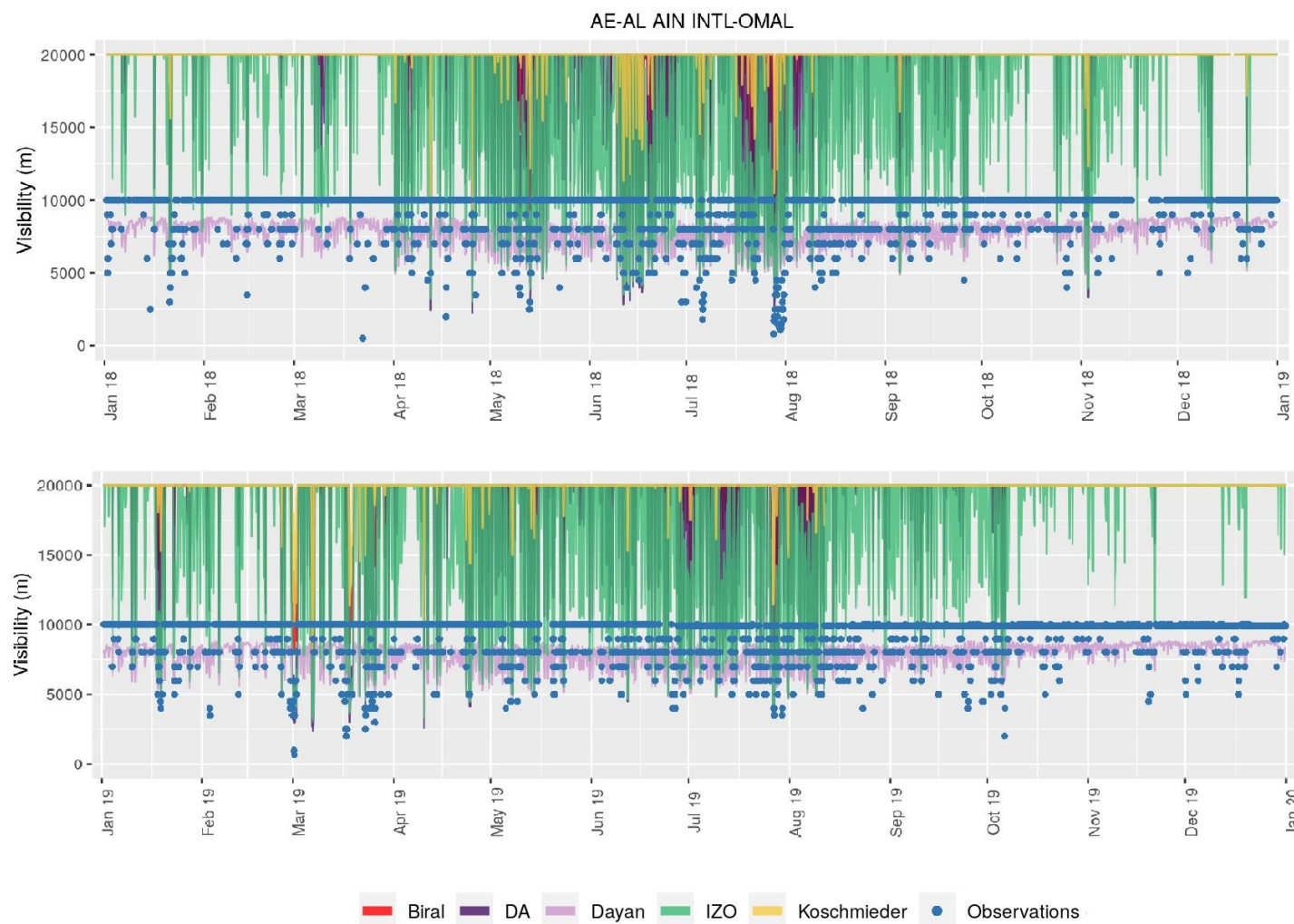


Figure 4.3: Predicted time series for visibility diagnostics, as described in Table 4.1, and observations for the Al Ain International Airport in Abu Dhabi, UAE ( $N24^{\circ}15.70'$ ,  $E55^{\circ}36.55'$ ) for 2018 and 2019 respectively.

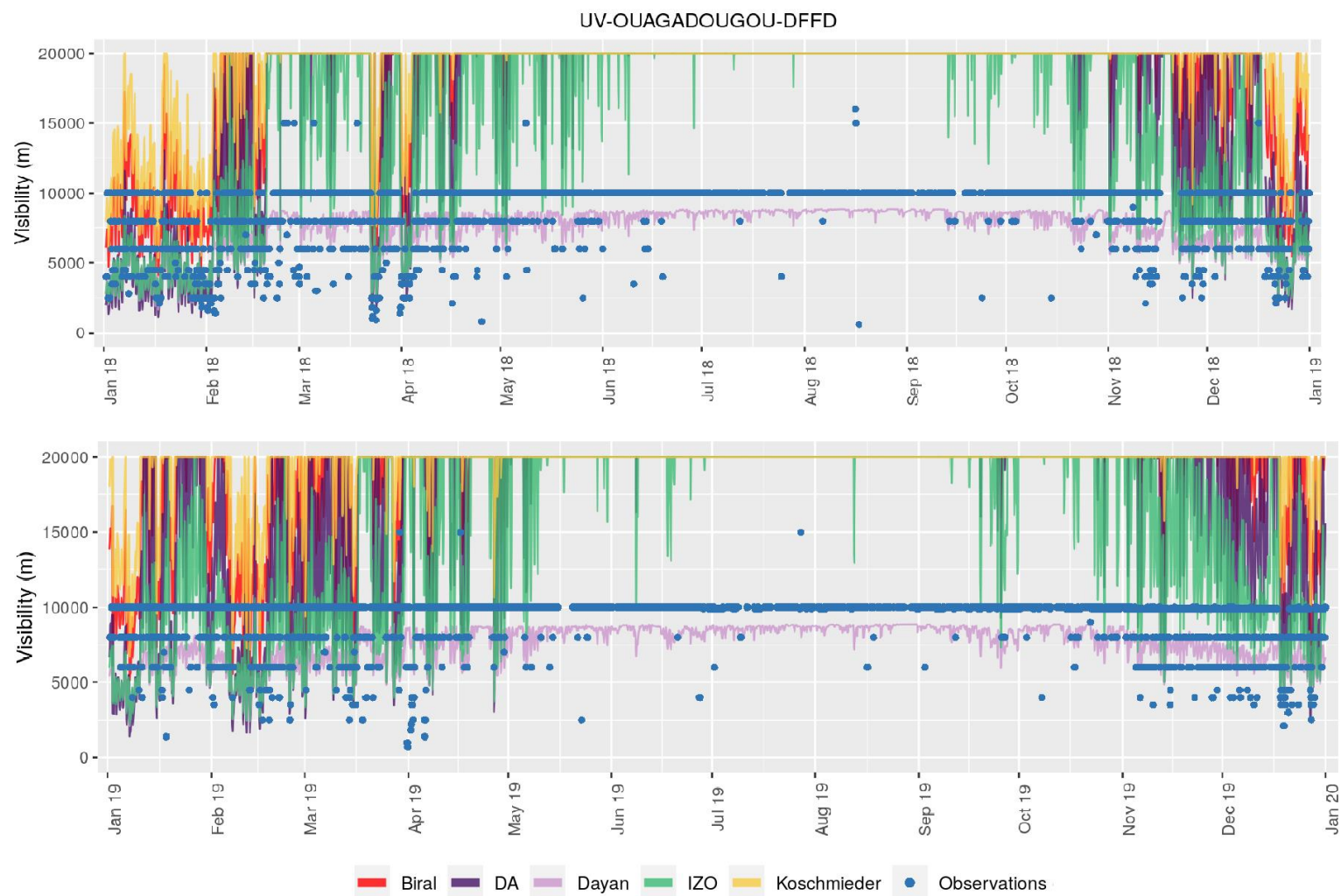


Figure 4.4: Predicted time series for visibility diagnostics, as described in Table 4.1, and observations for the Thomas Sankara International Airport Ouagadougou ( $N12^{\circ}21.22'$ ,  $W1^{\circ}30.72'$ ) in Burkina Faso for 2018 and 2019 respectively.

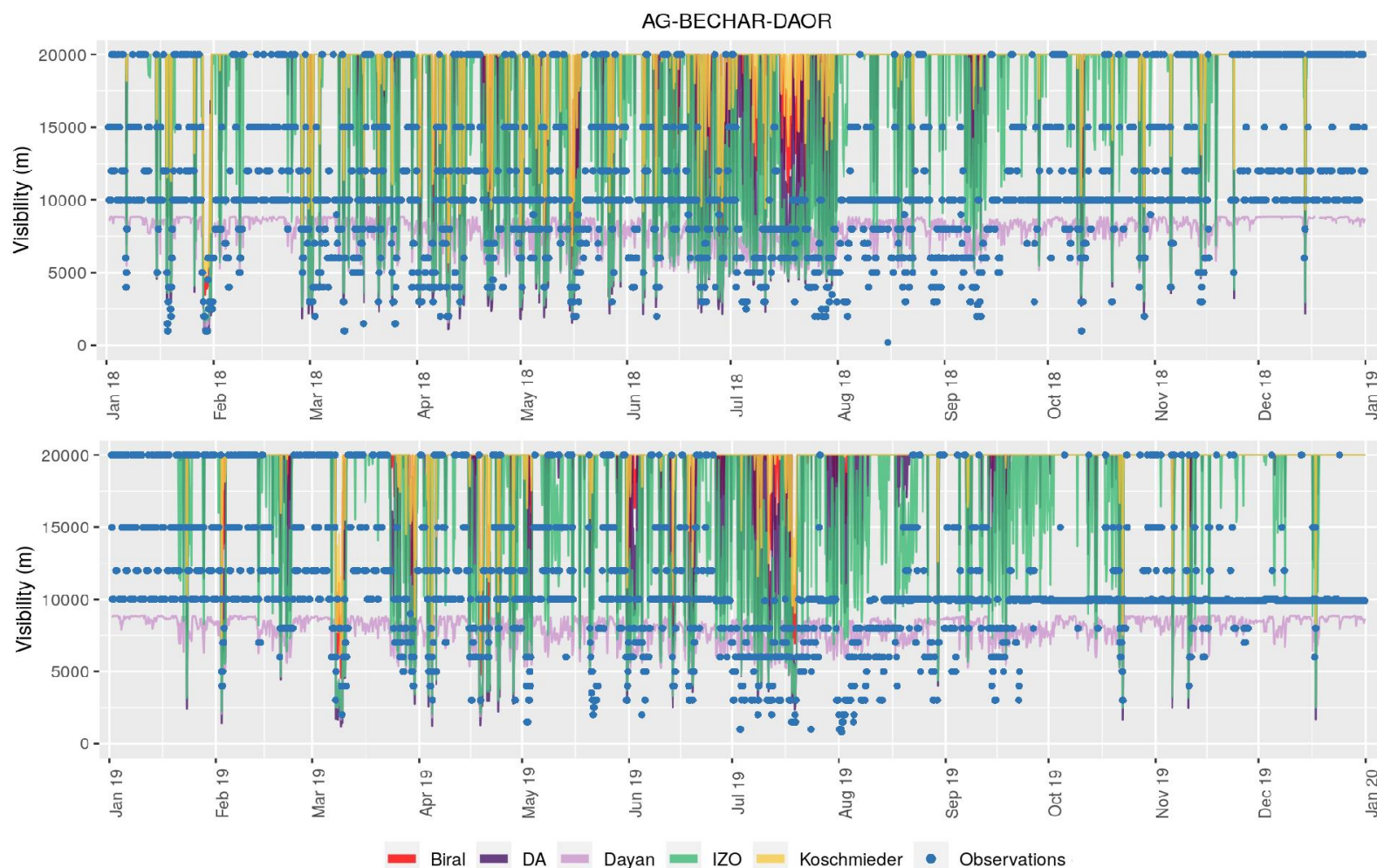


Figure 4.5: Predicted time series for visibility diagnostics, as described in Table 4.1, and observations for the Boudghene Ben Ali Lotfi Airport ( $N31^{\circ}39.16'$ ,  $W2^{\circ}15.40'$ ) in Algeria for 2018 and 2019 respectively



The creation of multi-category contingency tables, based on the defined categories, is a useful means to better understand and present the model's performance. Multi-category contingency tables consist of the values  $n(F_i, O_j)$  that denote the number of forecasts in category  $i$  that had observations in category  $j$ . Elements along the diagonal represent the model **hits**, i.e. the frequency of accurate category predictions, while off-diagonal elements give information about the specific nature of the forecast errors (Table 4.3). More specifically, elements above the diagonal represent overestimated category predictions, considered **false alarms**, while elements below the diagonal represent underestimated category predictions, interpreted as **misses**.

Table 4.3: Example of multi-category contingency table.

Category	1	2	...	i	
1	$n(F_1, O_1)$	$n(F_1, O_2)$	...	$n(F_i, O_1)$	False alarms
2	$n(F_2, O_1)$	$n(F_2, O_2)$	...	$n(F_i, O_2)$	
...	...	...	...	...	
j	$n(F_1, O_j)$	$n(F_2, O_j)$	...	$n(F_i, O_j)$	
	Misses				Hits

In order to evaluate the performance of the different visibility diagnostics, a set of statistics based on the calculated contingency tables are used. These include the Accuracy, Heidke Skill Score (HSS), Bias score, Hit rate and False alarm rate, furtherly explained in Table 4.4.



Table 4.4: Statistics used for the evaluation of categorical forecasts.

Name	Formula	Range	Perfect score	Explanation
Accuracy	$\frac{1}{N} \sum_{i=1}^k n(F_i, O_i)$	$[0, 1]$	1	Indicates what fraction of the total forecasts were in the correct category. It is heavily influenced by the most common category. The $n(F_i, O_j)$ factor denotes the number of forecasts and observations along the diagonal, while $N$ is the total number of forecasts.
Heidke skill score	$\frac{\frac{1}{N} \sum_{i=1}^k n(F_i, O_i) - \frac{1}{N} \sum_{i=1}^k N(F_i)N(O_i)}{1 - \frac{1}{N^2} \sum_{i=1}^k N(F_i)N(O_i)}$	$(-\infty, 1]$	1	Measures the accuracy of the forecast in predicting the correct category, relative to that of random chance. Negative values indicate that the chance forecast is better, while 0 means no skill.
Bias score	$\frac{hits + false\ alarms}{hits + misses}$	$[0, \infty)$	1	Measures the ratio of the frequency of forecasted categories to the frequency of observed categories. Indicates whether the forecast tends to underestimate (bias<1) or overestimate (bias>1) categories.
Hit rate	$\frac{hits}{hits + misses}$	$[0, 1]$	1	Measures what fraction of the observed categories was correctly forecasted. It considers the hits, but ignores the misses, hence it should be used in conjunction with the false alarm ratio.
False alarm ratio	$\frac{false\ alarms}{hits + false\ alarms}$	$[0, 1]$	0	Measures what fraction of the predicted categories did not occur. It considers the false alarms, but ignores the hits, hence it should be used in conjunction with the hit rate.

### 4.3 Evaluation results

The model evaluation results obtained for 2018 and 2019 through the five visibility diagnostics are presented as multi-category contingency tables (Figure 4.6 and Figure 4.7) and categorical skill scores (Table 4.5 and Table 4.6).

#### 4.3.1 Multi-category contingency tables

The evaluation results for 2018 and 2019 are presented in Figures 4.6 and 4.7 respectively, as multi-category contingency tables for the whole studied domain. According to the **observed visibility categories**, category 0 has been the most frequently occurred in the whole domain during 2018 (81.72%), followed by category 1 (12.65%), category 2 (5.33%) and finally category 3 with only 0.30% of frequency. The distribution of the observations is similar in 2019. Category 0 has a bit higher frequency of occurrence (81.16%) compared to the previous year, followed again by category 1 (10.39%), category 2 (3.31%) and category 3 (0.14%). Since the frequency of observations is particularly low for categories 2 and 3, the evaluation of the diagnostics' performance in predicting these categories, might result challenging.

Concerning the performance of the model, the **DA diagnostic** for 2018 (Figure 4.6a) has an overall number of hits of 79.7%. It has a strong tendency in predicting category 0 (92.27%) and its predictions are accurate in 77.7% of the cases. It significantly underpredicts category 1 (12.65% of observed cases versus 3.5% of predicted cases, with only 0.71% accuracy), and although it proves to be able to predict visibility values below 1km (0.16%), its accuracy in predicting category 3 is extremely low (0.04%). The DA diagnostic overforecasts visibility categories in 5.1% of the cases and underpredicts with frequency 15.2%. Its performance in 2019 (Figure 4.7a) follows the same pattern, although with higher overall accuracy (83% of hits), mainly attributed to the greater number of observations in category 0, combined to the diagnostic's "preference" towards this category. Similarly to the previous year, the DA diagnostic overforecasts in 5.7% of the cases and underpredicts with frequency 11.3%.

The **Dayan diagnostic** achieves accurate predictions in 57.3% of the cases for 2018 (Figure 4.6b). It strongly overestimates category 1 (29.23%), which is related to the upper limit (approximately 8km) of this parametrisation (see Table 4.1). Although, it can predict the category 3, the predicted values are not in accordance with the observed ones (0.30% of observed cases versus 0.08% of predicted cases with only 0.02% accuracy). It has a strong tendency to overforecast (32.3%), while it underestimates 10.4% of the times. Its performance for 2019 (Figure 4.7b) is similar to that of the previous year. Its overall accuracy is higher (57.6%), combined with an equally high tendency for overestimation (34.6%) and lower underestimation rate (7.8%).

The **IZO diagnostic** (Figure 4.6c) achieves overall accurate categorical predictions in 78.1% of the cases for 2018. Almost 90% of its predictions are found in category 0 and the majority of them are accurate (75.49%). It overforecasts 7.24% of the times and underpredicts 14.7% of the times. It strongly underpredicts category 1 (12.65% of observed cases versus 6.5% of predicted cases, with only 1.22% accuracy), presents similar observed and predicted frequencies for category 2 (5.33% of observed cases versus 4.21% of predicted cases) and it proves to be unable to predict category 3. For 2019 (Figure 4.7c), the overall accuracy of its predictions is improved (81%), the frequency of overestimation is slightly higher (8.1%) and underestimation is lower (10.95%).

The **Koschmieder diagnostic** (Figure 4.6d) gives accurate category predictions in 81.8% of the cases for 2018. However, it is not able to predict visibility values below 1km (that correspond to category 3), which explains the zero frequencies in the last column of the contingency table. Most of its predictions (99.17%) are found in category 0, from which 81.59% are accurate. Its tendency to overestimate is particularly low (0.15%), which is a great advantage, whereas its tendency to underestimate is significant (18%). The performance of the Koschmieder diagnostic in 2019 (Figure 4.7d) follows the same pattern as in 2018, with greater overall accuracy (86.2%), low frequency of overforecasting (0.22%) and significant frequency of underestimation (13.56%).

The **Biral diagnostic** (Figure 4.6e) predicts accurately the observed category with a frequency of 81.8%, its predictions for category 0 are accurate in 81.25% of the cases for 2018, while its accuracy in predicting categories 1 and 2 is slightly higher compared to the Koschmieder diagnostic. The fact that the two equations only present a small difference in the applied conversion factor, as it is shown in Table 4.1 explains the fact that neither the Biral diagnostic is able to provide predictions in category 3, resulting in zero frequencies in the last column of the corresponding contingency table. Its tendency to overestimate is low (0.54%), but the underestimation frequency is significant (17.6%), mainly located in categories 1 and 2. For 2019 (Figure 4.7e), the Biral diagnostic presents higher overall accuracy (86.1%), slightly higher, but still low frequency of overestimation (0.71%) and lower frequency of underprediction (13.2%) compared to the previous year. Again, its tendency to underestimate is mainly located in categories 1 and 2, while it has no skill in predicting category 3.

Underpredictions derived from the physically based diagnostics (Koschmieder and Biral) can be partly linked to the fact that visibility observations consider all ranges of particle size, while the NMMB-MONARCH model only takes into account particles up to 10  $\mu\text{m}$ . On the other hand, the use of empirical diagnostics (IZO, DA, Dayan) designed to correlate visibility with PM10 can compensate the difference in the mass of coarse particles that is not considered by the model.

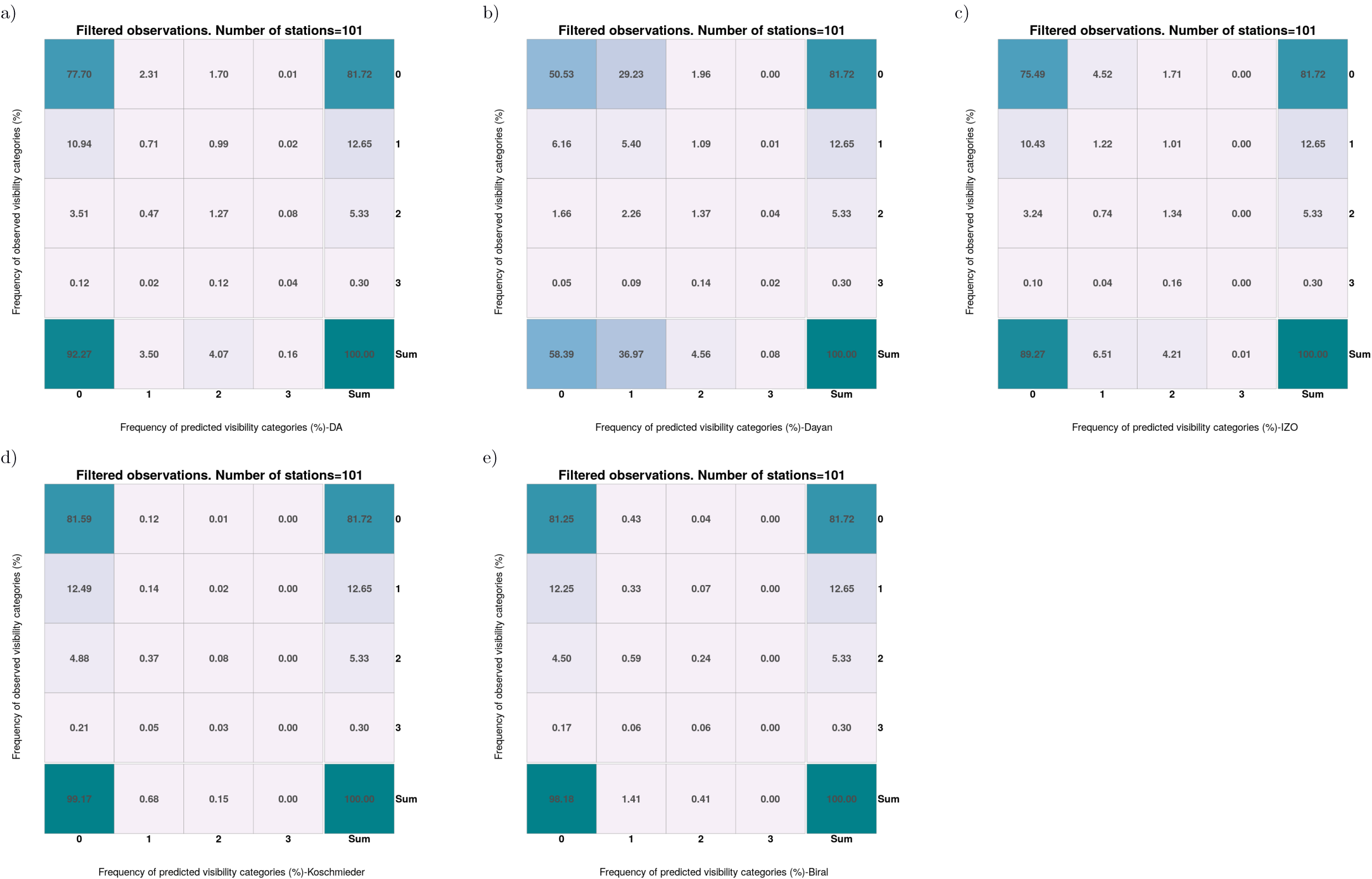


Figure 4.6: Multi-category contingency tables depicting the frequency of predictions and observations in each category in the studied area for 2018: a) DA, b) Dayan , c) IZO, d) Koschmieder, e) Biral.

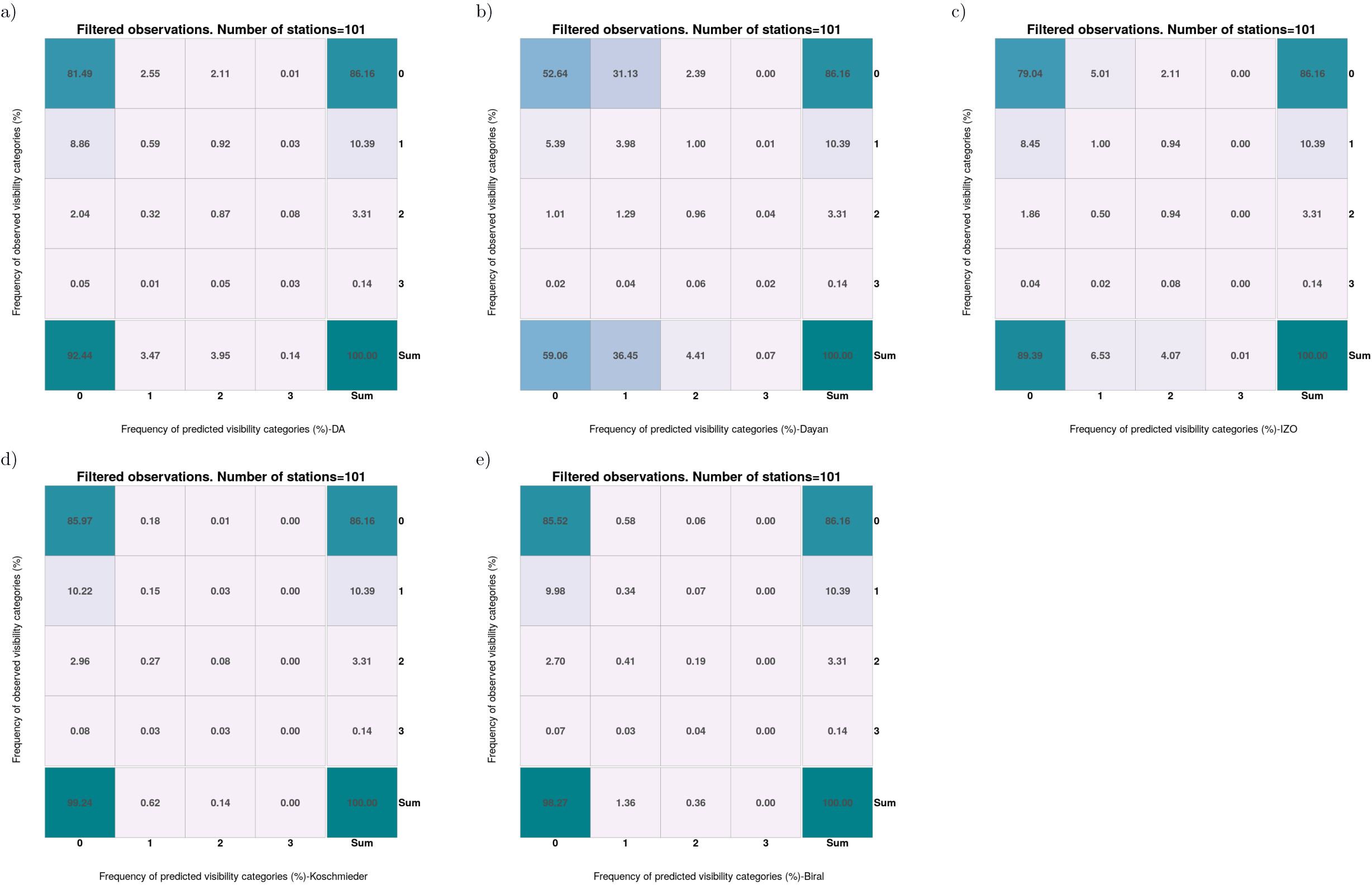


Figure 4.7: Multi-category contingency tables depicting the frequency of predictions and observations in each category in the studied area for 2019: a) DA, b) Dayan , c) IZO, d) Koschmieder, e) Biral.

### 4.3.2 Overall results: Skill scores

As it has been explained in section 4.2, there are two sets of skill scores that can be calculated for the multi-category evaluation of the visibility predictions. The first corresponds to the overall skill of the diagnostics in predicting accurately the observed visibility categories and it is expressed through Accuracy and the Heidke skill score. The second refers to the specific skill of the diagnostics in predicting each one of the 4 respective visibility categories and it is expressed through Bias Score, Hit rate and False alarm ratio per category. Table 4.5 presents the overall accuracy and the Heidke skill score for the five tested visibility diagnostics for 2018 and 2019.

*Table 4.5: Overall skill scores for evaluation for the five tested visibility diagnostics (described in Table 4.1) for 2018 and 2019.*

Diagnostic	2018		2019	
	Accuracy	Heidke skill score	Accuracy	Heidke skill score
DA	0.80	0.15	0.83	0.14
Dayan	0.57	0.10	0.58	0.06
IZO	0.78	0.16	0.81	0.14
Koschmieder	0.82	0.04	0.86	0.04
Biral	0.82	0.07	0.86	0.08

As it is observed in Table 4.5, for 2018 the accuracy of the five diagnostics range from 0.57 to 0.82 in a scale from 0 to 1, with 1 corresponding to 100% of forecasts in the correct category. The Dayan diagnostic presents overall lower accuracy than the others, while the remaining four present similar skill in predicting accurately the visibility categories, with the diagnostics derived from physically based equations (Koschmieder and Biral) having the best accuracy. Nevertheless, the same diagnostics present Heidke skill scores slightly above zero, while diagnostics derived from empirical equations have better skill. For 2019, the performance of the five diagnostics is similar to that of the previous year, although all scores are a bit higher. Now the accuracy of the five diagnostics range from 0.58 to 0.88, with Koschmieder and Biral being again the most accurate, besides their Heidke skill score, which is slightly above zero. Similarly, the Dayan diagnostic presents low Heidke skill score, in addition to low accuracy for 2019 and in general, it proves to be the weakest diagnostic of all. Overall, while the IZO and the DA diagnostics present high Heidke skill scores, Koschmieder and Biral prove to be more skillful in correctly predicting the visibility categories.

To better understand the skill of the five diagnostics in categorical predictions, a closer look to their performance per category is necessary. Table 4.6 presents the



Bias Score, Hit rate and False alarm ratio per category for the five tested diagnostics, for 2018 and 2019. The results by category show that:

**Category 0** ( $V \geq 8\text{km}$ ), is systematically overpredicted by all diagnostics (bias score above 1), except Dayan. The IZO diagnostic has the lowest overestimation tendency (1.09 in 2018, 1.04 in 2019), high hit rate (0.92 for both 2018 and 2019) and low false alarm ratios (0.15 in 2018, 0.12 in 2019). The DA has similar scores to IZO. The Koschmieder and Biral diagnostics have perfect hit rate (1.00 and 0.99 respectively) accompanied by very good false alarm ratios (0.18 and 0.17 for 2018, 0.13 for both in 2019).

**Category 1** ( $5\text{km} \leq V < 8\text{km}$ ) is strongly overpredicted from the Dayan diagnostic (bias score 2.92 in 2018, 3.51 in 2019), with medium-low hit rate (0.43 for 2018 and 0.38 for 2019) and high false alarm ratio (0.85 for 2018 and 0.89 for 2019). Additionally, it is slightly underpredicted by the DA and IZO diagnostics (bias score 0.28 and 0.51 for 2018 and 0.63 for both for 2019), with very low hit rates and high false alarm ratios, while it is strongly underpredicted by the Koschmieder and Biral diagnostics (bias scores close to zero).

**Category 2** ( $1\text{km} \leq V < 5\text{km}$ ) is systematically underpredicted by the physically based diagnostics (bias scores close to zero), suggesting they have almost no skill in predicting such visibility range. On the other hand, the 3 empirical diagnostics slightly underforecast this category in 2018, and slightly overforecast it in 2019. This inconsistency between the two years might be attributed to the higher observed frequency of visibility values belonging in category 2 in 2018 and highlights the weakness of the 3 empirical diagnostics in predicting this category. Additionally, all diagnostics present low hit rates and significant false alarm ratios.

**Category 3** ( $V < 1\text{km}$ ) is highly underforecasted from the DA and the Dayan diagnostics (bias score below 1), with very low hit rates and high false alarm ratios. The Koschmieder and Biral have no skill in predicting such visibility values (bias score close to, or equal to zero), which also explains the zero hit rate and the undetermined false alarm ratio.

Table 4.6: Overall skill scores by categories for the five tested visibility diagnostics (described in Table 4.1) for 2018 and 2019.

Diagnostic	Category 0 $V \geq 8\text{km}$			Category 1 $5\text{km} \leq V < 8\text{km}$			Category 2 $1\text{km} \leq V < 5\text{km}$			Category 3 $V < 1\text{km}$		
	Bias score	Hit rate	False alarm ratio	Bias score	Hit rate	False alarm ratio	Bias score	Hit rate	False alarm ratio	Bias score	Hit rate	False alarm ratio
2018												
DA	1.13	0.95	0.16	0.28	0.06	0.80	0.76	0.24	0.69	0.52	0.13	0.75
Dayan	0.71	0.62	0.13	2.92	0.43	0.85	0.86	0.26	0.70	0.27	0.07	0.73
IZO	1.09	0.92	0.15	0.51	0.10	0.81	0.79	0.25	0.68	0.02	0.01	0.53
Koschmieder	1.21	1.00	0.18	0.05	0.01	0.79	0.03	0.01	0.47	0.00	0.00	-
Biral	1.20	0.99	0.17	0.11	0.03	0.76	0.08	0.04	0.43	0.00	0.00	-
2019												
DA	1.07	0.95	0.12	0.63	0.06	0.83	1.19	0.26	0.78	1.01	0.19	0.81
Dayan	0.69	0.61	0.11	3.51	0.38	0.89	1.33	0.29	0.78	0.52	0.13	0.75
IZO	1.04	0.92	0.12	0.63	0.10	0.85	1.23	0.29	0.77	0.06	0.03	0.52
Koschmieder	1.15	1.00	0.13	0.06	0.01	0.76	0.04	0.02	0.45	0.00	0.00	-
Biral	1.14	0.99	0.13	0.13	0.03	0.75	0.11	0.06	0.48	0.00	0.00	-

The performance of the visibility diagnostics presents variations for the different areas included in the studied domain. The corresponding accuracies for three selected countries, representative of the main sub-regions included in the studied domain, Burkina Faso (Sahel), UAE (Middle East) and Algeria (Northern Africa) are presented in Table 4.7. As it can be observed, the physically based diagnostics (Koschmieder and Biral) tend to provide more accurate predictions in source regions (0.81 in Burkina Faso and Algeria for 2018 and 0.86 and 0.87 for 2019) than in the Middle East (0.71 in 2018, 0.78 in 2019). It is also highlighted that the IZO diagnostic presents the lowest variation in its accuracy among the different sub-regions (accuracy ranging from 0.71 to 0.78 for 2018 and from 0.77 to 0.80 for 2019), resulting in homogeneously accurate predictions for the different sub-regions and suggesting that it is a robust diagnostic for the whole domain.

*Table 4.7: Accuracy of visibility diagnostics for four selected countries: Burkina Faso (Sahel), UAE (Middle East), and Algeria (Northern Africa), for 2018 and 2019.*

Country	Accuracy	
	2018	2019
<b>DA</b>		
UAE	0.71	0.78
Burkina Faso	0.81	0.81
Algeria	0.77	0.82
<b>Dayan</b>		
UAE	0.54	0.59
Burkina Faso	0.57	0.52
Algeria	0.46	0.47
<b>IZO</b>		
UAE	0.71	0.78
Burkina Faso	0.78	0.77
Algeria	0.75	0.80
<b>Koschmieder</b>		
UAE	0.71	0.78
Burkina Faso	0.81	0.87
Algeria	0.81	0.87
<b>Biral</b>		
UAE	0.71	0.78
Burkina Faso	0.81	0.86
Algeria	0.81	0.86

#### 4.4 Visibility diagnostic

Overall, all visibility diagnostics have presented similar values of accuracy, ranging from 0.78 to 0.82 in 2018 and from 0.81 to 0.86 in 2019, except for the Dayan diagnostic that systematically presents much lower accuracy to its predictions (0.57 in 2018 and 0.58 in 2019). The lower accuracy combined to the systematically high frequency of overestimation, as it has been commented in section 4.3.1 demonstrates that the Dayan equation is not an appropriate visibility diagnostic for the studied domain. Concerning the remaining empirical diagnostics, IZO and DA, their performance is quite similar: they provide highly accurate predictions (with accuracies of 0.80 and 0.83 for DA in 2018 and 2019; 0.78 and 0.81 for IZO) for the whole domain and they underestimate with similar frequencies. While the DA diagnostic presents lower frequencies of overestimation, the IZO diagnostic proves to be more homogeneously accurate in its predictions for different sub-regions and therefore, it is selected as the reference empirical diagnostic for the studied domain. Concerning the physically based diagnostics, Koschmieder and Biral, they present the highest accuracy in their predictions for the whole domain (with accuracies of 0.82 in 2018 and 0.86 in 2019), particularly in North Africa, and the lowest tendency to overestimate categories, compared to the empirical diagnostics, although they have higher tendency to underestimate the visibility categories.

The IZO, DA and Dayan diagnostics rely on empirical equations created and calibrated in specific locations within the NAME domain, therefore their performance in other regions might be uncertain. Considering that the final visibility diagnostic should be robust and that the NMMB-MONARCH model is multiscale, that means it can be configured from regional to global domains, the use of physically based diagnostics (i.e., Koschmieder and Biral) is preferable. However, their predictions could be improved with appropriate calibration.

Calibration is a procedure based on the comparison of the model to a real system and includes its iterative revision until it leads to acceptable results. In this case, the conducted calibration aims to compensate the errors that derive from the differently defined visibility predictions and observations explained in Section 4.2, to reduce the frequency of underestimation of visibility categories and to improve the hit rates for the most poorly represented categories (categories 1, 2 and 3).

The fact that the Biral diagnostic presents better Hiedke skill score (Table 4.4) and higher accuracy in predicting categories 1 and 2 compared to the Koschmieder diagnostic, provides a hint that the calibration of the physically based diagnostics should center in reducing the applied conversion factor (3.92 in the Koschmieder equation; 3.00 in Biral; Table 4.1). For that reason, three conversion factors have been tested (1.5, 2.0 and 2.5), resulting in the diagnostics Koschmieder15,

Koschmieder20 and Koschmieder25, respectively. Their performance has been assessed for 2018 and 2019 and the obtained results are presented in Figure 4.8. As it can be observed in Figures 4.8a-c for 2018 and 4.8e-g for 2019, the overall accuracy of the diagnostic decreases with the reduction of the applied conversion factor. However, the hit rates for the categories 1 and 2 are improved and in the case of the Koschmieder15 calibration, they are competent to the IZO hit rates per category (Figure 4.8d), although category 3 remains unpredicted. Moreover, the frequency of underestimation of visibility categories drops for lower conversion factors, suggesting that the lowest factor should be chosen, resulting in the calibrated Koschmieder15 diagnostic.

The results of the Koschmieder15 diagnostic (Figures 4.8a and 4.8e) are similar to the IZO diagnostic (Figures 4.8d and 4.8h). More specifically, the Koschmieder15 diagnostic predicts accurately the visibility categories with frequency 79.6% for 2018 and 82.8% for 2019, hence slightly more accurately than IZO; it overestimates with frequency 5.19% and 5.91% and underestimates with frequency 15.2% and 11.28% for 2018 and 2019 respectively. Additionally, in the Middle East, which is the sub-domain where the theoretical diagnostics proved to be weaker, the performance of the calibrated Koschmieder15 is substantially improved (accuracy of 0.77 in UAE for 2018 and 0.84 for 2019).

Considering the requirement of scalability and potential applicability of the forecast in other domains and taking into account the evaluation results, the proposed diagnostic for visibility in the NAME domain is the calibrated Koschmieder diagnostic, with conversion factor 1.5 (i.e. Koschmieder15).

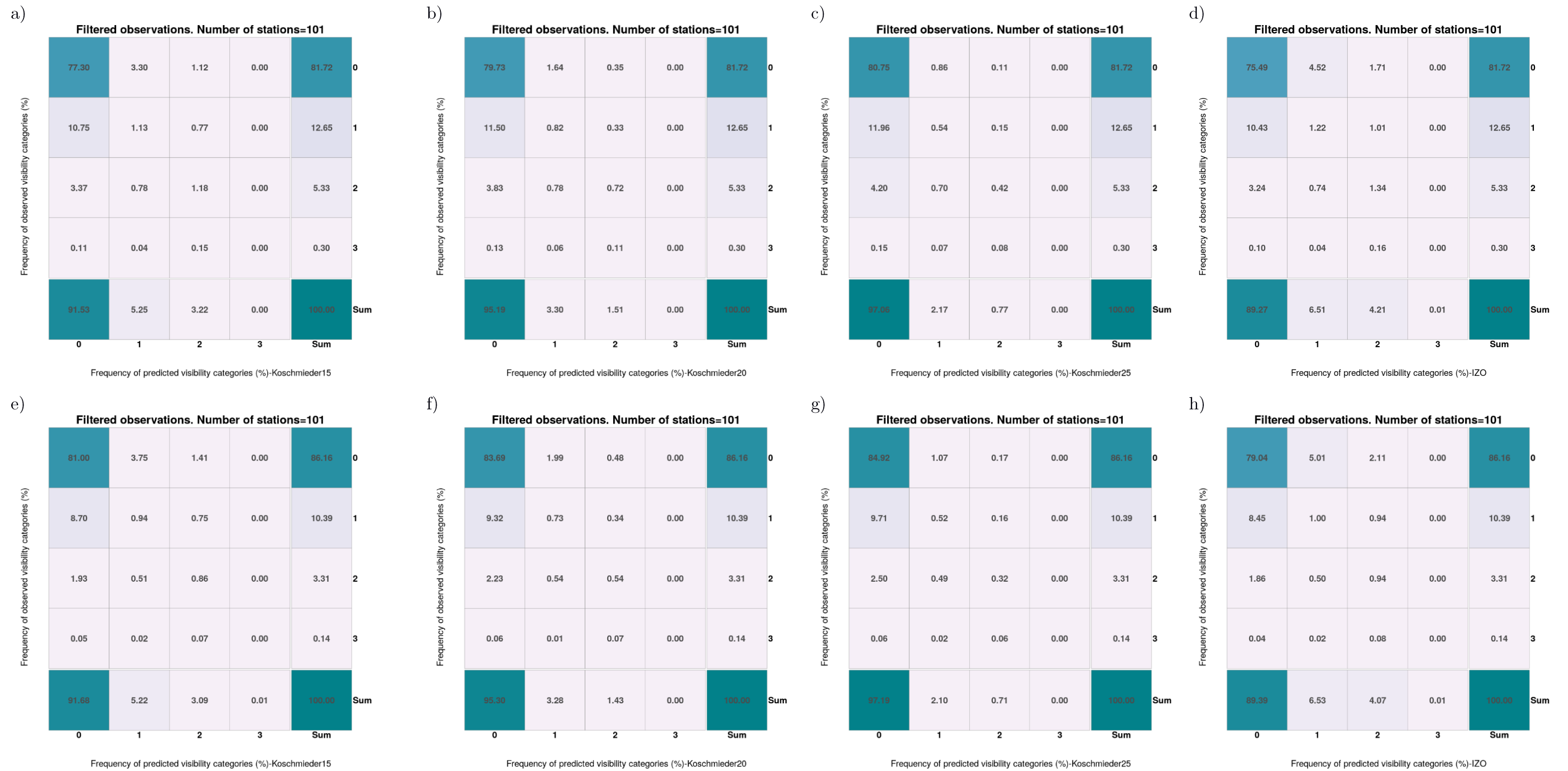


Figure 4.8: Contingency tables depicting the performance of the tested calibrations for the Koschmieder equation versus the performance of the IZO diagnostic. a) Calibration with 1.5 factor- 2018, b) Calibration with 2 factor- 2018, c) Calibration with 2.5 factor-2018, d) IZO diagnostic- 2018, e) Calibration with 1.5 factor- 2019, f) Calibration with 2 factor- 2019, g) Calibration with 2.5 factor-2019, h) IZO diagnostic- 2019



## 5 Impact assessment of SDS: Aviation sector

### 5.1 Methodology

The impact analysis performed relies on the two-dimensional surface extinction coefficient at 550nm predicted by the NMMB-MONARCH model. The conversion to visibility is achieved using the Koschmieder equation, properly calibrated to compensate the systematic errors of the model's predictions, in accordance with the election made in Section 4.4

The visibility values obtained by the conversion are translated into thresholds that correspond to either visual flight rules (VFR), instrument flight rules (IFR) or low visibility procedures (LVP) that regulate air operations and are explained in this section. While VFR and IFR include multiple visibility thresholds marking multiple operation categories, LVP is defined by a singular threshold. Moreover, a binary translation of boundary thresholds for each set of rules is possible and it is adopted for the present impact analysis.

Maps showing the frequency of occurrence of the above-mentioned flight rules and procedures per aggregation period and grid cell are provided as result of the analysis conducted for 2018 and 2019. The visualised frequency maps estimate the number of days in which aviation-related thresholds were exceeded during the assessment period and intend to identify which time of the day exceedances are more likely to occur. In order to have a better overview of the most affected airports, a review of their capacity in supporting operations under low visibility conditions is necessary. Figure 5.1 shows the classification of airports according to ILS capacity in global scale.

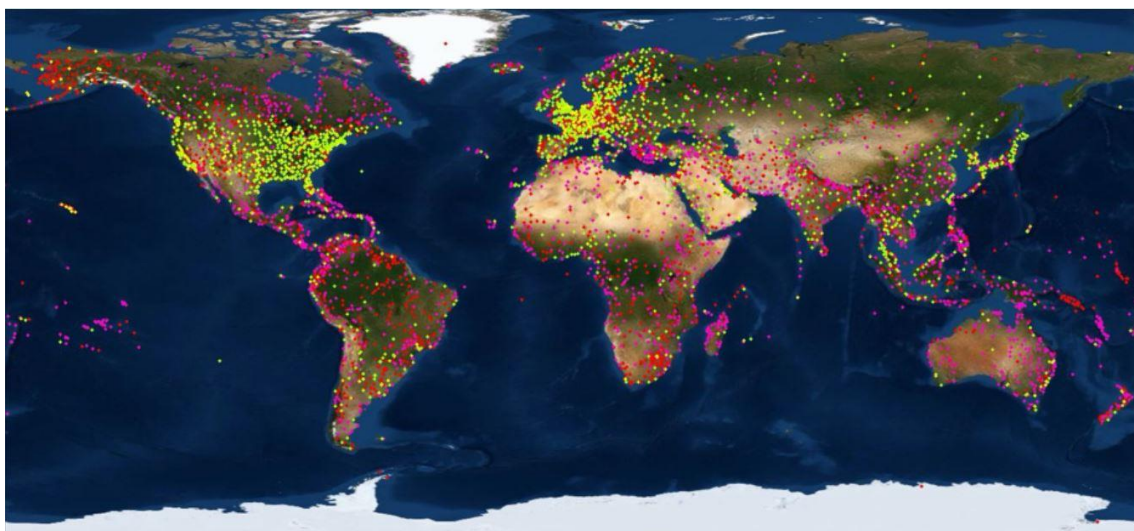


Figure 5.1: A classification of airports according to ILS capacity. Green indicates commercial airport with ILS capacity; yellow: non-commercial ILS; magenta: commercial no ILS; red: non-commercial no ILS.

Extracted from: (Votsis *et al.*, DustClim Technical Report 2020)

According to Fig. 5.1, most of the airports located in the study area do not possess ILS and therefore cannot support operations under IFR. However, the majority of the airports in Saudi Arabia, Lebanon, Israel and Canary Islands, as well as some airports in Egypt, Morocco and the African countries in the coast of the Gulf of Guinea do possess ILS. Regarding the number of airports located in the study area, there are totally 259 airports with scheduled commercial flights distributed between Northern Africa (96 airports), Western Africa (40 airports), South-eastern Mediterranean (18) and the Middle East (105). The countries with the greatest number of airports in NAME are Iran (49 airports), Algeria (34), Saudi Arabia (27), Egypt (11) and the United Arab Emirates (10).

### 5.1.1 *Visibility thresholds for aviation*

The impact analysis methodology for aviation requires a review of the flight rules and regulations. Flight rules are divided into visual flight rules (VFR) and instrument flight rules (IFR). The former is applied when the weather conditions allow the use of visual cues for aircraft navigation, while the latter is employed when aircraft operations under VFR is unsafe. The decision to conduct air operations under either VFR or IFR strongly depends on the weather conditions dominating the region.

In the case of landing and take-off operations, the security conditions are determined by the Aerodrome operating minima (AOM) criteria, which are the limits of usability of an aerodrome defined by ICAO and consist of two parts: i) one related to the cloud base and ii) one related to visibility and the Runway Visual Range. The Runway Visual Range (RVR) is the range over which the pilot of an aircraft can see the runway surface markings or the lights delineating the runway and identify its centre line (ICAO, Manual of All-Weather Operations).

Take-off minima normally consist of a visibility or RVR element exclusively, while approach and landing minima consist of both visibility or RVR, and cloud base elements. Take-off minima depend on the aircraft type, the number of engines that the aircraft possess, the lighting conditions of the runway and the assumed height above the take-off runway in which **engine failure could occur and be compensated**. Thus, visibility and RVR requirements for safe take-off range from 200m to 1500m, according to the Commission Regulation (EC) No 859/2008 of 20 August 2008, amending the Council Regulation (EEC) No 3922/91 of 16 December 1991 on the harmonisation of technical requirements and administrative procedures in the field of civil aviation.

Regarding the approach and landing minima, airports should be divided in those that do possess instrument landing systems and those that are not, hence only VFR can regulate operations. It is internationally agreed that in order to follow

VFR, there must be no cloud within a horizontal distance of 1,500m or within a vertical distance of 1,000ft from the aircraft. Additionally, the flight visibility, defined as the distance ahead that the pilot could see from the cockpit while on flight, must be at least 8,000m. While flying below 10,000ft, a flight visibility of 5,000m is considered enough for pilots to see other aircrafts, as determined in the Commission Regulation (EU) No 748/2012.

On the other hand, airports in which instrument landing systems (ILS) on the runways are available, can follow IFR. There are three main categories of ILS equipment (categories I, II, III), that determine the categories of precision approach and landing operations. Precision approach consists in an instrument approach and landing, using lateral and vertical guidance, provided by a ground-based navigation aid, computer generated navigation data or a controller interpreting the display on a radar. During the approach, the pilot follows the ILS guidance until the decision height (DH) is reached. The special categories of ILS that allow precision approach and secure landing are presented in Table 5.1.

*Table 5.1: Runway Visual Range (RVR) and visibility limits for ILS approach categories for precision approach and landing. Source: ICAO, Manual of all-weather operations*

Category of Operation	Decision Height- DH (m)	RVR (m)	Visibility (m)
CAT I	>60	>550	>800m
CAT II	30<DH<60	>350	-
CAT IIIA	>30 or no DH	>200	-
CAT IIIB	>5 or no DH	50<RVR<200	-
CAT IIIC	No DH limitation	No RVR limitation	-

As it is showed on Table 5.1, operations under IFR require visibility greater than 800m overall, while operations under lower visibilities and RVR are still possible depending on the class of instrumentation that the airport possess.

Furthermore, low visibility procedures (LVP) are established in various aerodromes in support of CAT II/III approaches and landings and for take-offs under RVR below 550 m, enabling the operations of aerodromes in poor weather conditions. Nevertheless, the development and implementation of LVP is quite challenging as it requires the fulfilment of numerous criteria related to the aerodrome infrastructure and equipment and therefore, not all airports can support operations under LVP.

In order to establish the visibility thresholds to be used for the impact assessment, a combination of visual flight rules (VFR), instrument flight rules (IFR) and low visibility procedures (LVP) is proposed, which mark three types of hazards related to approach and landing operations.

*Table 5.2: Visibility thresholds used for the impact analysis of low visibility conditions on air operations.*

Visibility threshold (m)	Procedures applied
Above 5000	VFR
Below 1000	Flow reduction
Below 800	IFR
Below 550	LVP

Air operations might be modified in airports that do not possess instrument landing systems when visibility falls below 5000m. In that case, Air Traffic Control might change the flow of aircrafts. The reduction in the flow of traffic usually is gradual and becomes significant when visibility drops below 1000m, i.e. in the case of sand and dust storms. Under such visibility conditions, up to 50% reduction in flow can occur. The reduction of visibility does not always correlate linearly with changes in the flow of operations, as it does matter how long the reduced visibilities last and at what time of day they occur.

The application of IFR becomes obligatory when visibility falls below 800m, hence airports that do not possess the required instrumentation are affected. The fourth threshold proposed coincides with the visibility limit for the activation of low visibility protocols, i.e. 550m, therefore only airports that fulfill the required criteria of aerodrome infrastructure and equipment can support air operations under these conditions.

## 5.2 Impact analysis results

The results obtained from the impact assessment of SDS in the studied domain are presented in the form of 2-dimensional maps depicting the frequency of exceedance for specific thresholds over the 2-year (2018 and 2019) modelled visibility on 3-hourly basis. Figure 5.2a-f present the maps showing the frequency of exceedance of the thresholds established in section 5.1.1 per aggregation period and grid cell for 2018 and 2019.



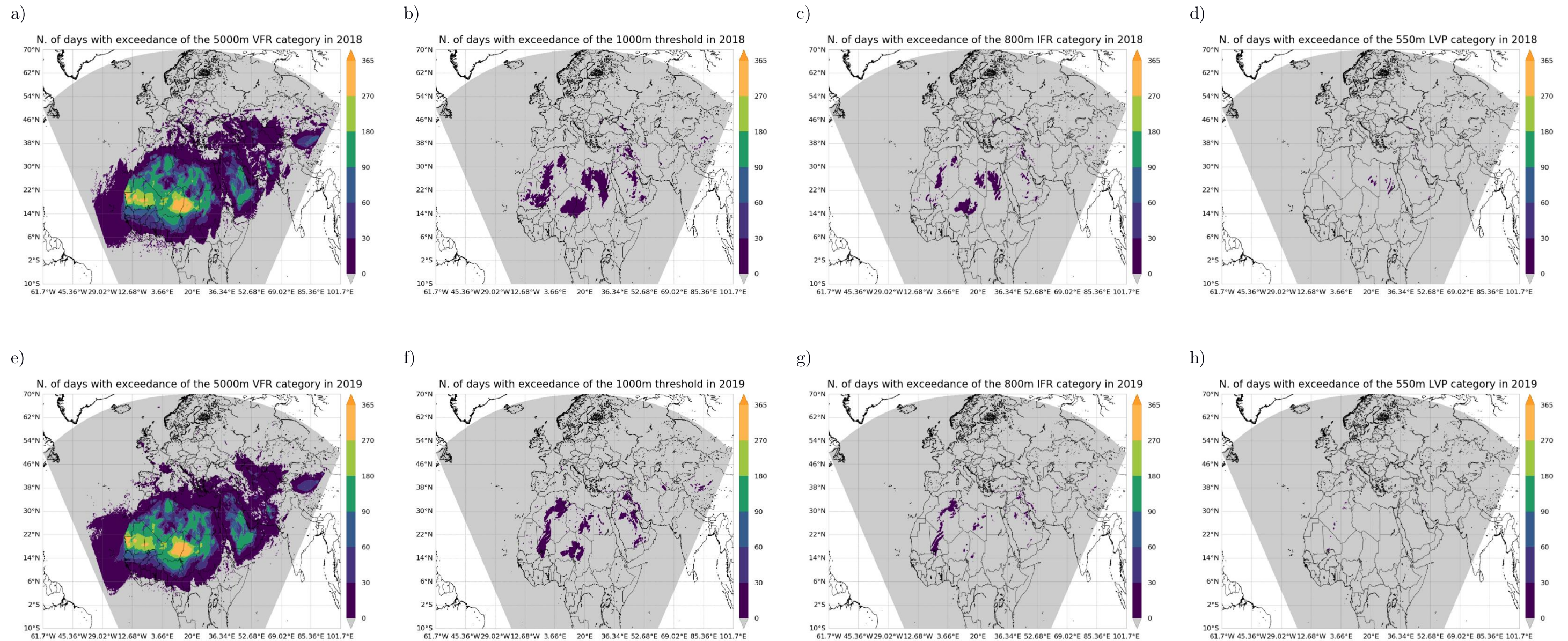


Figure 5.2: Number of days in 2018 and 2019 with exceedance of aviation-related thresholds, indicating possible changes in the applied flight rules and the flow of operations. a) 5000m VFR threshold in 2018, b) 800m IRF threshold in 2018, c) 1000m threshold in 2018, d) 550m VFR threshold in 2018, e) 5000m VFR threshold in 2019, f) 800m IRF threshold in 2018, g) 1000m threshold in 2019, h) 550m VFR threshold in 2019.

As it is observed in Figures 5.2a and 5.2e, the 5000m VRF category has been exceeded during more than half of the days of both 2018 and 2019 in the largest part of the dust belt, leading to possible effects for airports that can only support operations under VFR and to potential modifications of the traffic flow.

Countries located in the Sahel region, such as Western Sahara, Mauritania, Mali, Niger, Chad and west Sudan, have experienced visibility values lower than 5000m more than 90 days per year and for some locations mainly in Mauritania, Niger and Chad more than 270 days per year. Hence, 10 airports in this area have potentially experienced changes in the flow of operations. Countries located in the south of the region, such as Senegal, Guinea and Burkina Faso, hosting 5 airports in total, have been affected from 30 up to 90 days, while Niger, that hosts 5 airports has been affected during more than 90. The countries located in the coast of the Gulf of Guinea have been affected less than 30 days per year. Cape Verde, where 7 airports are installed, and the Canary Islands with 8 airports, are some of the least affected areas, having experienced visibility values lower than 5000m during less than 30 days per year both in 2018 and 2019. Exceedance of the 5000m VRF threshold has been observed in the greatest part of Algeria, Libya, and Egypt during more than 90 days per year, while in the rest of the territory. It must be mentioned that the majority of the 51 airports in total that are hosted by these three countries are located in the less frequently affected areas.

In general, airports located in the South-eastern Mediterranean have been affected less than 30 days per year, with the exception of western Syria the south of Iraq, that have experienced exceedances of the VRF threshold up to 60 days per year. Visibility conditions in Iran, which hosts 49 airports, has been favorable for air operations during the greatest part of 2018 and 2019, with less than 30 days of possible effects. In the Middle East, Saudi Arabia has been the most affected country, experiencing visibility values less than 5000m during up to 180 days per year, while Yemen, Oman and UAE has have been affected during less than 30 days per year, in both 2018 and 2019.

Figures 5.2b and 5.2f show the frequency of exceedance of the 1000m threshold that marks significant reductions in the flow of aircrafts, in 2018 and 2019 respectively. As it can be observed, visibility in the North of Africa has been reduced below 1000m in some locations in Mauritania, Mali, Algeria, Niger, Chad, Libya and the greatest part of Egypt during less than 30 days in 2018. In the Middle East, visibility dropped below 1000m in sparse locations in Saudi Arabia and Iraq during up to 30 days in 2018. In 2019, some affected areas during less than 30 days can be identified in Mali, Algeria, Niger, Chad and sparse locations in Egypt, Libya, Iraq and Saudi Arabia.



Figures 5.2c and 5.2g show the frequency of exceedance of the 800m threshold that requires the application of IFR for safe approach and landing, in 2018 and 2019 respectively. As it can be observed, visibility in the North of Africa has been reduced below 800m in sparse locations in Algeria, Niger, Libya, and Egypt during less than 30 days in 2018. In 2019, some affected areas during less than 30 days can be identified in Mauritania and Algeria. Regarding Western Africa, South-eastern Mediterranean, and the Middle East, there has been no clear impacts in air operations under IFR.

Figures 5.2d and 5.2h show the frequency of exceedance of the 550m threshold that requires the activation of LVP for safe operations. As it is observed, in 2018 visibility has exceeded this threshold during less than 30 days in very few locations in Libya and Egypt, potentially affecting up to 5 airports. In 2019 visibility has not been reduced below 550m in the studied domain.

Overall, the impact assessment of SDS on aviation for 2018 and 2019 reveals that the most frequently affected countries are those located in the Sahel region and the Arabian Peninsula. While visibility values below 5000m have been very frequent (up to 270 days per year), visibility below 800m has potentially affected only sparse location in North Africa with much lower frequency (less than 30 days per year). Furthermore, visibility levels lower than 550m have occurred with almost zero frequency. It is estimated that the real number of cases below 1000m, 800m and 550m is higher. Nevertheless, the weak signals of visibilities below these thresholds in the present analysis were expected, considering the extremely low observed frequency of such values (0.30% in 2018 and 0.14% in 2019), commented in section 4.3, as well as the model's tendency to underestimate such low visibility ranges. This weakness could be attributed to the fact that the NMMB-MONARCH model is not prepared to reproduce haboobs which are intense, short and local SDS that can be associated to extreme reductions of the visibility to a few meters. These types of SDS are common in summer in Sahara and in spring the Iran – Iraq border.

Figures 5.3 and 5.4 helps to identify which time of the day, exceedances of the 5000m VFR category are more likely to occur per aggregation period in timesteps of 3 hours and per grid cell, while the corresponding figures for the 1000m threshold can be found in Appendix C. As it is observed, the most critical hours of the day for visibility to be reduced below 5000m are between 06h and 18h in the greatest part of the studied domain. During these times, visibility exceedance of the VFR threshold has been very frequent in the countries located in Sahel and the Arabian Peninsula, corresponding to more than 25% and up to 50% of the year. Although exceedances are less frequent during the night and in early hours, they do occur up to 90 days per year in some locations in the west and central

Sahel. While for these areas a clear diurnal pattern is identified, South-eastern Mediterranean and the countries located in the coast of the Gulf of Guinea present no such pattern, as they experience exceedances with almost the same frequency during all times. To better assess the impact that such exceedances have for aviation, it is prudent to take into account that the busiest hours for the airports located in Middle East are at nighttime, with 02h being prime time in Dubai, Doha and much of Saudi Arabia.

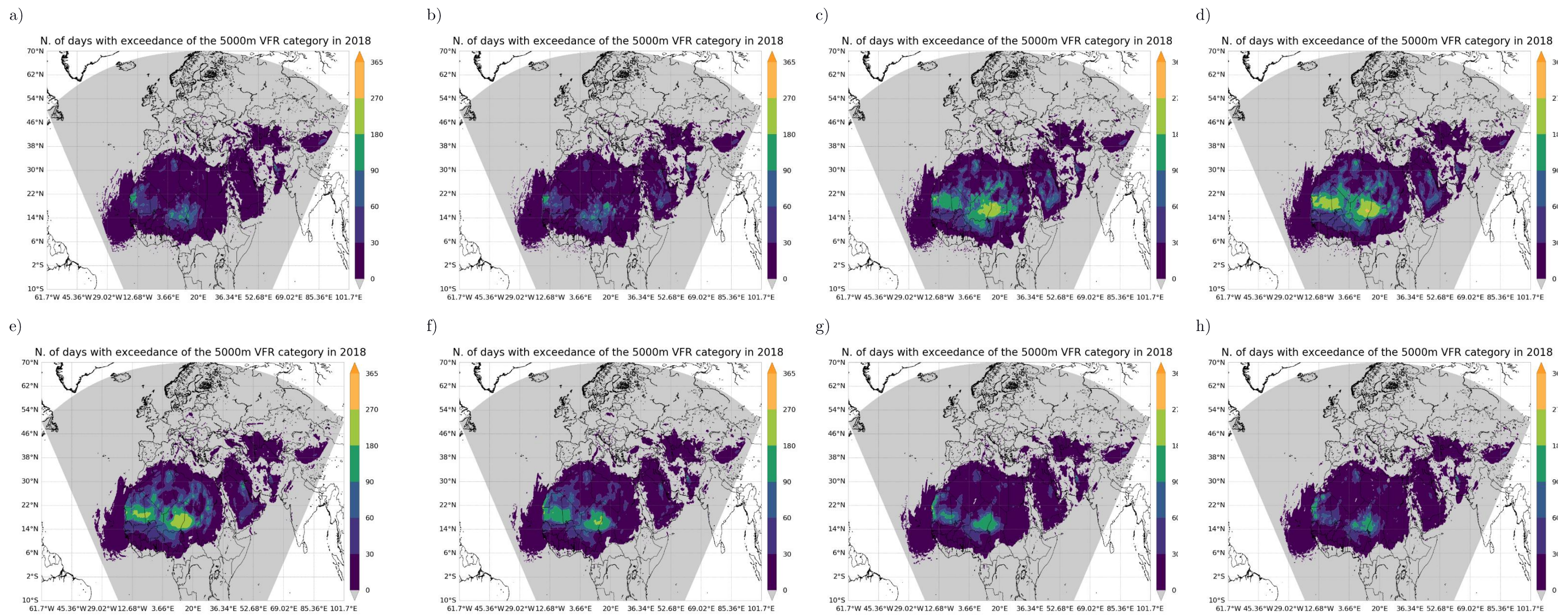


Figure 5.3: Frequency of exceedance of the 5000m VFR category per 3-hourly timesteps and grid cell during 2018. a) Valid for 00h, b) Valid for 03h, c) Valid for 06h, d) Valid for 09h, e) Valid for 12h, f) Valid for 15h, g) Valid for 18h, h) Valid for 21h



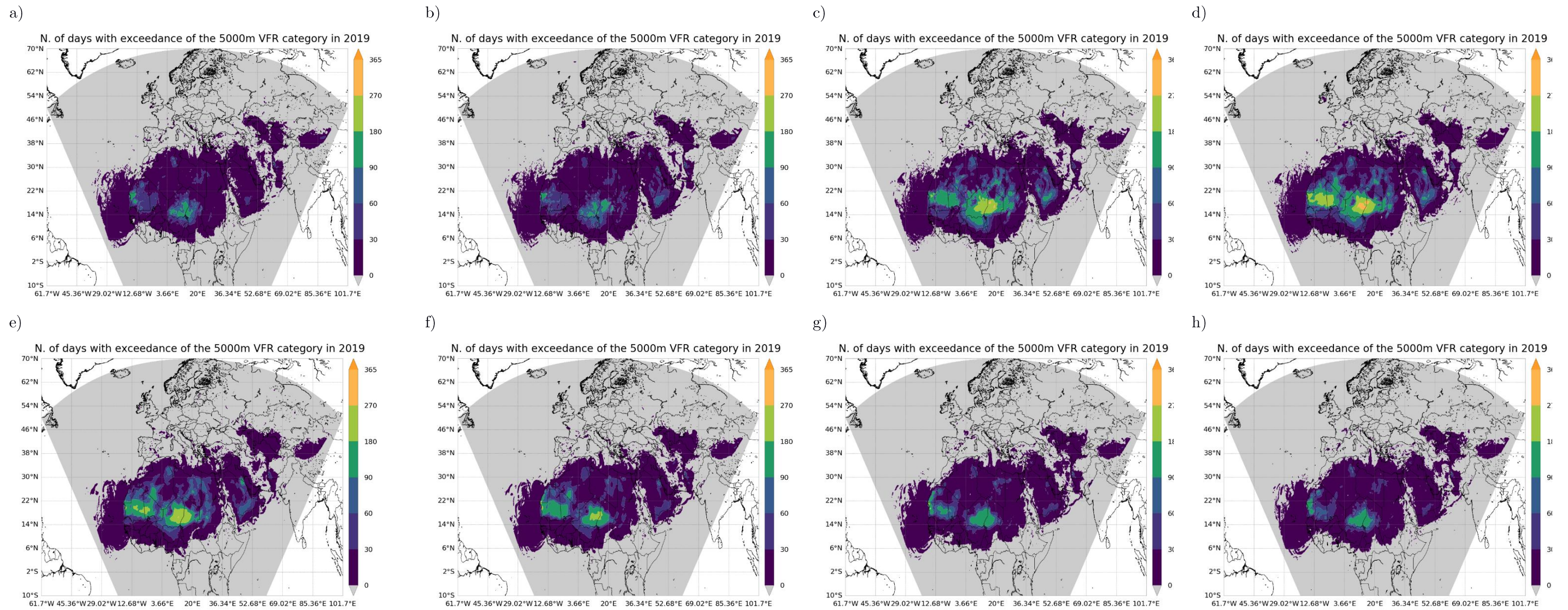


Figure 5.4: Frequency of exceedance of the 5000m VFR category per 3-hourly timesteps and grid cell during 2019. a) Valid for 00h, b) Valid for 03h, c) Valid for 06h, d) Valid for 09h, e) Valid for 12h, f) Valid for 15h, g) Valid for 18h, h) Valid for 21h.

## 6 End-user product proposal

The creation of end-user products targeted to the aviation sector consists in translating the scientific outcome of numerical prediction models into products that permit users to understand the environmental risks related to air operations and reduce them or make use of available technologies to compensate them to the widest possible extent. Aviation products should provide information in location-specific format, both numerical and visual and should be developed considering the objective risks that sand and dust could pose for the aviation sector, as well as the operational requirements stated by end-users.

There are numerous end-user products that could be designed to serve the needs of the aviation sector, making use of the scientific outcomes of the NMMB-MONARCH model, since the multiple variables calculated by the model offer various possibilities. These possibilities should be assessed in the context of an operational center, such as the WMO Barcelona Dust Forecast Center, considering both the user needs and the technical requirements that need to be met by an operational forecast.

The assessment of the user needs requires thorough knowledge of the sector, as well as the capacity to identify the objective threats related to sand and dust storms. The revision of the flight rules, presented in section 5.1.1 provided the key thresholds, the exceedance of which could pose at risk key aspects of flight, airport, and maintenance operations. It has also become evident that visibility conditions are a key factor for the definition of the different operation categories and the equipment required. Hence, the need for a forecast that predicts visibility, while implements the visibility thresholds related to aviation has emerged.

The proposed visibility forecast relies on the conversion of the surface extinction coefficient predictions of the NMMB-MONARCH model, using the calibrated Koschmieder equation (see section 4.4). The proposed visibility forecast is suggested to be implemented under the framework of the WMO Barcelona Dust Forecast Center, hosted by the consortium formed by the Spanish State Meteorological Center (AEMET) and the Barcelona Supercomputing Center (BSC).

Since forecast evaluation is an essential step for all predictions used for operational purposes, as it provides a measure of confidence and accuracy of the derived forecast products, NRT-evaluation of the proposed visibility forecast should be available to users. As this type of evaluation can be perceived as a routine evaluation, it is important to have timely delivered observations on a regular basis. Visibility observations from METAR and SYNOP are available in



near-real-time through international platforms, such as OGIMET and the methodology for the evaluation of such forecast has been established in section 4.2.

The values of visibility obtained by the conversion of the dust surface extinction coefficient predictions of the NMMB-MONARCH model should be daily plotted for the reference area of the Barcelona Dust Forecast Center and made available at the end of each day using the results of the simulation starting the same day at 12 UTC. The forecasts released by the NMMB-MONARCH have a temporal resolution of 3 hours and can predict up to 72 hours ahead, thus making the product a powerful tool to issue short-term predictions.

A sample visibility forecast for February 12-13, 2018 is presented in Figure 6.1. The forecast is the visualisation of the simulation run on the 12<sup>th</sup> of February at 12UTC and it consists of 9 timesteps covering the next 24 hours with a 3-hourly resolution.

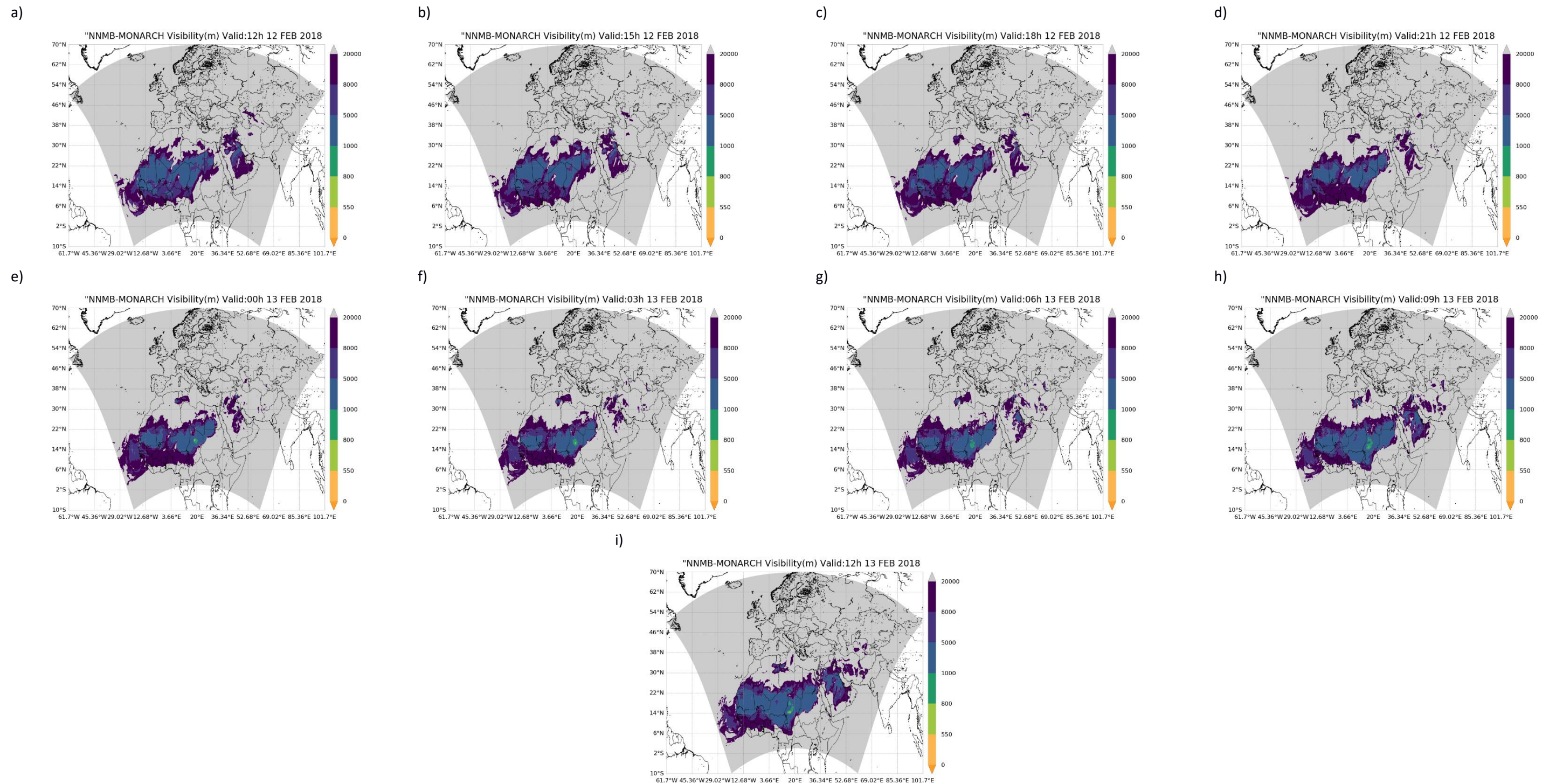


Figure 6.1: Visibility forecast for 12-13 February 2018 . a) Valid for 12h of 12 Feb 2018, b) Valid for 15h of 12 Feb 2018, c) Valid for 18h of 12 Feb 2018, d) Valid for 21h of 12 Feb 2018, e) Valid for 00h of 13 Feb 2018, f) Valid for 03 of 13 Feb 2018, g) Valid for 06h of 13 Feb 2018, h) Valid for 09h of 13 Feb 2018, i) Valid for 12h of 13 Feb 2018.

According to the visibility forecast presented in Figure 6.1, visibility values lower than 5000m are predicted for the 12<sup>th</sup> of February 2018, at 12h (Figure 6.1a) and 15h (Figure 6.1b) in various African countries. More specifically, various locations in Mauritania, Mali, Senegal, Niger, south-western Algeria, Chad, southeast Libya, and west Egypt experience visibilities below 5000m due to the presence of dust. In the Middle East, the presence of dust leads to visibility reduction below 5000m in some locations in Arabia Saudi and Iraq. During the same hours, the Canary Islands, Cape Verde, the African countries in the Gulf of Guinea, Morocco, Iran, and the Mediterranean coast experience visibility conditions favorable for air operations under VFR.

The forecast for 18h (Figure 6.1c) indicates that visibility values below 5000m persist in Mauritania, Mali, Senegal, Niger, Chad, Libya, and southwestern Egypt. Even though visibility conditions are improved in the Arabian Peninsula, some locations around the Persian Gulf still experience visibility values below 5000m. The forecast for 21h (Figure 6.1d) suggests an improvement in visibility conditions in Senegal and a further improvement in the Arabian Peninsula, while visibility values below 5000m persist in the dust belt.

The forecast for the early hours of the next day, 13<sup>th</sup> of February, shows that visibility values below 5000m are experienced in the greatest part of Mauritania, Mali, Niger, Libya and Egypt, while values even below 1000m are predicted in central Chad, suggesting a local dust outbreak (Figures 6.1e-g). During the same hours, the visibility conditions in the Middle East and the Mediterranean coast are favorable for air operations. At 9h and 12h, a general deterioration of the visibility conditions is predicted for the whole domain, with visibility reduction below 5000m in all countries located in the dust belt and the greatest part of the Arabian Peninsula, while the dust outbreak in Chad persists, moving to the south-west of the country.

Overall, the forecast for the 12<sup>th</sup> of February at 12h and the following 24 hours suggests quite unfavorable visibility conditions for the greatest part of the domain. Airports located in the dust belt experience reduced visibility conditions during the whole forecasted time period. Therefore, airports that can only support operations under VRF might suffer schedule disturbances. Moreover, airports located close to the epicenter of the dust outbreak in Chad are highly affected on the 13<sup>th</sup> of February. In the Middle East, late hour operations on the 12<sup>th</sup> of February and early morning operations on the 13<sup>th</sup> are less likely to be affected by visibility conditions, while the forecast is favorable for the countries located in the Gulf of Guinea, Cape Verde, Iran, and the Canary Islands of Spain.

The proposed visibility forecast should be available at the official webpage of the WMO Barcelona Dust Forecast Center. Although at the present work the visualisation consists of static maps, it is highly suggested that the forecast is implemented as an

interactive animated map with a pause option for each timestep and specific numerical values for visibility where the airports are located, available upon click. Additionally, since the NMMB-MONARCH model offers predictions for up to 72h ahead, the final product should include 24 timesteps of 3hourly predictions. A special section with the comparison to near-real-time observations of the forecast should be included to reinforce the credibility of the predictions offered and to facilitate its objective interpretation by the users.

## 7 Conclusions

The present work has endeavored to establish a methodology to evaluate the predictions of the **NMMB-MONARCH model with visibility observations** obtained from meteorological reports. The conducted evaluation relied on the PM10 dust surface concentration and the surface extinction coefficient at 550nm predicted by the NMMB-MONARCH model, while observations of horizontal visibility and meteorological data were obtained from the Integrated Surface Database of the National Climatic Data Center (NCDC-ISD). For the conversion of the model output to visibility, **five diagnostics have been tested**: the Koschmieder and the Biral which are physically based expressions using the surface extinction coefficient and the IZO, DA and Dayan, empirical equations that use the PM10 dust surface concentration.

Since the visibility observations have been found to be categorical, the need for **categorical evaluation** has arisen. Hence, the model predictions have been classified in 4 categories covering visibility values between 0 and 20km. The process followed for the categorical evaluation has served to **establish the methodology for verification with visibility observations**, as well as to assess the suitability of the five tested diagnostics in predicting visibility. The filtering of observations based on relative humidity to discard cases of reduced visibility due to hydrometeors has been proven useful, while the careful selection of the stations that provide observations is also crucial.

The overall results of the evaluation revealed high accuracy in predicting the right visibility category for all diagnostics. Their accuracies range from 0.78 to 0.82 in 2018 and from 0.81 to 0.86 in 2019, except for the Dayan diagnostic that systematically presents significantly lower accuracy to its predictions (0.57 in 2018 and 0.58 in 2019). The remaining empirical diagnostics (DA and IZO) provide highly accurate predictions for the whole domain and relatively low frequencies of overestimation and underestimation of visibility categories.

While the overestimation frequency is lower in the case of the DA diagnostic, IZO proves to be more accurate in its predictions among different sub-regions and therefore, it has been selected as the reference empirical diagnostic for the studied domain. The physically based diagnostics, Koschmieder and Biral, present the highest accuracy in their predictions for the whole domain (0.82 in 2018 and 0.86 in 2019) and the lowest tendency to overestimate, compared to the empirical. Additionally, as they rely on a physical basis, their results are not regionally sensitive, meaning that they can be applicable to other regions beyond NAME, which is an important advantage, considering the that the NMMB-MONARCH is multiscale, i.e. can run simulations in different regional and global domains. Hence, the use of the physically based diagnostics



is preferable. Aiming to improve their predictions, reduce the frequency of underestimation of visibility categories and improve the hit rates for the most poorly represented categories, a calibration of the Koschmieder diagnostic has been endeavored. Among the three conversion factors that have been tested (1.5, 2.0 and 2.5), the results of the Koschmieder formula calibrated with a factor of 1.5, have shown similar performance to IZO. Therefore, the proposed diagnostic for visibility in the NAME domain, based on the output of the NMMB-MONARCH model is the calibrated Koschmieder diagnostic, with conversion factor 1.5.

Based on the visibility obtained by the calibrated Koschmieder diagnostic, the impact analysis for the aviation sector revealed that visibility has been reduced below 5000m more than half of the days of 2018 and 2019 in the largest part of the dust belt, leading to possible effects for airports that can only support operations under VFR and to potential modifications of the flow of aircrafts in the majority of the 259 airports with scheduled commercial flights located in the study area. Significant modifications in the aircrafts flow might have occurred during up to 30 days per year in various locations in North Africa and sparse locations in the Middle East, upon exceedance of the 1000m threshold. Additionally, the 800m threshold that marks the necessity to use ILS to conduct safe air operations has been exceeded less than 30 days in various locations, while the 550m threshold that requires the activation of LVP has not been exceeded in the greatest part of the studied domain. Concerning the exceedances of the 800m and 550m thresholds, estimated in the present analysis, it is highlighted that these estimations are subjected to the model's ability to predict the corresponding visibility ranges.

The **most frequently affected countries** by the presence of dust are those located in the **Sahel region and the Arabian Peninsula**, while the **most critical hours** of the day for visibility to be reduced below 5000m are **between 6h and 18h** in the greatest part of the studied domain, suggesting a diurnal pattern for the visibility conditions that dominate the area. Luckily enough, the busiest hours for the airports located in the region is at nighttime with 2am being prime time in Israel, Dubai, Doha and much of Saudi Arabia.

Considering that visibility conditions are a key factor for air operations, the design of a forecast that predicts visibility reduction due to SDS, while implements aviation-related visibility thresholds, constitutes an effort to connect the dust research conducted by the scientific community with socio-economic sectors. The result is a powerful tool that permits users from the aviation sector to understand and mitigate the environmental risks related to air operations. The proposed dust-visibility forecast could be considered for implementation under the framework of the WMO Barcelona Dust Forecast Center.



## 8 References

- Al-Hemoud, A. *et al.* (2017) ‘Socioeconomic effect of dust storms in Kuwait’, *Arabian Journal of Geosciences*. Springer Verlag, 10(1), pp. 1–9. doi: 10.1007/s12517-016-2816-9.
- Amiridis, V. *et al.* (2015) ‘LIVAS: a 3-D multi-wavelength aerosol/cloud database based on CALIPSO and EARLINET’, *Atmospheric Chemistry and Physics*. Copernicus GmbH, 15(13), pp. 7127–7153. doi: 10.5194/acp-15-7127-2015.
- Andreae, M. O. and Rosenfeld, D. (2008) ‘Aerosol-cloud-precipitation interactions. Part 1. The nature and sources of cloud-active aerosols’, *Earth-Science Reviews*. Elsevier, 89(1–2), pp. 13–41. doi: 10.1016/j.earscirev.2008.03.001.
- Ansmann, A. *et al.* (2003) ‘Long-range transport of Saharan dust to northern Europe: The 11–16 October 2001 outbreak observed with EARLINET’, *Journal of Geophysical Research: Atmospheres*. Blackwell Publishing Ltd, 108(24). doi: 10.1029/2003jd003757.
- Ansmann, A. *et al.* (2017) ‘Profiling of Saharan dust from the Caribbean to West Africa, Part 2: Shipborne lidar measurements versus forecasts’. doi: 10.5194/acp-2017-502.
- AR4 Climate Change 2007: Synthesis Report — IPCC* (no date). Available at: <https://www.ipcc.ch/report/ar4/syr/> (Accessed: 14 April 2020).
- AR5 Climate Change 2013: The Physical Science Basis — IPCC* (no date). Available at: <https://www.ipcc.ch/report/ar5/wg1/> (Accessed: 14 April 2020).
- Badarinath, K. V. S. *et al.* (2010) ‘Long-range transport of dust aerosols over the Arabian Sea and Indian region - A case study using satellite data and ground-based measurements’, *Global and Planetary Change*. Elsevier, 72(3), pp. 164–181. doi:10.1016/j.gloplacha.2010.02.003.
- Balkanski, Y. *et al.* (2007) ‘Atmospheric Chemistry and Physics’, *Reevaluation of Mineral aerosol radiative forcings suggests a better agreement with satellite and AERONET data*, 7(1), pp. 81–95. Available at: [www.atmos-chem-phys.net/7/81/2007/](http://www.atmos-chem-phys.net/7/81/2007/)
- Banks, J. R. and Brindley, H. E. (2013) ‘Evaluation of MSG-SEVIRI mineral dust retrieval products over North Africa and the Middle East’, *Remote Sensing of Environment*. Elsevier, 128, pp. 58–73. doi: 10.1016/j.rse.2012.07.017.
- Basart, S. *et al.* (2009) ‘Aerosol characterization in Northern Africa, Northeastern Atlantic, Mediterranean Basin and Middle East from direct-sun AERONET observations’, *Atmospheric Chemistry and Physics*. European Geosciences Union, 9(21), pp. 8265–8282. doi: 10.5194/acp-9-8265-2009.
- Biscaye, P. E. *et al.* (1997) ‘Asian provenance of glacial dust (stage 2) in the Greenland Ice Sheet Project 2 Ice Core, Summit, Greenland’, *Journal of Geophysical Research: Oceans*. Blackwell Publishing Ltd, 102(C12), pp. 26765–26781. doi: 10.1029/97JC01249.
- Bory, A. J.-M. *et al.* (2003) ‘Regional variability of ice core dust composition and provenance in Greenland’, *Geochemistry, Geophysics, Geosystems*. John Wiley & Sons, Ltd, 4(12). doi: 10.1029/2003GC000627.
- Bory, A. J. M. *et al.* (2002) ‘Seasonal variability in the origin of recent atmospheric mineral dust at NorthGRIP, Greenland’, *Earth and Planetary Science Letters*. Elsevier B.V., 196(3–

- 4), pp. 123–134. doi: 10.1016/S0012-821X(01)00609-4.
- Boucher, O., D. Randall, P. Artaxo, C. Bretherton, G. Feingold, P. Forster, V.-M. Kerminen, Y. Kondo, H. Liao, U. and Lohmann, P. Rasch, S.K. Satheesh, S. Sherwood, B. S. and X. Y. Z. (2013) ‘Clouds and Aerosols. In: Climate Change 2013: The Physical Science Basis. Contribution of Working Group I to the Fifth Assessment Report of the Intergovernmental Panel on Climate Change’.
- Cabello, M. *et al.* (2012) ‘Spatial and temporal variation of the impact of an extreme Saharan dust event’, *Journal of Geophysical Research: Atmospheres*. Blackwell Publishing Ltd, 117(D11), p. n/a-n/a. doi: 10.1029/2012JD017513.
- Camino, C. *et al.* (2015) ‘An empirical equation to estimate mineral dust concentrations from visibility observations in Northern Africa’, *Aeolian Research*. doi: 10.1016/j.aeolia.2014.11.002.
- Carrer, D. *et al.* (2010) ‘Daily estimates of aerosol optical thickness over land surface based on a directional and temporal analysis of SEVIRI MSG visible observations’, *Journal of Geophysical Research Atmospheres*. Blackwell Publishing Ltd, 115(10). doi: 10.1029/2009JD012272.
- Chadwick, O. A. *et al.* (1999) ‘Changing sources of nutrients during four million years of ecosystem development’, *Nature*. Nature Publishing Group, pp. 491–497. doi: 10.1038/17276.
- Chepil, W. S. and Woodruff, N. P. (1957) ‘Sedimentary characteristics of dust storms; Part II, Visibility and dust concentration’, *American Journal of Science*. American Journal of Science (AJS), 255(2), pp. 104–114. doi: 10.2475/ajs.255.2.104.
- Cuevas, E. *et al.* (2015) ‘The MACC-II 2007–2008 reanalysis: atmospheric dust evaluation and characterization over northern Africa and the Middle East’, *Atmospheric Chemistry and Physics*. Copernicus GmbH, 15(8), pp. 3991–4024. doi: 10.5194/acp-15-3991-2015.
- D’Almeida, G. A. (1986) ‘A Model for Saharan Dust Transport’, [http://dx.doi.org/10.1175/1520-0450\(1986\)025<0903:AMFSDT>2.0.CO;2](http://dx.doi.org/10.1175/1520-0450(1986)025<0903:AMFSDT>2.0.CO;2). doi: 10.1175/1520-0450(1986)025<0903:AMFSDT>2.0.CO;2.
- Dai, A. (2011) ‘Drought under global warming: A review’, *Wiley Interdisciplinary Reviews: Climate Change*. Wiley-Blackwell, pp. 45–65. doi: 10.1002/wcc.81.
- Dayan, U. *et al.* (2008) ‘Suspended dust over southeastern Mediterranean and its relation to atmospheric circulations’, *International Journal of Climatology*. John Wiley & Sons, Ltd, 28(7), pp. 915–924. doi: 10.1002/joc.1587.
- Duce, R. A. *et al.* (1980) ‘Long-range atmospheric transport of soil dust from Asia to the tropical North Pacific: Temporal variability’, *Science*. American Association for the Advancement of Science, 209(4464), pp. 1522–1524. doi: 10.1126/science.209.4464.1522.
- Duce, R. A. and Tindale, N. W. (1991) ‘Atmospheric transport of iron and its deposition in the ocean’, *Limnology and Oceanography*. John Wiley & Sons, Ltd, 36(8), pp. 1715–1726. doi: 10.4319/lo.1991.36.8.1715.
- Engelstaedter, S., Tegen, I. and Washington, R. (2006) ‘North African dust emissions and transport’, *Earth-Science Reviews*. Elsevier, 79(1–2), pp. 73–100. doi:

10.1016/j.earscirev.2006.06.004.

Formenti, P. *et al.* (2001) ‘Saharan dust in Brazil and Suriname during the Large-Scale Biosphere-Atmosphere Experiment in Amazonia (LBA) - Cooperative LBA Regional Experiment (CLAIRE) in March 1998’, *Journal of Geophysical Research Atmospheres*. Blackwell Publishing Ltd, 106(D14), pp. 14919–14934. doi: 10.1029/2000JD900827.

Gama, C. *et al.* (2015) ‘Seasonal patterns of Saharan dust over Cape Verde - a combined approach using observations and modelling’, *Tellus, Series B: Chemical and Physical Meteorology*. Co-Action Publishing, 67(1). doi: 10.3402/tellusb.v67.24410.

García-Pando, C. P. *et al.* (2014) ‘Soil Dust Aerosols and Wind as Predictors of Seasonal Meningitis Incidence in Niger’, *Environmental Health Perspectives*. Public Health Services, US Dept of Health and Human Services, 122(7), pp. 679–686. doi: 10.1289/ehp.1306640.

Garrison, V. H. *et al.* (2003) ‘African and Asian dust: From desert soils to coral reefs’, *BioScience*. American Institute of Biological Sciences, pp. 469–480. doi: 10.1641/0006-3568(2003)053[0469:AAADFD]2.0.CO;2.

Giannadaki, D., Pozzer, A. and Lelieveld, J. (2014) ‘Atmospheric Chemistry and Physics Modeled global effects of airborne desert dust on air quality and premature mortality’, *Atmos. Chem. Phys. Discuss*, 14, pp. 957–968. doi: 10.5194/acp-14-957-2014.

Ginoux, P. *et al.* (2001) ‘Sources and distributions of dust aerosols simulated with the GOCART model’, *Journal of Geophysical Research Atmospheres*. Blackwell Publishing Ltd, 106(D17), pp. 20255–20273. doi: 10.1029/2000JD000053.

Ginoux, P. *et al.* (2012) ‘Global-scale attribution of anthropogenic and natural dust sources and their emission rates based on MODIS Deep Blue aerosol products’, *Reviews of Geophysics*. Blackwell Publishing Ltd. doi: 10.1029/2012RG000388.

Goudie, A., Livingstone, I. and Stokes, S. (1999) *Aeolian environments, sediments, and landforms, British geomorphological research group symposia series*.

Haustein, K. *et al.* (2012) ‘Atmospheric dust modeling from meso to global scales with the online NMMB/BSC-Dust model-Part 2: Experimental campaigns in Northern Africa’, *Atmos. Chem. Phys*, 12, pp. 2933–2958. doi: 10.5194/acp-12-2933-2012.

Heinold, B. *et al.* (2008) ‘Dust radiative feedback on Saharan boundary layer dynamics and dust mobilization’, *Geophysical Research Letters*. John Wiley & Sons, Ltd, 35(20), p. L20817. doi: 10.1029/2008GL035319.

Hsu, N. C. *et al.* (2012) ‘Global and regional trends of aerosol optical depth over land and ocean using SeaWiFS measurements from 1997 to 2010’, *Atmospheric Chemistry and Physics*, 12(17), pp. 8037–8053. doi: 10.5194/acp-12-8037-2012.

Huneus, N. *et al.* (2011) ‘Global dust model intercomparison in AeroCom phase I’, pp. 7781–7816. doi: 10.5194/acp-11-7781-2011.

Jackson, J. M. *et al.* (2013) ‘Suomi-NPP VIIRS aerosol algorithms and data products’, *Journal of Geophysical Research: Atmospheres*. Blackwell Publishing Ltd, 118(22), pp. 12,673–12,689. doi: 10.1002/2013JD020449.

Janjic, Z. and Gall, R. (2012) ‘Scientific Documentation of the NCEP Nonhydrostatic

- Multiscale Model on the B grid (NMMB). Part 1 Dynamics', *NCAR Tech. Note*, (April), pp. 1–80. doi: 10.5065/D6WH2MZX.
- Jugder, D. *et al.* (2014) 'Quantitative analysis on windblown dust concentrations of PM10 (PM2.5) during dust events in Mongolia', *Aeolian Research*. Elsevier, 14, pp. 3–13. doi: 10.1016/j.aeolia.2014.04.005.
- Jusot, J. F. *et al.* (2017) 'Airborne dust and high temperatures are risk factors for invasive bacterial disease', *Journal of Allergy and Clinical Immunology*. Mosby Inc., 139(3), pp. 977–986.e2. doi: 10.1016/j.jaci.2016.04.062.
- Klose, M. *et al.* (2010) 'Sahel dust zone and synoptic background', *Geophysical Research Letters*. John Wiley & Sons, Ltd, 37(9), p. n/a-n/a. doi: 10.1029/2010GL042816.
- Knippertz, P. and Stuut, J. B. W. (2014) *Mineral dust: A key player in the earth system*, *Mineral Dust: A Key Player in the Earth System*. Springer Netherlands. doi: 10.1007/978-94-017-8978-3.
- Kohfeld, K. E. and Tegen, I. (2007) 'Record of Mineral Aerosols and Their Role in the Earth System', in *Treatise on Geochemistry*. Elsevier Inc., pp. 1–26. doi: 10.1016/B978-008043751-4/00236-4.
- Kosmopoulos, P. G. *et al.* (2017) 'Dust impact on surface solar irradiance assessed with model simulations, satellite observations and ground-based measurements', *Atmospheric Measurement Techniques*. Copernicus GmbH, 10(7), pp. 2435–2453. doi: 10.5194/amt-10-2435-2017.
- Lawrence, M. G. (2005) 'The Relationship between Relative Humidity and the Dewpoint Temperature in Moist Air A Simple Conversion and Applications'. doi: 10.1175/BAMS-86-2-225.
- Lekas, T. I. *et al.* (2014) 'Some considerations related to flight in dusty conditions', *Journal of Aerospace Operations*. IOS Press, 3, pp. 45–56. doi: 10.3233/AOP-140043.
- Levy, R. C. *et al.* (2010) 'Atmospheric Chemistry and Physics Global evaluation of the Collection 5 MODIS dark-target aerosol products over land', *Atmos. Chem. Phys*, 10, pp. 10399–10420. doi: 10.5194/acp-10-10399-2010.
- Luo, C. (2004) 'Temporal variability of dust mobilization and concentration in source regions', *Journal of Geophysical Research*. John Wiley & Sons, Ltd, 109(D20), p. D20202. doi: 10.1029/2004JD004861.
- Mahowald, N. M. *et al.* (2005) 'Atmospheric global dust cycle and iron inputs to the ocean', *Global Biogeochemical Cycles*, 19(4). doi: 10.1029/2004GB002402.
- Mahowald, N. M. *et al.* (2007) 'Global trends in visibility: implications for dust sources' *Atmospheric Chemistry and Physics*, 7, pp. 3309–3339. doi: 10.5194/acp-7-3309-2007.
- Mahowald, N. M. *et al.* (2010) 'Observed 20th century desert dust variability: impact on climate and biogeochemistry', *Atmospheric Chemistry and Physics*, 10(22), pp. 10875–10893. doi: 10.5194/acp-10-10875-2010.
- Mahowald, N. M. *et al.* (2017) 'Aerosol Deposition Impacts on Land and Ocean Carbon Cycles', *Current Climate Change Reports*. Springer, pp. 16–31. doi: 10.1007/s40641-017-0056-

z.

*Managing the Risks of Extreme Events and Disasters to Advance Climate Change Adaptation* — IPCC (2013). Available at: <https://www.ipcc.ch/report/managing-the-risks-of-extreme-events-and-disasters-to-advance-climate-change-adaptation/>.

Marticorena, B. and Bergametti, G. (1995) 'Modeling the atmospheric dust cycle: 1. Design of a soil-derived dust emission scheme', *Journal of Geophysical Research*. John Wiley & Sons, Ltd, 100(D8), pp. 16415–16430. doi: 10.1029/95jd00690.

McTainsh, G. H. and Pitblado, J. R. (1987) 'Dust storms and related phenomena measured from meteorological records in Australia', *Earth Surface Processes and Landforms*. John Wiley & Sons, Ltd, 12(4), pp. 415–424. doi: 10.1002/esp.3290120407.

Meywerk, J. and Ramanathan, V. (1999) 'Observations of the spectral clear-sky aerosol forcing over the tropical Indian Ocean', *Journal of Geophysical Research*, 104(D20), pp. 24,359–24,370, doi: 10.1029/1999JD900502.

Middleton, N. J. and Goudie, A. S. (2001) 'Saharan dust: Sources and trajectories', *Transactions of the Institute of British Geographers*. John Wiley & Sons, Ltd, 26(2), pp. 165–181. doi: 10.1111/1475-5661.00013.

Ben Mohamed, A. *et al.* (1992) 'Spatial and temporal variations of atmospheric turbidity and related parameters in Niger', *Journal of Applied Meteorology*, 31(11), pp. 1286–1294. doi: 10.1175/1520-0450(1992)031<1286:satvoa>2.0.co;2.

Mona, L. *et al.* (2012) 'Lidar Measurements for Desert Dust Characterization: An Overview', *Advances in Meteorology*. Hindawi Publishing Corporation, 2012, p. 36. doi: 10.1155/2012/356265.

Ničković, S. *et al.* (1996) 'A Model for Long-Range Transport of Desert Dust', *Mon. Wea. Rev.* (1996) 124(11) pp. 2537–2544, doi: 10.1175/1520-0493(1996)124<2537:AMFLRT>2.0.CO;2.

O'Loingsigh, T. *et al.* (2014) 'The Dust Storm Index (DSI): A method for monitoring broadscale wind erosion using meteorological records', *Aeolian Research*, 12, pp. 29–40. doi: 10.1016/j.aeolia.2013.10.004.

Parrington, J. R., Zoller, W. H. and Aras, N. K. (1983) 'Asian dust: Seasonal transport to the Hawaiian Islands', *Science*. American Association for the Advancement of Science, 220(4593), pp. 195–197. doi: 10.1126/science.220.4593.195.

Patterson, E. M. and Gillette, D. A. (1977) 'COMMONALITIES IN MEASURED SIZE DISTRIBUTIONS FOR AEROSOLS HAVING A SOIL-DERIVED COMPONENT.', *J Geophys Res.* John Wiley & Sons, Ltd, 82(15), pp. 2074–2082. doi: 10.1029/JC082i015p02074.

Pérez, C. *et al.* (2006) 'Interactive dust-radiation modeling: A step to improve weather forecasts', *Journal of Geophysical Research Atmospheres*. Blackwell Publishing Ltd, 111(16), p. D16206. doi: 10.1029/2005JD006717.

Pérez, C. *et al.* (2011) 'Atmospheric dust modeling from meso to global scales with the online NMMB/BSC-Dust model - Part 1: Model description, annual simulations and evaluation',



- Atmospheric Chemistry and Physics*, 11(24), pp. 13001–13027. doi: 10.5194/acp-11-13001-2011.
- Perry, K. D. *et al.* (1997) ‘Long-range transport of North African dust to the eastern United States’, *Journal of Geophysical Research Atmospheres*, 102(10), pp. 11225–11238. doi: 10.1029/97jd00260.
- Prospero, J. M. (1999) ‘Long-range transport of mineral dust in the global atmosphere: Impact of African dust on the environment of the southeastern United States’, *Proceedings of the National Academy of Sciences of the United States of America*. National Academy of Sciences, 96(7), pp. 3396–3403. doi: 10.1073/pnas.96.7.3396.
- Prospero, J. M. *et al.* (2002) ‘Environmental characterization of global sources of atmospheric soil dust identified with the Nimbus 7 Total Ozone Mapping Spectrometer (TOMS) absorbing aerosol product’, *Reviews of Geophysics*. Blackwell Publishing Ltd, 40(1), pp. 2-1-2-31. doi: 10.1029/2000RG000095.
- Prospero, J. M., Glaccum, R. A. and Nees, R. T. (1981) ‘Atmospheric transport of soil dust from Africa to South America’, *Nature*. Nature Publishing Group, 289(5798), pp. 570–572. doi: 10.1038/289570a0.
- IPCC, 2013: Summary for Policymakers. In: Climate Change 2013: The Physical Science Basis. Contribution of Working Group I to the Fifth Assessment Report of the Intergovernmental Panel on Climate Change
- M. C., Fung, I. and McFarlane, N. (1999) ‘The mineral dust aerosol cycle during the Last Glacial Maximum’, *Journal of Geophysical Research: Atmospheres*. Blackwell Publishing Ltd, 104(D8), pp. 9381–9398. doi: 10.1029/1999JD900033.
- Remer, L. A. *et al.* (2005) ‘The MODIS aerosol algorithm, products, and validation’, *Journal of the Atmospheric Sciences*. American Meteorological Society, 62(4), pp. 947–973. doi: 10.1175/JAS3385.1.
- Rodó, X. *et al.* (2014) ‘Tropospheric winds from northeastern China carry the etiologic agent of Kawasaki disease from its source to Japan’, *Proceedings of the National Academy of Sciences of the United States of America*. National Academy of Sciences, 111(22), pp. 7952–7957. doi: 10.1073/pnas.1400380111.
- SAR Climate Change 1995: The Science of Climate Change — IPCC* (1995). Available at: <https://www.ipcc.ch/report/ar2/wg1/>.
- Sarver, T., Al-Qaraghuli, A. and Kazmerski, L. L. (2013) ‘A comprehensive review of the impact of dust on the use of solar energy: History, investigations, results, literature, and mitigation approaches’, *Renewable and Sustainable Energy Reviews*. Pergamon, pp. 698–733. doi: 10.1016/j.rser.2012.12.065.
- Sayer, A. M. *et al.* (2012) ‘SeaWiFS Ocean Aerosol Retrieval (SOAR): Algorithm, validation, and comparison with other data sets’, *Journal of Geophysical Research Atmospheres*. Blackwell Publishing Ltd, 117(3). doi: 10.1029/2011JD016599.
- Sayer, A. M. *et al.* (2013) ‘Validation and uncertainty estimates for MODIS Collection 6 “deep Blue” aerosol data’, *Journal of Geophysical Research Atmospheres*. Blackwell Publishing Ltd, 118(14), pp. 7864–7872. doi: 10.1002/jgrd.50600.



- Shao, Y. *et al.* (2011) ‘Dust cycle: An emerging core theme in Earth system science’, *Aeolian Research*, pp. 181–204. doi: 10.1016/j.aeolia.2011.02.001.
- Shao, Y. and Dong, C. H. (2006) ‘A review on East Asian dust storm climate, modelling and monitoring’, *Global and Planetary Change*. Elsevier, 52(1–4), pp. 1–22. doi: 10.1016/j.gloplacha.2006.02.011.
- Shao, Y. and Wang, J. (2003) ‘A climatology of Northeast Asian dust events’, *Meteorologische Zeitschrift*, 12(4), pp. 187–196. doi: 10.1127/0941-2948/2003/0012-0187.
- Smith, A., Lott, N. and Vose, R. (2011) ‘The integrated surface database: Recent developments and partnerships’, *Bulletin of the American Meteorological Society*. American Meteorological Society, 92(6), pp. 704–708. doi: 10.1175/2011BAMS3015.1.
- Sprigg, W. A. *et al.* (2014) ‘Regional dust storm modeling for health services: The case of valley fever’, *Aeolian Research*. Elsevier, 14, pp. 53–73. doi: 10.1016/j.aeolia.2014.03.001.
- TAR Climate Change 2001: The Scientific Basis — IPCC* (2001). Available at: <https://www.ipcc.ch/report/ar3/wg1/>.
- Tegen, I. (2003) ‘Modeling the mineral dust aerosol cycle in the climate system’, *Quaternary Science Reviews*. Elsevier Ltd, 22(18–19), pp. 1821–1834. doi: 10.1016/S0277-3791(03)00163-X.
- Tegen, I. and Fung, I. (1994) ‘Modeling of mineral dust in the atmosphere: Sources, transport, and optical thickness’, *Journal of Geophysical Research*, 99(D11), p. 22897. doi: 10.1029/94JD01928.
- Textor, C. *et al.* (2006) ‘Analysis and quantification of the diversities of aerosol life cycles within AeroCom’, *Atmospheric Chemistry and Physics*, 6(7), pp. 1777–1813. doi: 10.5194/acp-6-1777-2006.
- Di Tomaso, E. *et al.* (2017) ‘Assimilation of MODIS Dark Target and Deep Blue observations in the dust aerosol component of NMMB-MONARCH version 1.0’, *Geoscientific Model Development*. Copernicus GmbH, 10(3), pp. 1107–1129. doi: 10.5194/gmd-10-1107-2017.
- Tong, D. Q. *et al.* (2017) ‘Intensified dust storm activity and Valley fever infection in the southwestern United States’, *Geophysical Research Letters*. Blackwell Publishing Ltd, 44(9), pp. 4304–4312. doi: 10.1002/2017GL073524.
- Torres, O. *et al.* (2007) ‘Aerosols and surface UV products from Ozone Monitoring Instrument observations: An overview’, *Journal of Geophysical Research: Atmospheres*. John Wiley & Sons, Ltd, 112(D24). doi: 10.1029/2007JD008809@10.1002/(ISSN)2169-8996.AURA1.
- Votsis, A. *et al.* (2020) ‘Impact Assessment on Aviation and Solar Energy’, DustClim Project Report.
- Wang, Y. Q. *et al.* (2008) ‘Surface observation of sand and dust storm in East Asia and its application in CUACE/Dust’, *European Geosciences Union*, 8(3), pp. 545–553, doi: 10.5194/acp-8-545-2008.
- Washington, R. *et al.* (2003) ‘Dust-storm source areas determined by the total ozone

- monitoring spectrometer and surface observations’, *Annals of the Association of American Geographers*. Taylor & Francis Group, pp. 297–313. doi: 10.1111/1467-8306.9302003.
- Winker, D. M., Hunt, W. H. and McGill, M. J. (2007) ‘Initial performance assessment of CALIOP’, *Geophysical Research Letters*. John Wiley & Sons, Ltd, 34(19). doi: 10.1029/2007GL030135.
- Xian, P. *et al.* (2019) ‘Current state of the global operational aerosol multi-model ensemble: An update from the International Cooperative for Aerosol Prediction (ICAP)’, *Quarterly Journal of the Royal Meteorological Society*. John Wiley and Sons Ltd, 145(S1), pp. 176–209. doi: 10.1002/qj.3497.
- Yin, Y. *et al.* (2002) ‘Interactions of mineral dust particles and clouds: Effects on precipitation and cloud optical properties’, *Journal of Geophysical Research Atmospheres*. Blackwell Publishing Ltd, 107(23), p. AAC 19-1-AAC 19-14. doi: 10.1029/2001JD001544.
- Yu, H. *et al.* (2015) ‘The fertilizing role of African dust in the Amazon rainforest: A first multiyear assessment based on data from Cloud-Aerosol Lidar and Infrared Pathfinder Satellite Observations’, *Geophysical Research Letters*. Blackwell Publishing Ltd, 42(6), pp. 1984–1991. doi: 10.1002/2015GL063040.
- Zhang, X. *et al.* (2016) ‘A Systematic Review of Global Desert Dust and Associated Human Health Effects’, *Atmosphere*. MDPI AG, 7(12), p. 158. doi: 10.3390/atmos7120158.

## Appendix A: List of the selected stations for the evaluation

	USAF	WBAN	STATION NAME	COUNTRY	ICAO	LAT	LON	ELEVATION (m)
1	411840	99999	RAS AL KHAIMAH INTL	UAE	OMRK	25.61	55.9	31.1
2	411940	99999	DUBAI INTL	UAE	OMDB	25.26	55.4	10.4
3	411945	99999	AL MAKTOUM INTL AIRPORT	UAE		24.89	55.2	18.9
4	411960	99999	SHARJAH INTL	UAE	OMSJ	25.33	55.5	33.8
5	411980	99999	FUJAIRAH INTL	UAE	OMFJ	25.11	56.3	46.3
6	412160	99999	BATEEN	UAE	OMAD	24.43	54.5	4.9
7	412170	99999	ABU DHABI INTL	UAE	OMAA	24.43	54.7	26.8
8	412180	99999	AL AIN INTL	UAE	OMAL	24.26	55.6	264.9
9	605250	99999	BISKRA	ALGERIA	DAUB	34.79	5.74	88.1
10	605550	99999	SIDI MAHDI	ALGERIA	DAUK	33.07	6.09	85
11	605590	99999	GUEMAR	ALGERIA	DAUO	33.51	6.78	61.9
12	605660	99999	NOUMERAT	ALGERIA	DAUG	32.38	3.79	460.9
13	605710	99999	BECHAR	ALGERIA	DAOR	31.65	-2.3	811.1
14	605800	99999	OUARGLA	ALGERIA	DAUU	31.92	5.41	150
15	605810	99999	OUED IRARA	ALGERIA	DAUH	31.67	6.14	141.1
16	605900	99999	EL GOLEA	ALGERIA	DAUE	30.57	2.86	398.1
17	606070	99999	TIMIMOUN	ALGERIA	DAUT	29.24	0.28	313
18	606110	99999	IN AMENAS	ALGERIA	DAUZ	28.05	9.64	563
19	606200	99999	TOUAT CHEIKH SIDI MOHAMED BELKEBIR	ALGERIA	DAUA	27.84	-0.2	280.1
20	606305	99999	IN SALAH	ALGERIA		27.25	2.5	280
21	606400	99999	ILLIZI TAKHAMALT	ALGERIA	DAAP	26.72	8.62	541.9
22	606560	99999	TINDOUF	ALGERIA	DAOF	27.7	-8.2	442.9
23	606700	99999	TISKA	ALGERIA	DAAJ	24.29	9.45	968
24	411500	99999	BAHRAIN INTL	BAHRAIN	OBBI	26.27	50.6	1.8
25	647000	99999	NDJAMENA HASSAN DJAMOUS	CHAD	FTTJ	12.13	15	295
26	176000	99999	PAFOS INTL	CYPRUS	LCPH	34.72	32.5	12.5
27	176010	99999	AKROTIRI	CYPRUS	LCRA	34.59	33	23.2
28	176090	99999	LARNACA	CYPRUS	LCLK	34.88	33.6	2.4
29	623060	99999	MERSA MATRUH	EGYPT	HEMM	31.33	27.2	28.7

30	623180	99999	ALEXANDRIA INTL	EGYPT	HEAX	31.18	29.9	-1.8
31	623330	99999	PORT SAID	EGYPT		31.27	32.3	6
32	623660	99999	CAIRO INTL	EGYPT	HECA	30.12	31.4	116.4
33	623930	99999	ASYUT INTL	EGYPT	HEAT	27.05	31	235.3
34	624050	99999	LUXOR INTL	EGYPT	HELX	25.67	32.7	89.6
35	624590	99999	EL TOR	EGYPT	HETR	28.21	33.6	35.1
36	624630	99999	HURGHADA INTL	EGYPT	HEGN	27.18	33.8	15.8
37	407802	99999	KISH ISLAND	IRAN		26.52	54	31
38	407808	99999	DAYRESTAN	IRAN	OIKQ	26.75	55.9	12.5
39	408110	99999	AHWAZ	IRAN	OIAW	31.34	48.8	20.1
40	408120	99999	SHAHID ASYAEE	IRAN	OIAI	32	49.3	361.8
41	408310	99999	ABADAN	IRAN	OIAA	30.37	48.2	3
42	408330	99999	AGHAJARI	IRAN	OIAG	30.75	49.7	26.8
43	408350	99999	GACHSARAN	IRAN	OIAH	30.34	50.8	729.7
44	408580	99999	BUSHEHR	IRAN	OIBB	28.95	50.8	20.7
45	408750	99999	BANDAR ABBASS INTL	IRAN	OIKB	27.22	56.4	6.7
46	408830	99999	BANDAR LENGEH	IRAN	OIBL	26.53	54.8	20.4
47	408930	99999	JASK	IRAN	OIZJ	25.65	57.8	5.8
48	401800	99999	BEN GURION	ISRAEL	LLBG	32.01	34.9	41.1
49	406500	99999	BAGHDAD INTL AIRPORT	IRAQ	ORBI	33.27	44.2	34.7
50	406700	99999	NAJAF	IRAQ	ORNI	31.95	44.3	32
51	406890	99999	BASRAH INTL	IRAQ	ORMM	30.55	47.7	3.4
52	402700	99999	MARKA INTL	JORDAN	OJAM	31.97	36	778.8
53	402720	99999	QUEEN ALIA INTL	JORDAN	OJAI	31.72	36	730
54	403400	99999	AQABA KING HUSSEIN INTL	JORDAB	OJAQ	29.61	35	53.3
55	405820	99999	KUWAIT INTL	KUWAIT	OKBK	29.23	48	62.8
56	401000	99999	RAFIC HARIRI INTL	LEBANON	OLBA	33.82	35.5	26.5
57	612910	99999	SENOU	MALI	GABS	12.53	-8	380.1
58	601150	99999	ANGADS	MOROCCO	GMFO	34.79	-1.9	467.9
59	601350	99999	SALE	MOROCCO	GMME	34.05	-6.8	84.1
60	601410	99999	SAISS	MOROCCO	GMFF	33.93	-5	579.1
61	601500	99999	BASSATINE	MOROCCO	GMFM	33.88	-5.5	576.1
62	601560	99999	MOHAMMED V	MOROCCO	GMMN	33.37	-7.6	199.9
63	602300	99999	MENARA	MOROCCO	GMMX	31.61	-8	467.9
64	602520	99999	AL MASSIRA	MOROCCO	GMAD	30.33	-9.4	76.2

65	603400	99999	NADOR-AROUJ	MOROCCO	GMMW	34.98	-3	177
66	614150	99999	NOUADHIBOU	MAURITANIA	GQPP	20.93	-17	4.9
67	412560	99999	SEEB INTL	OMAN	OOMS	23.59	58.3	14.6
68	413160	99999	SALALAH	OMAN	OOSA	17.04	54.1	22.3
69	610430	99999	TAHOUA	NIGER	DRRT	14.88	5.27	385.9
70	610520	99999	DIORI HAMANI	NIGER	DRRN	13.48	2.18	223.1
71	411703	99999	DOHA	QATAR	OTHH	25.27	51.6	4
72	403560	99999	TURAIK	SAUDI ARABIA	OETR	31.69	38.7	854.4
73	403570	99999	ARAR	SAUDI ARABIA	OERR	30.91	41.1	552.6
74	403600	99999	GURIAH	SAUDI ARABIA	OEGT	31.41	37.3	509.6
75	403610	99999	AL JOUF	SAUDI ARABIA	OESK	29.79	40.1	689.2
76	403620	99999	RAFHA	SAUDI ARABIA	OERF	29.63	43.5	449.3
77	403730	99999	QAISUMAH	SAUDI ARABIA	OEPA	28.34	46.1	357.8
78	403750	99999	TABUK	SAUDI ARABIA	OETB	28.37	36.6	777.5
79	404000	99999	WEJH	SAUDI ARABIA	OEWJ	26.2	36.5	20.1
80	404050	99999	GASSIM	SAUDI ARABIA		26.3	43.8	648
81	404150	99999	DAMMAM (KING FAHD INT. AIRPORT)	SAUDI ARABIA		26.43	49.8	12
82	404200	99999	AL AHSA	SAUDI ARABIA	OEAH	25.29	49.5	179.2
83	404300	99999	PRINCE MOHAMMAD BIN ABDULAZIZ	SAUDI ARABIA	OEMA	24.55	39.7	655.6
84	404370	99999	KING KHALED INTL	SAUDI ARABIA	OERK	24.96	46.7	624.5
85	404390	99999	YENBO	SAUDI ARABIA	OEYN	24.14	38.1	7.9
86	410240	99999	KING ABDULAZIZ INTL	SAUDI ARABIA	OEJN	21.68	39.2	14.6
87	410610	99999	WADI AL DAWASIR	SAUDI ARABIA	OEWD	20.5	45.2	628.5
88	411360	99999	SHARURAH	SAUDI ARABIA	OESH	17.47	47.1	720.2
89	411400	99999	KING ABDULLAH BIN ABDULAZIZ	SAUDI ARABIA	OEGN	16.9	42.6	6.1
90	616000	99999	SAINT LOUIS	SENEGAL	GOSS	16.05	-16	2.7
91	616410	99999	LEOPOLD SEDAR SENGHOR INTL	SENEGAL	GOOY	14.74	-17	25.9
92	616870	99999	TAMBACOUNDA	SENEGAL	GOTT	13.74	-14	49.1
93	600150	99999	TENERIFE NORTE	SPAIN	GCXO	28.48	-16	631.9
94	600200	99999	STA. CRUZ DE TENERIFE	SPAIN		28.45	-16	36
95	600350	99999	FUERTEVENTURA	SPAIN	GCFV	28.45	-14	25.3
96	400800	99999	DAMASCUS INTL	SYRIA	OSDI	33.41	36.5	615.7



97	607450	99999	GAFSA	TUNISIA	DTTF	34.42	8.82	323.1
98	607500	99999	THYNA	TUNISIA	DTTX	34.72	10.7	25.9
99	607600	99999	NEFTA	TUNISIA	DTTZ	33.94	8.11	87.5
100	607690	99999	ZARZIS	TUNISIA	DTTJ	33.88	10.8	5.8
101	655030	99999	OUAGADOUGOU	BURKINA FASO	DFFD	12.35	-1.5	316.1

## Appendix B: Percentage reduction of observations after the application of the RH filter.

	USAF	WBAN	STATION NAME	COUNTRY	ICAO	% REDUCTION 2018	% REDUCTION 2019
1	411840	99999	RAS AL KHAIMAH INTL	UAE	OMRK	13.6	16.3
2	411940	99999	DUBAI INTL	UAE	OMDB	6.7	7.5
3	411945	99999	AL MAKTOUM INTL AIRPORT	UAE		16.4	16.5
4	411960	99999	SHARJAH INTL	UAE	OMSJ	13.3	14.6
5	411980	99999	FUJAIRAH INTL	UAE	OMFJ	18.3	20.3
6	412160	99999	BATEEN	UAE	OMAD	17.7	17.3
7	412170	99999	ABU DHABI INTL	UAE	OMAA	15.6	12.9
8	412180	99999	AL AIN INTL	UAE	OMAL	7.1	6.2
9	605250	99999	BISKRA	ALGERIA	DAUB	2.6	2.7
10	605550	99999	SIDI MAHDI	ALGERIA	DAUK	3.0	2.5
11	605590	99999	GUEMAR	ALGERIA	DAUO	5.0	5.2
12	605660	99999	NOUMERAT	ALGERIA	DAUG	1.6	1.2
13	605710	99999	BECHAR	ALGERIA	DAOR	2.4	1.0
14	605800	99999	OUARGLA	ALGERIA	DAUU	1.3	1.0
15	605810	99999	OUED IRARA	ALGERIA	DAUH	2.9	1.8
16	605900	99999	EL GOLEA	ALGERIA	DAUE	3.0	0.8
17	606070	99999	TIMIMOUN	ALGERIA	DAUT	0.7	0.4
18	606110	99999	IN AMENAS	ALGERIA	DAUZ	0.9	0.9
19	606200	99999	TOUAT CHEIKH SIDI MOHAMED BELKEBIR	ALGERIA	DAUA	0.3	0.1
20	606305	99999	IN SALAH	ALGERIA		0.1	0.1
21	606400	99999	ILLIZI TAKHAMALT	ALGERIA	DAAP	0.7	0.6
22	606560	99999	TINDOUF	ALGERIA	DAOF	3.0	1.4
23	606700	99999	TISKA	ALGERIA	DAAJ	0.3	0.0

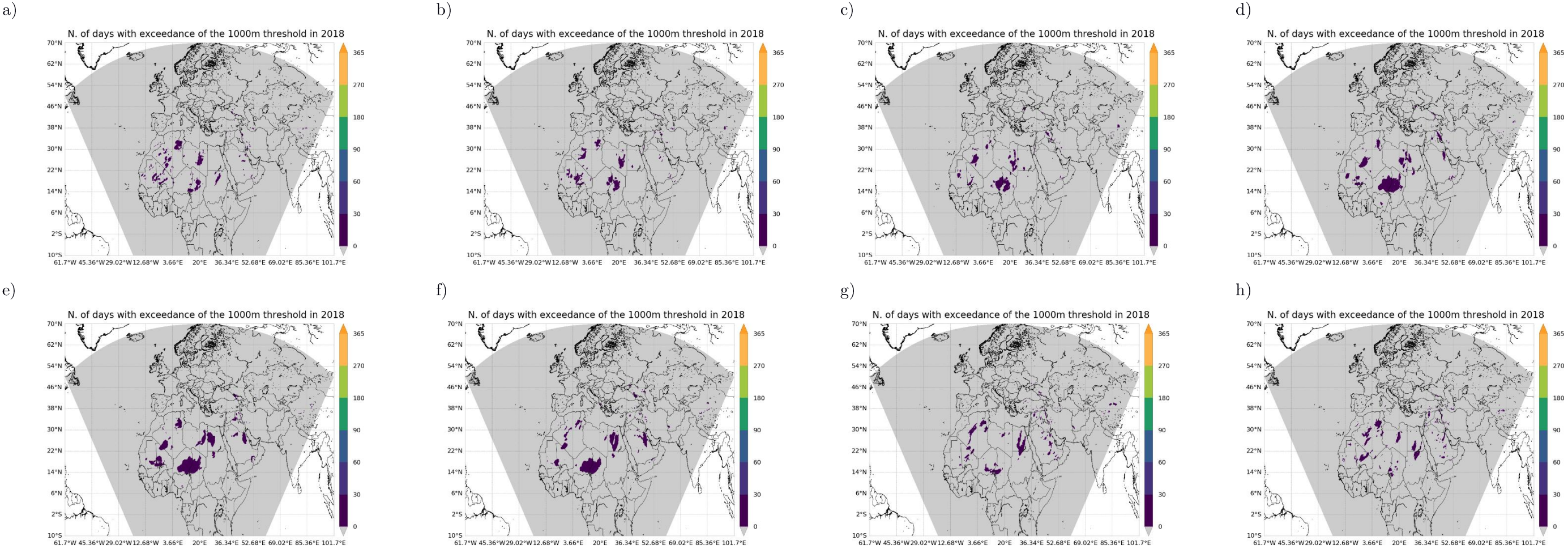
24	411500	99999	BAHRAIN INTL	BAHRAIN	OBBI	14.2	13.5
25	647000	99999	NDJAMENA HASSAN DJAMOUS	CHAD	FTTJ	20.9	22.6
26	176000	99999	PAFOS INTL	CYPRUS	LCPH	34.5	31.2
27	176010	99999	AKROTIRI	CYPRUS	LCRA	29.4	29.5
28	176090	99999	LARNACA	CYPRUS	LCLK	35.6	36.4
29	623060	99999	MERSA MATRUH	EGYPT	HEMM	33.4	33.3
30	623180	99999	ALEXANDRIA INTL	EGYPT	HEAX	24.1	24.0
31	623330	99999	PORT SAID	EGYPT		35.9	37.2
32	623660	99999	CAIRO INTL	EGYPT	HECA	12.5	11.0
33	623930	99999	ASYUT INTL	EGYPT	HEAT	2.2	1.8
34	624050	99999	LUXOR INTL	EGYPT	HELX	0.3	0.3
35	624590	99999	EL TOR	EGYPT	HETR	7.4	10.0
36	624630	99999	HURGHADA INTL	EGYPT	HEGN	1.7	1.0
37	407802	99999	KISH ISLAND	IRAN		31.2	31.2
38	407808	99999	DAYRESTAN	IRAN	OIKQ	51.4	50.7
39	408110	99999	AHWAZ	IRAN	OIAW	12.3	13.9
40	408120	99999	SHAHID ASYAEE	IRAN	OIAI	14.5	21.1
41	408310	99999	ABADAN	IRAN	OIAA	13.0	13.0
42	408330	99999	AGHAJARI	IRAN	OIAG	10.8	12.6
43	408350	99999	GACHSARAN	IRAN	OIAH	8.4	13.2
44	408580	99999	BUSHEHR	IRAN	OIBB	6.6	8.3
45	408750	99999	BANDAR ABBASS INTL	IRAN	OIKB	34.0	36.6
46	408830	99999	BANDAR LENGHEH	IRAN	OIBL	24.2	24.9
47	408930	99999	JASK	IRAN	OIZJ	47.7	46.1
48	401800	99999	BEN GURION	ISRAEL	LLBG	22.5	19.7
49	406500	99999	BAGHDAD INTL AIRPORT	IRAQ	ORBI	16.3	10.9
50	406700	99999	NAJAF	IRAQ	ORNI	12.3	10.1
51	406890	99999	BASRAH INTL	IRAQ	ORMM	11.2	10.0
52	402700	99999	MARKA INTL	JORDAN	OJAM	15.7	13.5
53	402720	99999	QUEEN ALIA INTL	JORDAN	OJAI	20.5	17.9
54	403400	99999	AQABA KING HUSSEIN INTL	JORDAB	OJAQ	1.1	0.8
55	405820	99999	KUWAIT INTL	KUWAIT	OKBK	12.3	9.9
56	401000	99999	RAFIC HARIRI INTL	LEBANON	OLBA	11.5	13.3
57	612910	99999	SENOU	MALI	GABS	27.1	34.6

58	601150	99999	ANGADS	MOROCCO	GMFO	34.3	25.4
59	601350	99999	SALE	MOROCCO	GMME	48.5	51.8
60	601410	99999	SAISS	MOROCCO	GMFF	37.7	24.2
61	601500	99999	BASSATINE	MOROCCO	GMFM	47.1	32.1
62	601560	99999	MOHAMMED V	MOROCCO	GMMN	65.7	59.6
63	602300	99999	MENARA	MOROCCO	GMMX	15.6	13.0
64	602520	99999	AL MASSIRA	MOROCCO	GMAD	39.9	40.8
65	603400	99999	NADOR-AROUJ	MOROCCO	GMMW	29.8	22.5
66	614150	99999	NOUADHIBOU	MAURITANIA	GQPP	27.7	28.8
67	412560	99999	SEEB INTL	OMAN	OOMS	27.1	29.7
68	413160	99999	SALALAH	OMAN	OOSA	54.6	45.9
69	610430	99999	TAHOUA	NIGER	DRRT	7.1	8.9
70	610520	99999	DIORI HAMANI	NIGER	DRRN	11.4	9.3
71	411703	99999	DOHA	QATAR	OTHH	7.4	7.4
72	403560	99999	TURAIF	SAUDI ARABIA	OETR	17.9	16.1
73	403570	99999	ARAR	SAUDI ARABIA	OERR	17.8	13.6
74	403600	99999	GURIAT	SAUDI ARABIA	OEGT	6.1	2.9
75	403610	99999	AL JOUF	SAUDI ARABIA	OESK	5.1	2.6
76	403620	99999	RAFHA	SAUDI ARABIA	OERF	3.5	2.5
77	403730	99999	QAISUMAH	SAUDI ARABIA	OEPA	8.4	4.9
78	403750	99999	TABUK	SAUDI ARABIA	OETB	0.2	0.7
79	404000	99999	WEJH	SAUDI ARABIA	OEWD	27.6	24.6
80	404050	99999	GASSIM	SAUDI ARABIA		14.8	11.2
81	404150	99999	DAMMAM (KING FAHD INT. AIRPORT)	SAUDI ARABIA		6.8	7.0
82	404200	99999	AL AHSA	SAUDI ARABIA	OEAH	5.1	5.7
83	404300	99999	PRINCE MOHAMMAD BIN ABDULAZIZ	SAUDI ARABIA	OEMA	1.3	0.4
84	404370	99999	KING KHALED INTL	SAUDI ARABIA	OERK	4.0	2.6
85	404390	99999	YENBO	SAUDI ARABIA	OEYN	15.4	10.9
86	410240	99999	KING ABDULAZIZ INTL	SAUDI ARABIA	OEJN	7.5	6.7
87	410610	99999	WADI AL DAWASIR	SAUDI ARABIA	OEWD	2.7	2.4
88	411360	99999	SHARURAH	SAUDI ARABIA	OESH	0.3	0.5
89	411400	99999	KING ABDULLAH BIN ABDULAZIZ	SAUDI ARABIA	OEGN	18.2	24.1
90	616000	99999	SAINT LOUIS	SENEGAL	GOSS	43.6	41.3

91	616410	99999	LEOPOLD SEDAR SENGHOR INTL	SENEGAL	GOOY	66.9	64.3
92	616870	99999	TAMBACOUNDA	SENEGAL	GOTT	20.7	27.5
93	600150	99999	TENERIFE NORTE	SPAIN	GCXO	66.9	58.6
94	600200	99999	STA. CRUZ DE TENERIFE	SPAIN		7.4	4.7
95	600350	99999	FUERTEVENTURA	SPAIN	GCFV	26.3	25.4
96	400800	99999	DAMASCUS INTL	SYRIA	OSDI	23.9	19.8
97	607450	99999	GAFSA	TUNISIA	DTTF	12.5	5.8
98	607500	99999	THYNA	TUNISIA	DTTX	13.1	14.5
99	607600	99999	NEFTA	TUNISIA	DTTZ	2.9	3.0
100	607690	99999	ZARZIS	TUNISIA	DTTJ	16.1	13.1
101	655030	99999	OUAGADOUGOU	BURKINA FASO	DFFD	17.3	22.0

Appendix C: Critical hours for the exceedance of the 1000m threshold

Frequency of exceedance of the 1000m threshold per 3-hourly timesteps and grid cell during 2018. a) Valid for 00h, b) Valid for 03h, c) Valid for 06h, d) Valid for 09h, e) Valid for 12h, f) Valid for 15h, g) Valid for 18h, h) Valid for 21h





Frequency of exceedance of the 1000m threshold per 3-hourly timesteps and grid cell during 2019. a) Valid for 00h, b) Valid for 03h, c) Valid for 06h, d) Valid for 09h, e) Valid for 12h, f) Valid for 15h, g) Valid for 18h, h) Valid for 21h

